Eng. Sci., 2025, **37**, 1700

Engineered Science
DOI: https://dx.doi.org/10.30919/es1700

Structural Design and Parameter Optimization Analysis of a Novel Three-Dimensional Vibration Isolation Device

Tao Liu[1], Xiansong Xie[1,*] and Aiqun Li[2,3]

Abstract

To resolve the trade-off between stability and vibration isolation performance in linear systems, vertical and horizontal quasi-zero stiffness (QZS) vibration isolators are designed using coil springs and a slider-guide mechanism. A new type of three-dimensional quasi-zero stiffness isolation structure is developed, consisting of one vertical isolation module combined with two horizontal isolation modules arranged orthogonally through connecting components. Analytical results confirm that this system exhibits quasi-zero stiffness characteristics along all three principal axes when maintained in static balance. The effects of different design parameters on the mechanical properties are analyzed, and the parameters of the three-dimensional QZS system are optimized to expand the QZS range and improve low-frequency isolation performance. The dynamics of the system under optimized parameters are studied, and the transmissibility of the three-dimensional QZS system is compared with traditional QZS and equivalent linear systems to evaluate the vibration isolation performance of the new device. Finally, shaking table tests are conducted on the three-dimensional QZS isolator to assess the effect of excitation amplitude on the system. The experimental transmissibility is compared with theoretical predictions, validating the dynamic behavior of the device and confirming its superior low-frequency vibration isolation capabilities.

Keywords: Three-dimensional QZS vibration isolator; Theoretical mechanical model; Parameter design; QZS interval; Low-frequency vibration isolation performance; Shaking table tests.
Received: 17 June 2025; Revised: 18 July 2025; Accepted: 02 August 2025
Article type: Research article.

1. Introduction

Passive isolation technology refers to the installation of isolation devices between the vibration source and the isolated object to reduce the transmitted vibration. When the isolated object and the linear vibration isolation system are determined, the isolation range is a fixed frequency domain, and the low frequency vibration beyond its isolation range cannot be effectively isolated. Therefore, it is of great engineering importance to propose a nonlinear vibration device with high static stiffness and low dynamic stiffness compared with the traditional linear isolation system. Higher static stiffness means less deflection and larger load carrying capacity, while decreased dynamic stiffness leads to an expanded frequency range for vibration isolation.

The stiffness characteristics of nonlinear vibration isolators can be achieved by combining positive and negative stiffnesses to create a near-zero stiffness, which is referred to as the QZS characteristic. Molyneux[1] was the first to create a quasi-zero stiffness system with two springs arranged at an angle to form a negative stiffness structure in 1957. In 1976, Eijk *et al*.[2] designed a plate spring type system and introduced a comprehensive theory of quasi-zero stiffness vibration isolation. In 1999, Platus[3] designed an eccentric articulated Eulerian compression bar as a negative stiffness structure and used the compression bar system to avoid structural instability. Since the twenty-first century, various vibration isolators with quasi-zero stiffness characteristics have been developed, which can be classified according to different negative stiffness structures as follows:

(1) Tilting spring vibration isolation system: The even number of springs is hinged at one end at the center point and the other end is arranged at a fixed tilt angle, so that when the

[1]*School of Architectural Engineering, Quzhou University, Quzhou, Zhejiang, 324000, China*
[2]*Department of Civil Engineering, Southeast University, Nanjing, Jiangsu, 211189, China*
[3]*School of Civil Engineering and Transportation engineering, Beijing University of Civil Engineering and Architecture, Beijing, 100044, China*
[*]*Email*: lt2957327761@gmail.com (Xiansong Xie)

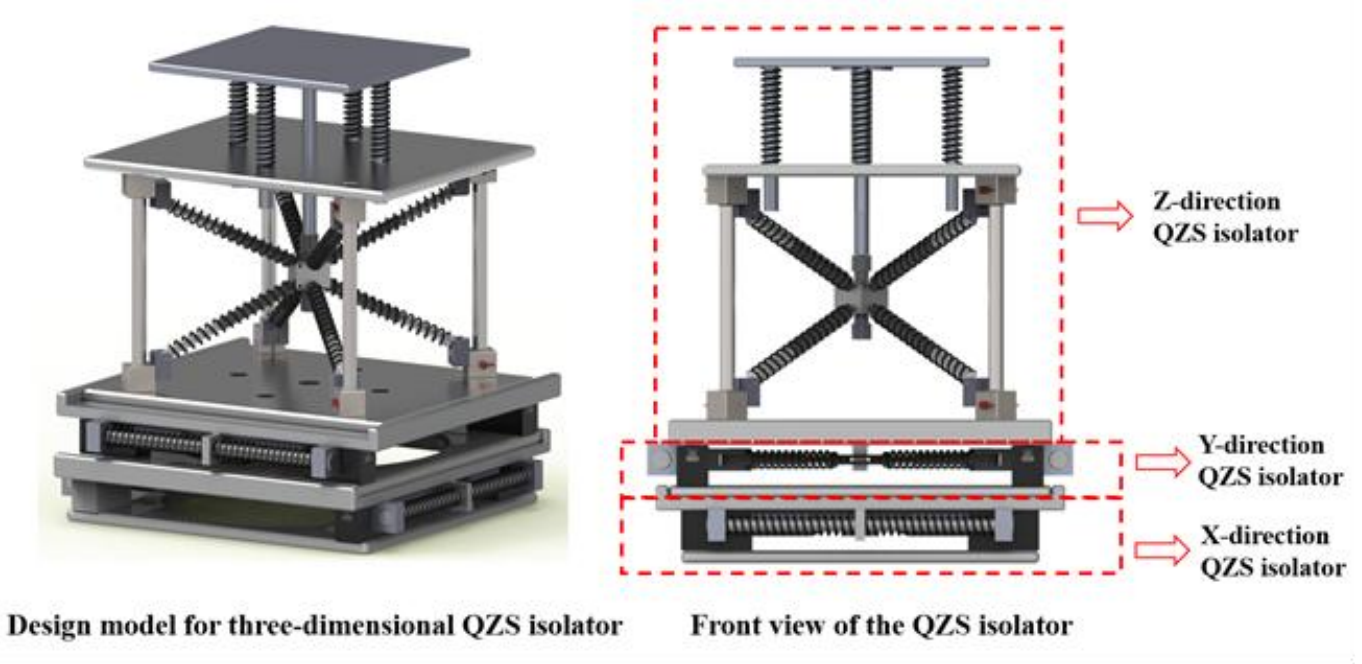

Fig. 1: 3D model representation of the three-dimensional QZS isolator.

system is subjected to a vertical load, the load gradually decreases as the displacement increases, resulting in a tilt spring type negative stiffness structure. One representative example is the vibration isolation system configured with three springs,[4-7] on which later scholars have based different forms of improvement, designing multi-spring QZS structures,[8-11] special spring QZS structures[12-14] and slider-rod QZS structures.[15-17]

(2) Euler flexure beam/rod vibration isolation system: Buckling beams generally indicate structural elements that bear lateral or axial forces. Their unique property of negative stiffness arises because, under specific loading conditions, these beams can experience localized or global buckling phenomena, depending on factors such as geometry, boundary constraints, and the manner in which force is applied[18-22]. Eulerian compression rods are long thin rods that experience stability failure under axial compression, and their negative stiffness characteristics are mainly reflected in the fact that after reaching the critical compression force, any small perturbation may lead to significant deformation of the structure.[23-25] Both serve as key reference models in structural stability research and can display negative stiffness behavior once a defined critical threshold is surpassed, at which point the structure may experience significant shape changes triggered by external disturbances.[26-28]

(3) Geometrically Nonlinear Vibration Isolation Systems: Structures with geometrical nonlinearity leverage specific configurations and structural forms to generate nonlinear dynamic responses. Under external forces or disturbances, the system's stiffness and damping behavior adjust according to variations in displacement or applied load, enabling enhanced vibration and impact mitigation. Such nonlinear features are introduced by carefully designing structural contours, optimizing material layout, or applying initial pre-load conditions. This design approach allows the vibration isolation system to exhibit excellent performance in vibration isolation, shock absorption and energy conversion, and is particularly suited to applications that require effective vibration isolation over a wide bandwidth, or where there are special requirements for specific vibration frequencies. Quasi-zero stiffness vibration isolators with geometrical nonlinear characteristics can be mainly classified into rhombic structures,[29-31] scissor structures[32-36] and cam structures.[37-42]

(4) Magnetic vibration isolation system: Magnetic-based vibration isolation systems utilize the nonlinear characteristics inherent in magnetic fields to create negative stiffness behavior. Through deliberate configuration of magnetic components, forces of attraction or repulsion are introduced within the structure. When these magnetic forces interact with elements providing positive stiffness, they can counteract part of the positive stiffness contribution, leading to an overall reduction in system stiffness. By carefully tuning the position and distance between magnets, the combined system stiffness can be minimized or even approach zero under defined loading and displacement scenarios, thereby realizing quasi-zero stiffness performance. Magnetic quasi-zero stiffness vibration isolators are categorized into permanent magnet systems,[43–46] electromagnetic systems,[47–49] hybrid magnetic systems,[50–53] and magnetic levitation systems.[54–56]

Considering that most of the existing quasi-zero stiffness vibration isolation systems focus on vertical vibration, a new type of QZS isolation device has not yet been proposed to meet the requirements of three-dimensional vibration isolation, the authors propose an innovative three-dimensional vibration isolator based on coil springs and slider-guide connecting mechanism with quasi-zero stiffness characteristics for

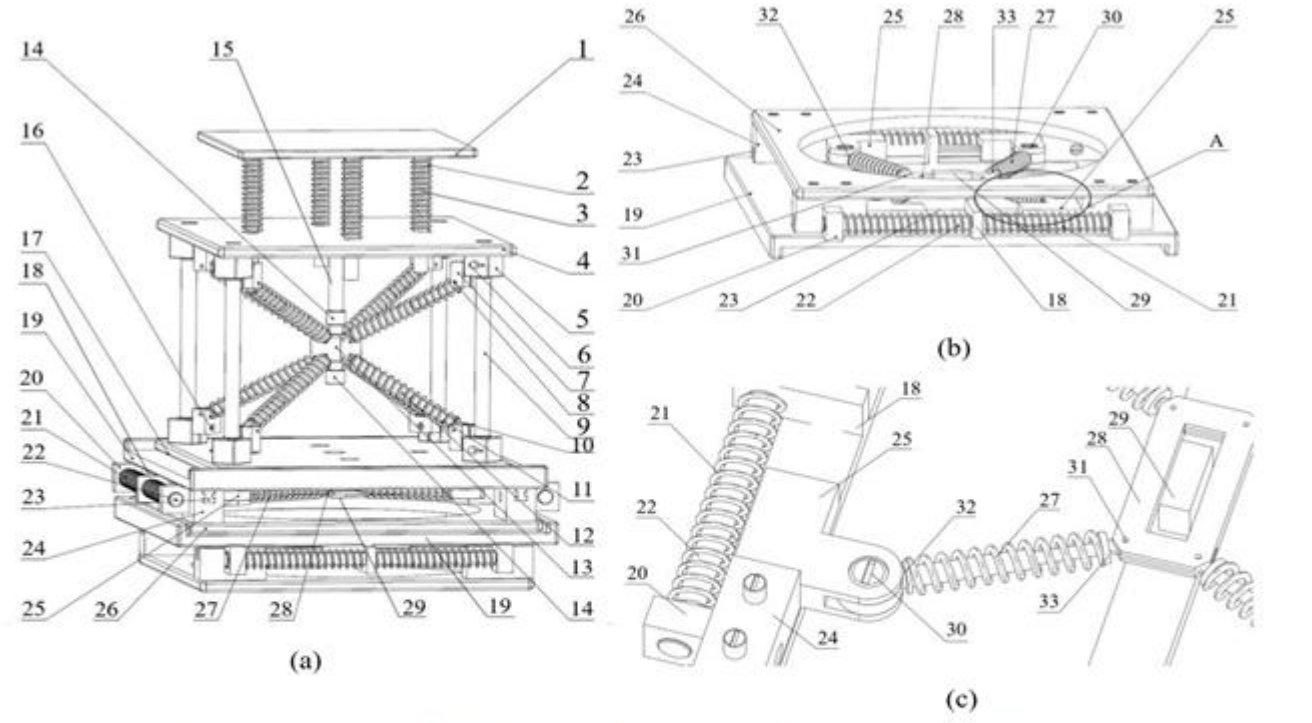

Fig. 2: Three-dimensional QZS device: (a) full structure, (b) horizontal isolator, (c) detail view at A.

practical engineering applications.

2. Three-dimensional QZS isolator description

Building on research into multi-spring structures[8-11] and slider-rod structures,[15-17] this study develops vertical and horizontal QZS vibration isolators by combining pre-loaded inclined springs and a slider-guided setup to generate negative stiffness, together with vertically and horizontally arranged helical springs providing positive stiffness. Both negative and positive stiffness components are integrated in parallel through a connecting rod and motion transmission system. Furthermore, by vertically cross-assembling a set of vertical vibration isolators (Z-direction) and a pair of horizontal vibration isolators (X- and Y-directions) through a connecting plate, a three-dimensional QZS vibration device is developed, as shown in Fig. 1, which achieves high static stiffness with low dynamic stiffness under three-directional vibrations. The structural design and motion mechanism of the isolators in the X- and Y-directions are essentially identical, adopting four pre-compressed tilting spring elements symmetrically arranged horizontally as well as the slider-guide connecting mechanism on both sides as the components of the negative stiffness structure. The two sides of the negative stiffness structure are respectively equipped with corresponding horizontal coil springs as the positive stiffness structure, and the positive and negative stiffness structures are jointly assembled on the base plate to enable it to achieve QZS characteristics under the action of horizontal vibration.

As shown in Fig. 2, the proposed three-dimensional quasi-zero stiffness (QZS) structure integrates one vertical isolator along the Z-axis and two horizontal isolators aligned with the X and Y axes. The vertical isolator is constructed from a carrier plate (1), an upper limiting plate (4), and a lower limiting plate (17). Between the carrier plate and the upper limiting plate, four vertically positioned coil springs are arranged to establish the system's vertical positive stiffness. The vertical negative stiffness system, located between the upper and lower limit plates, consists of eight sets of tilting shock absorbers with first pre-compressed tilting coil springs (11) as elastic elements. The adjustable support portion, comprising four support columns (9) and eight round hole sliders (5), limits the compression stroke, while the connecting rod (15) links the vertical positive and negative stiffness systems. A first central connecting block (13) moves along the rod, adjustable via two nuts (14) on a threaded section to modify load-bearing characteristics. The tilting shock absorber includes a first piston rod (10), a first piston sleeve (12), and a first slider (7) mounted on round hole sliders, with

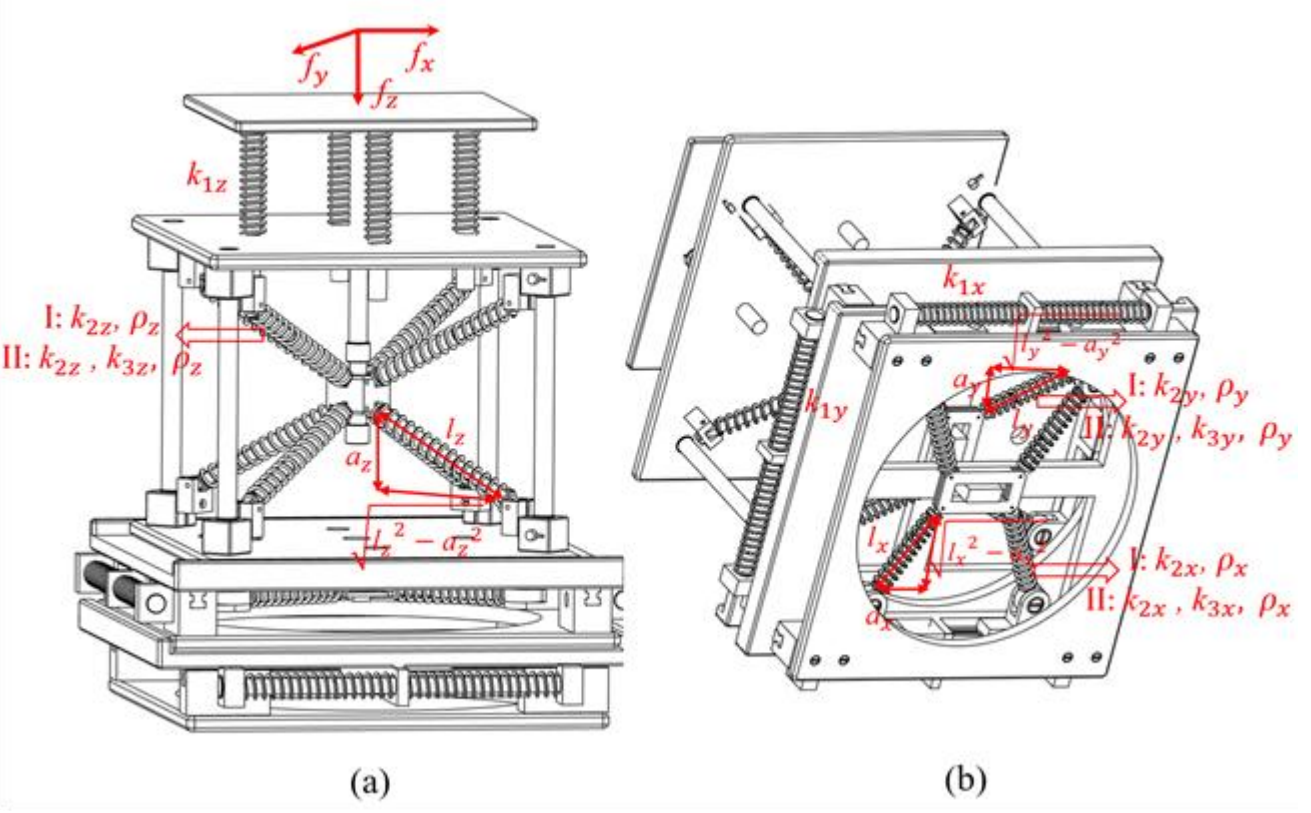

Fig. 3: Spring characteristics and structural parameters of the three-dimensional QZS isolator; (a) vertical isolator (Z-axis), (b) horizontal isolators (X- and Y-axes).

viscous damping fluid inside the piston sleeve to absorb energy and control displacement.

The horizontal isolator consists of a connection plate (19) and a base plate (26), positioned up and down, with two guide rails (23) on the bottom surface of the connection plate and a drive block (29) in the middle, moving linearly along the guide rails. The horizontal negative stiffness system comprises a second central connecting block (28) and four symmetrically arranged sets of second pre-compressed tilting coil springs (27). The horizontal positive stiffness system consists of two baffle plates (18), four sets of horizontal coil springs (21), and two second slide rods (22), with each slide rod passing through the coil springs and baffle plates. The system further includes four second sliders (25), each connected to a limit slider (24) and a second pre-compressed tilting coil spring (27), enabling movement along the guide rails. A second piston rod (33), enclosed in a second piston sleeve (32) and connected to a second slider (25) via a round head bolt (30), allows for additional damping using a viscous damping fluid to control horizontal displacement. The two horizontal isolators are stacked, with the upper connection plate (19) in contact with the lower limit plate (17) and the lower base plate (26) in contact with the upper isolator's connection plate.

The first sliders (7), mounted on round hole sliders (5), face the center of the upper and lower limit plates and can slide vertically along their supporting walls. The position of each first slider (7) is defined by a screw (16), enabling precise regulation of the deformation range within the vertical subsystem that generates negative stiffness. This assembly provides adjustable load-bearing capacity, enhanced damping, and controlled displacement across three dimensions. To simplify the theoretical model, all components except the springs are treated as rigid bodies, focusing on the QZS mechanism and isolation characteristics. However, we acknowledge that under complex excitation conditions, structural flexibility and internal modal effects, particularly those involving coupled horizontal translation and rotation, may influence overall performance. This will be further addressed in future work.

3. Static Analysis of three-dimensional QZS isolator

The vibration isolators produce both vertical and horizontal compression movements through the connecting plates under the action of three-dimensional motion of the ground or three-dimensional vibration of the isolated object. At the designed starting displacement stage, the vertical and horizontal positive stiffness systems can work independently to provide positive stiffness, and after the preset displacement is reached, the negative stiffness and the positive stiffness systems will work together. The dynamic behavior of the three-dimensional QZS isolator is primarily influenced by both the mechanical characteristics of its coil springs and the structural dimensions of the device, as indicated in Fig. 3(a). For modeling purposes, the vertical direction's positive stiffness is represented by the spring constant k_{1z} , while the tilted spring mechanism providing negative stiffness in the vertical direction is

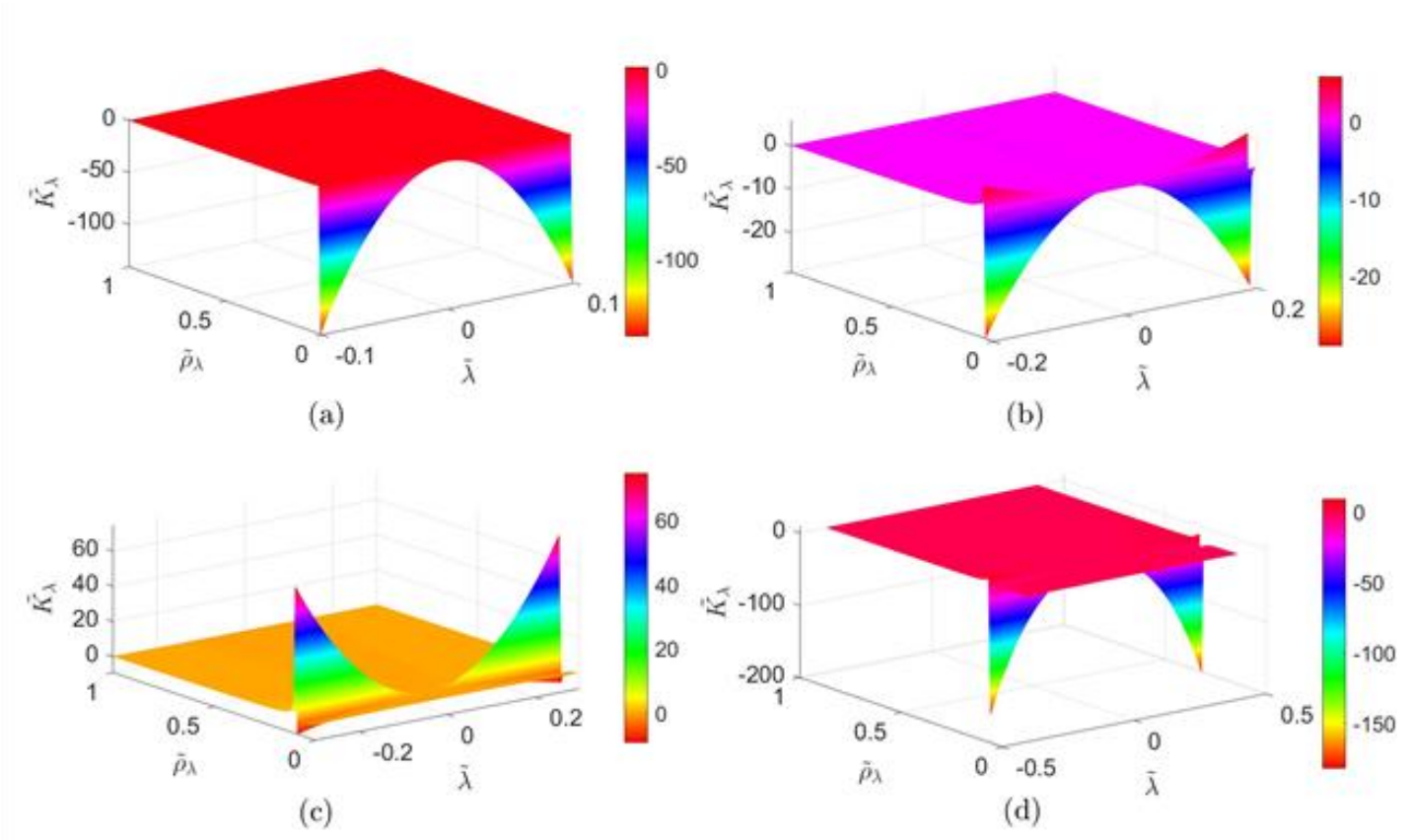

Fig. 4: A 3D surface plot of the dimensionless stiffness $\tilde{K}_\lambda$ as a function of parameters $\tilde{\rho}_\lambda$ and $\tilde{\lambda}$. ($\nu_\lambda = 0$); (a) $\tilde{a}_\lambda = 0.1$, (b) $\tilde{a}_\lambda = 0.2$, (c) $\tilde{a}_\lambda = 0.3$, (d) $\tilde{a}_\lambda = 0.4$.

described using two separate setups. In these setups, the stiffness coefficient of the inclined spring is denoted as k_{2z}, its pre-compression amount as ρ_z, and the softening cubic stiffness coefficient as k_{3z}. These two structural configurations along with their related parameters are identified as cases I and II in the analysis. In Fig. 3(b), the coil spring stiffness coefficients k_{1x} and k_{1y} are defined for the horizontal systems, and two different configurations of the tilting coil springs are also considered, where the stiffness coefficients of the tilting springs are k_{2x} and k_{2y}, the pre-compression of the tilting springs are ρ_x and ρ_y, and the softening cubic stiffness coefficients of the tilting springs are k_{3x} and k_{3y}, and these configurations and the corresponding parameters are likewise labelled I and II in Fig. 3(b).

Referring to the structural dimensions illustrated in Fig. 3(a), the length of the pre-compressed spring in the vertical negative stiffness unit is denoted as l_z. Taking into account its pre-compression amount ρ_z, the total free length of the inclined spring along the Z-direction becomes $l_z + \rho_z$. The displacement range available for vertical compression in this setup is defined as a_z, which corresponds to the vertical projection height of the pre-compressed spring. Similarly, as shown in Fig. 3(b), for the horizontal negative stiffness mechanisms along the X- and Y-axes, the pre-compressed spring lengths are defined as l_x and l_y, while their total free lengths, including pre-compression, are $l_x + \rho_x$ and $l_y + \rho_y$, respectively. The maximum compression displacements along the X- and Y-directions are given as a_x and a_y, representing the respective projection distances of the inclined pre-compressed springs in both horizontal directions.

In this study, the vertical and horizontal isolation mechanisms are treated as independent subsystems to simplify the theoretical model. This simplification enables focused analysis of the quasi-zero stiffness characteristics along each principal direction. It is acknowledged that in practical implementations, connecting plates, mounting frames, and other structural components possess finite stiffness, which may introduce coupled stiffness terms between translational motions along the X, Y, and Z axes. Such coupling effects may influence the overall isolation performance, particularly in cases involving large equipment or precision isolation requirements. The present model provides a first-order approximation. Coupling effects will be further analyzed and considered in future refined dynamic models. Further, we can derive the force-displacement characteristics of the three-dimensional vibration isolators in the Z-direction, X-direction and Y-direction respectively.

Within the range of $-a_z < z < a_z$, the relationship between the applied force f_z along the Z-axis and the corresponding displacement z can be described as follows

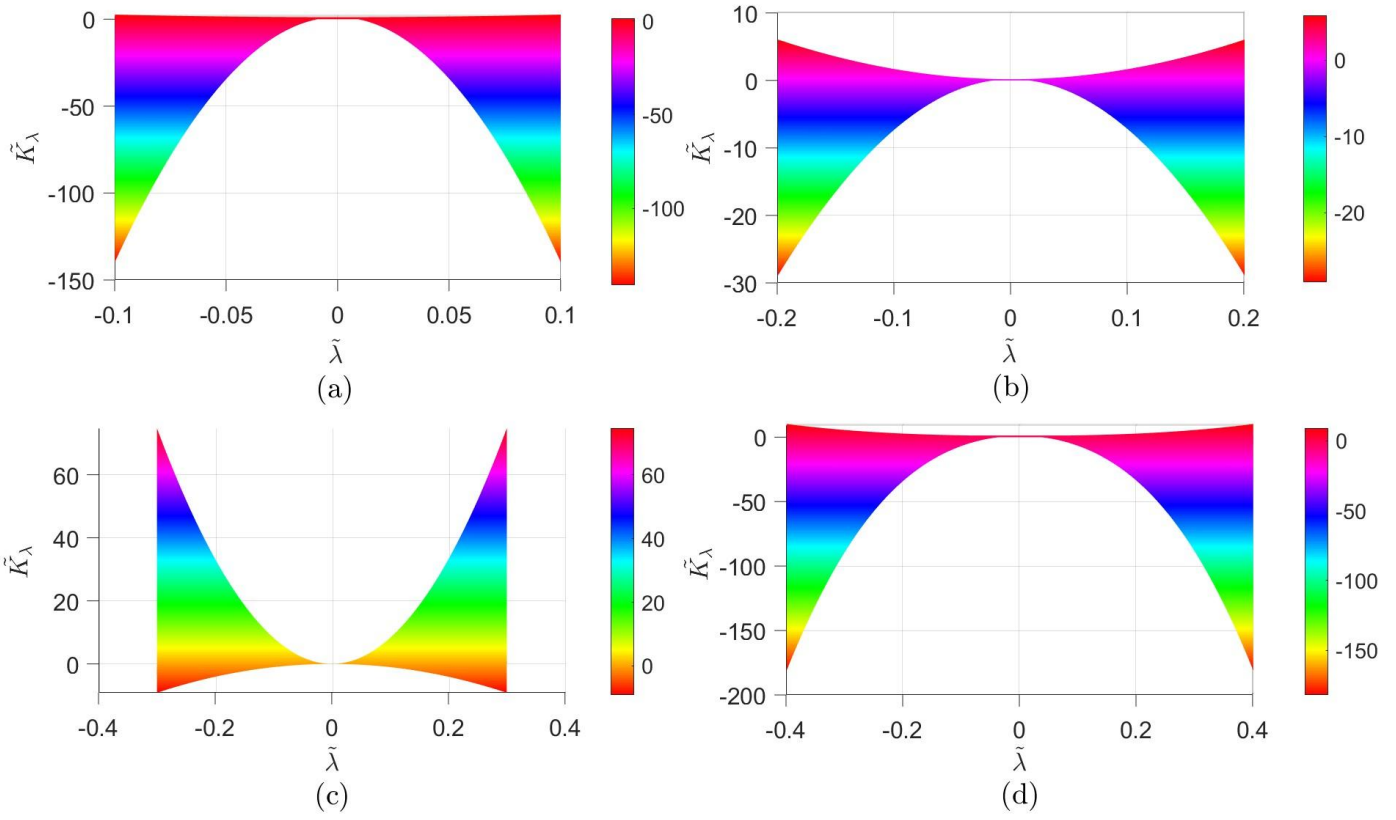

Fig. 5: A 2D mapping diagram of the dimensionless stiffness $\tilde{K}_\lambda$ as a function of parameter $\tilde{\lambda}$. ($\nu_\lambda = 0$); (a) $\tilde{a}_\lambda = 0.1$, (b) $\tilde{a}_\lambda = 0.2$, (c) $\tilde{a}_\lambda = 0.3$, (d) $\tilde{a}_\lambda = 0.4$.

$$f_x = 4k_{1z}z + \{4k_{2z}\frac{a_z - z}{\sqrt{{l_z}^2 + z^2 - 2a_z z}}(l_z + \rho_z - \sqrt{{l_z}^2 + z^2 - 2a_z z}) - 4k_{3z}\frac{a_z - z}{\sqrt{{l_z}^2 + z^2 - 2a_z z}}(l_z + \rho_z - \sqrt{{l_z}^2 + z^2 - 2a_z z})^3 - 4k_{2z}\frac{a_z + z}{\sqrt{{l_z}^2 + z^2 + 2a_z z}}\left(l_z + \rho_z - \sqrt{{l_z}^2 + z^2 + 2a_z z}\right) + 4k_{3z}\frac{a_z + z}{\sqrt{{l_z}^2 + z^2 + 2a_z z}}(l_z + \rho_z - \sqrt{{l_z}^2 + z^2 + 2a_z z})^3\} \quad (1)$$

Within the range of $-a_x < x < a_x$, the relationship between the applied force f_x along the Z-axis and the corresponding displacement x can be described as follows

$$f_x = 2k_{1x}x + \{2k_{2x}\frac{a_x - x}{\sqrt{{l_x}^2 + x^2 - 2a_x x}}(l_x + \rho_x - \sqrt{{l_x}^2 + x^2 - 2a_x x}) - 2k_{3x}\frac{a_x - x}{\sqrt{{l_x}^2 + x^2 - 2a_x x}}(l_x + \rho_x - \sqrt{{l_x}^2 + x^2 - 2a_x x})^3 - 2k_{2x}\frac{a_x + x}{\sqrt{{l_x}^2 + x^2 + 2a_x x}}(l_x + \rho_x - \sqrt{{l_x}^2 + x^2 + 2a_x x}) + 2k_{3x}\frac{a_x + x}{\sqrt{{l_x}^2 + x^2 + 2a_x x}}(l_x + \rho_x - \sqrt{{l_x}^2 + x^2 + 2a_x x})^3\} \quad (2)$$

Within the range of $-a_y < y < a_y$, the relationship between the applied force f_y along the Z-axis and the corresponding displacement y can be described as follows

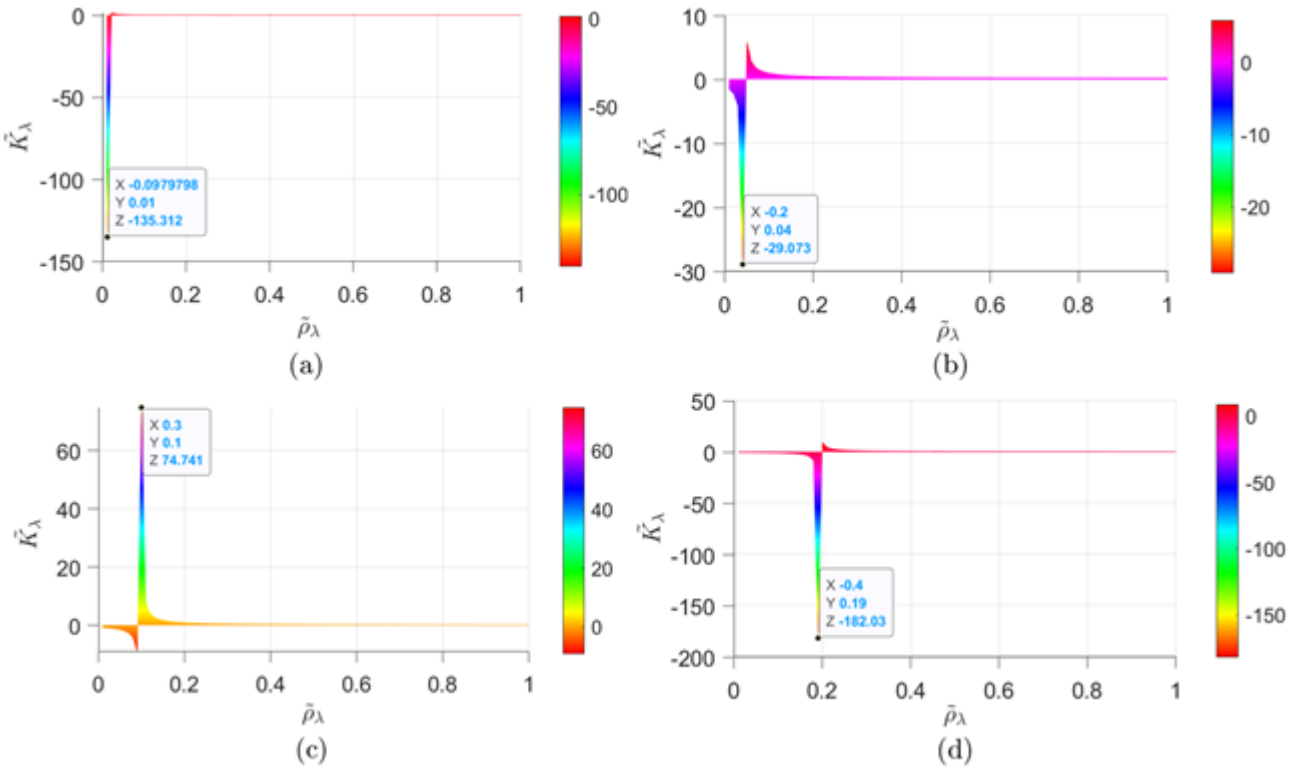

Fig. 6: A 2D mapping diagram of the dimensionless stiffness $\tilde{K}_\lambda$ as a function of parameter $\tilde{\rho}_\lambda$. ($\nu_\lambda = 0$); (a) $\tilde{a}_\lambda = 0.1$, (b) $\tilde{a}_\lambda = 0.2$, (c) $\tilde{a}_\lambda = 0.3$, (d) $\tilde{a}_\lambda = 0.4$.

$$f_x = 2k_{1y}y + \{2k_{2y}\frac{a_y - y}{\sqrt{l_y{}^2 + y^2 - 2a_y y}}(l_x + \rho_x - \sqrt{l_y{}^2 + y^2 - 2a_y y}) - 2k_{3y}\frac{a_y - y}{\sqrt{l_y{}^2 + y^2 - 2a_y y}}(l_x + \rho_x - \sqrt{l_y{}^2 + y^2 - 2a_y y})^3 - 2k_{2y}\frac{a_y - y}{\sqrt{l_y{}^2 + y^2 + 2a_y y}}(l_x + \rho_x - \sqrt{l_y{}^2 + y^2 + 2a_y y}) + 2k_{3y}\frac{a_y - y}{\sqrt{l_y{}^2 + y^2 + 2a_y y}}(l_x + \rho_x - \sqrt{l_y{}^2 + y^2 + 2a_y y})^3\} \tag{3}$$

The structural configuration and dynamic behavior of the QZS isolation units along the X-axis and Y-axis within the three-dimensional system are identical; therefore, their corresponding mechanical models can be uniformly represented by Eq. (2) and Eq. (3). Meanwhile, since the QZS characteristics are designed based on the tilting pre-compression springs as negative stiffness structure, the mechanical models of the three-dimensional isolator in the horizontal and vertical directions are also similar to a certain extent. Based on Eq. (1), Eq. (2) and Eq. (3), the mechanical model of the three-dimensional isolator can be written uniformly as follows

when $-a_\lambda < \lambda < a_\lambda$

$$nf_\lambda = k_{1\lambda}\lambda + \{k_{2\lambda}\frac{a_\lambda - \lambda}{\sqrt{l_\lambda{}^2 + \lambda^2 - 2a_\lambda\lambda}}(l_\lambda + \rho_\lambda - \sqrt{l_\lambda{}^2 + \lambda^2 - 2a_\lambda\lambda}) - k_{3\lambda}\frac{a_\lambda - \lambda}{\sqrt{l_\lambda{}^2 + \lambda^2 - 2a_\lambda\lambda}}(l_\lambda + \rho_\lambda - \sqrt{l_\lambda{}^2 + \lambda^2 - 2a_\lambda\lambda})^3 - k_{2\lambda}\frac{a_\lambda + \lambda}{\sqrt{l_\lambda{}^2 + \lambda^2 + 2a_\lambda\lambda}}(l_\lambda + \rho_\lambda - \sqrt{l_\lambda{}^2 + \lambda^2 + 2a_\lambda\lambda}) + k_{3\lambda}\frac{a_\lambda + \lambda}{\sqrt{l_\lambda{}^2 + \lambda^2 + 2a_\lambda\lambda}}(l_\lambda + \rho_\lambda - \sqrt{l_\lambda{}^2 + \lambda^2 + 2a_\lambda\lambda})^3\} \tag{4}$$

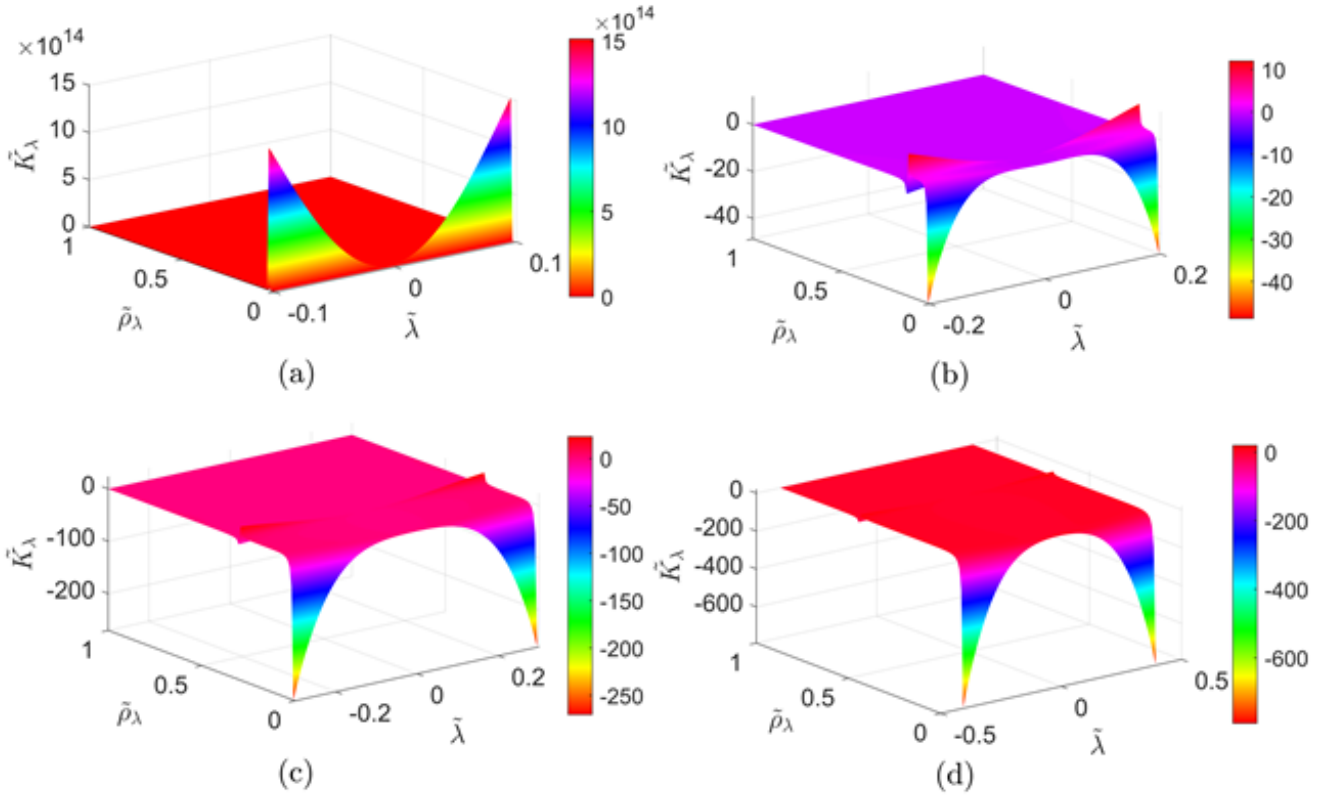

Fig. 7: A 3D surface plot of the dimensionless stiffness $\tilde{K}_\lambda$ as a function of parameters $\tilde{\rho}_\lambda$ and $\tilde{\lambda}$. ($\nu_\lambda \neq 0$); (a) $\tilde{a}_\lambda = 0.1$, (b) $\tilde{a}_\lambda = 0.2$, (c) $\tilde{a}_\lambda = 0.3$, (d) $\tilde{a}_\lambda = 0.4$.

In the dimensionless formulation, $\lambda = z$ corresponds to the vertical QZS mechanism along the Z-axis within the three-dimensional structure, where n takes the value 1/4 in Eq. (4). Similarly, $\lambda = x$ or $\lambda = y$ denotes the horizontal QZS mechanisms along the X- and Y-axes, with n equal to 1/2 in Eq. (4). By applying this unified dimensionless approach, it becomes possible to compare different system configurations and identify shared features or distinctions, thereby extending the general conclusions of the study. The following normalized parameters are introduced: $\tilde{f}_\lambda = nf_\lambda/k_{1\lambda}l_\lambda$, $\tilde{\lambda} = \lambda/l_\lambda$, $\tilde{a}_\lambda = a_\lambda/l_\lambda$, $\tilde{\rho}_\lambda = \rho_\lambda/l_\lambda$, $\mu_\lambda = k_{2\lambda}/k_{1\lambda}$, $\nu_\lambda = k_{3\lambda}{l_\lambda}^2/k_{1\lambda}$, and further simplified Eq. (4) as follows
when $-\tilde{a}_\lambda < \tilde{\lambda} < \tilde{a}_\lambda$

$$\begin{aligned}\tilde{f}_\lambda = \tilde{\lambda} + \{&\mu_\lambda\Gamma_{1\lambda}(\Phi_{1\lambda}-1) - \mu_\lambda\Gamma_{2\lambda}(\Phi_{2\lambda}-1)\\ &- \nu_\lambda\Gamma_{1\lambda}{H_{1\lambda}}^2(\Phi_{1\lambda}-1)^3\\ &+ \nu_\lambda\Gamma_{2\lambda}{H_{2\lambda}}^2(\Phi_{2\lambda}-1)^3\}\end{aligned} \tag{5}$$

The definitions of the simplified parameters in Eq. (5) are as follows: $\Gamma_{1\lambda} = \tilde{a}_\lambda - \tilde{\lambda}$, $\Gamma_{2\lambda} = \tilde{a}_\lambda + \tilde{\lambda}$, $H_{1\lambda} = \sqrt{1+\tilde{\lambda}^2 - 2\tilde{a}_\lambda\tilde{\lambda}}$, $H_{2\lambda} = \sqrt{1+\tilde{\lambda}^2 + 2\tilde{a}_\lambda\tilde{\lambda}}$, $\Phi_{1\lambda} = (1+\tilde{\rho}_\lambda)/H_{1\lambda}$, $\Phi_{2\lambda} = (1+\tilde{\rho}_\lambda)/H_{2\lambda}$. The expressions for the derivatives of each simplified parameter are as follows: ${\Gamma_{1\lambda}}' = -1$, ${\Gamma_{2\lambda}}' = 1$, ${H_{1\lambda}}' = -\Gamma_{1\lambda}/H_{1\lambda}$, ${H_{2\lambda}}' = \Gamma_{2\lambda}/H_{2\lambda}$, ${\Phi_{1\lambda}}' = -(1+\tilde{\rho}_\lambda){H_{1\lambda}}'/{H_{1\lambda}}^2$, ${\Phi_{2\lambda}}' = -(1+\tilde{\rho}_\lambda){H_{2\lambda}}'/{H_{2\lambda}}^2$. Thus, by differentiating the expression in Eq. (5) with respect to the variable $\tilde{\lambda}$, the dimensionless stiffness expression can be obtained as follows:
when $-\tilde{a}_\lambda < \tilde{\lambda} < \tilde{a}_\lambda$

$$\begin{aligned}\tilde{K}_\lambda = 1 + \{&\mu_\lambda[1-(1-\tilde{a}_\lambda{}^2)\frac{\Phi_{1\lambda}}{{H_{1\lambda}}^2}] - \nu_\lambda(\Phi_{1\lambda}\\ &-1)^2[(1-\Phi_{1\lambda})(3{\Gamma_{1\lambda}}^2+1-\tilde{a}_\lambda{}^2)\\ &+3{\Gamma_{1\lambda}}^2\Phi_{1\lambda}] + \mu_\lambda[1-(1\\ &-\tilde{a}_\lambda{}^2)\frac{\Phi_{2\lambda}}{{H_{2\lambda}}^2}] - \nu_\lambda(\Phi_{2\lambda}-1)^2[(1\\ &-\Phi_{2\lambda})(3{\Gamma_{2\lambda}}^2+1-\tilde{a}_\lambda{}^2)\\ &+3{\Gamma_{2\lambda}}^2\Phi_{2\lambda}]\}\end{aligned} \tag{6}$$

3.1 Linear tilting springs with pre-stress

When $\nu_\lambda = 0$, the mechanical properties of the device are further simplified as follows

$$\begin{aligned}\tilde{K}_\lambda = 1 + \mu_\lambda(2 &- \frac{(1-\tilde{a}_\lambda{}^2)(1+\tilde{\rho}_\lambda)}{\sqrt{(1+\tilde{\lambda}^2-2\tilde{a}_\lambda\tilde{\lambda})^3}}\\ &- \frac{(1-\tilde{a}_\lambda{}^2)(1+\tilde{\rho}_\lambda)}{\sqrt{(1+\tilde{\lambda}^2+2\tilde{a}_\lambda\tilde{\lambda})^3}})\end{aligned} \tag{7}$$

Setting the system's stiffness to zero at its static equilibrium state leads to the following result

$$\mu_\lambda = -1/2\{1-(1-\tilde{a}_\lambda{}^2)(1+\tilde{\rho}_\lambda)\} \tag{8}$$

Substituting Eq. (8) into Eq. (7) yields

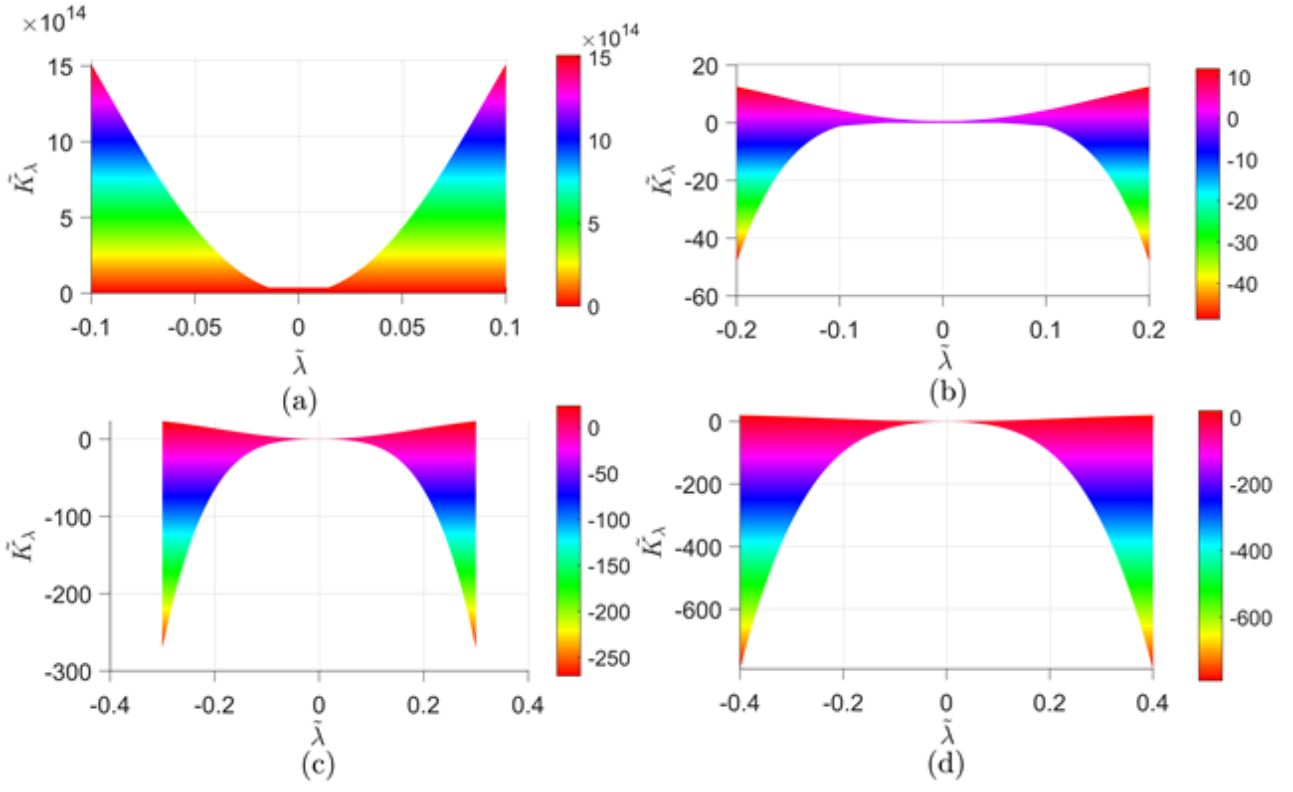

Fig. 8: A 2D mapping diagram of the dimensionless stiffness $\widetilde{K}_\lambda$ as a function of parameter $\tilde{\lambda}$. ($\nu_\lambda \neq 0$); (a) $\tilde{a}_\lambda = 0.1$, (b) $\tilde{a}_\lambda = 0.2$, (c) $\tilde{a}_\lambda = 0.3$, (d) $\tilde{a}_\lambda = 0.4$.

$$\widetilde{K}_\lambda = 1 - \frac{1}{2[1-(1-\tilde{a}_\lambda{}^2)(1+\tilde{\rho}_\lambda)]} \times [2 - \frac{(1-\tilde{a}_\lambda{}^2)(1+\tilde{\rho}_\lambda)}{\sqrt{(\tilde{\lambda}^2-2\tilde{a}_\lambda\tilde{\lambda}+1)^3}} - \frac{(1-\tilde{a}_\lambda{}^2)(1+\tilde{\rho}_\lambda)}{\sqrt{(\tilde{\lambda}^2+2\tilde{a}_\lambda\tilde{\lambda}+1)^3}}] \quad (9)$$

From the equation given by Eq. (9), a 3D surface plot of $\widetilde{K}_\lambda$ of parameters $\tilde{\rho}_\lambda$ and $\tilde{\lambda}$ for different values of $\tilde{a}_\lambda$ can be drawn, as shown in Fig. 4. To better observe the mechanical performance of the QZS isolation system, we have also plotted 2D mapping diagrams of the dimensionless stiffness $\widetilde{K}_\lambda$ as a function of parameter $\tilde{\lambda}$ shown in Fig. 5, as well as the dimensionless stiffness $\widetilde{K}_\lambda$ as a function of parameter $\tilde{\rho}_\lambda$ shown in Fig. 6. From Fig. 4 and Fig. 5, it can be seen that the dimensionless stiffness of the three-dimensional vibration isolator at the static equilibrium position is $\widetilde{K}_\lambda = 0$. Along with the change of the dimensionless pre-compression coefficient $\tilde{\rho}_\lambda$, the stiffness of the system is not always positive throughout the range of compression stroke $\tilde{a}_\lambda$, and sometimes there is a negative stiffness, which is necessary to be avoided in the actual engineering, because the appearance of the negative stiffness will result in the system's unstable characteristics. Therefore, the design parameters of three-dimensional vibration isolator should not only take into account the QZS characteristics at the static equilibrium position, but also ensure that the system is in positive stiffness throughout the compression stroke range.

It can also be seen from Fig. 4 and Fig. 6 that for different values of the $\tilde{a}_\lambda$, the three-dimensional QZS system will always produce an abrupt change in the stiffness value for a particular value of the parameter $\tilde{\rho}_\lambda$. When $\tilde{a}_\lambda = 0.1$, $\widetilde{K}_\lambda$ value forms a sudden variation near $\tilde{\rho}_\lambda = 0.01$; when $\tilde{a}_\lambda = 0.2$, $\widetilde{K}_\lambda$ value forms a sudden variation near $\tilde{\rho}_\lambda = 0.04$; when $\tilde{a}_\lambda = 0.3$, $\widetilde{K}_\lambda$ value forms a sudden variation near $\tilde{\rho}_\lambda = 0.1$; and when $\tilde{a}_\lambda = 0.4$, $\widetilde{K}_\lambda$ value forms a sudden variation near $\tilde{\rho}_\lambda = 0.19$. This is due to the fact that in Eq. (9), it is also necessary to satisfy $2[1-(1-\tilde{a}_\lambda{}^2)(1+\tilde{\rho}_\lambda)] \neq 0$, implying $\tilde{\rho}_\lambda \neq \tilde{a}_\lambda{}^2/(1-\tilde{a}_\lambda{}^2)$, so the parameters selection need to pay attention to avoid specific parameter values, in order to avoid the stiffness value produces a sudden change affecting the vibration isolation performance of the system.

3.2 Softening nonlinear tilting springs with pre-stress

When $\nu_\lambda \neq 0$, Eq. (6) shows the dimensionless stiffness-displacement equation of the three-dimensional vibration isolator. Utilizing the quasi-zero stiffness characteristic, we obtain: $\nu_\lambda = \{1+2\mu_\lambda[1-(1-\tilde{a}_\lambda{}^2)(1+\tilde{\rho}_\lambda)]\}/\{2\tilde{\rho}_\lambda{}^2[3\tilde{a}_\lambda{}^2 - \tilde{\rho}_\lambda(1-\tilde{a}_\lambda{}^2)]\}$, which can be brought into Eq. (6) to get

$$\begin{aligned}\widetilde{K}_\lambda = 1 + \mu_\lambda[2 - (1-\tilde{a}_\lambda{}^2)\frac{\Phi_{1\lambda}}{H_{1\lambda}{}^2} - (1-\tilde{a}_\lambda{}^2)\frac{\Phi_{2\lambda}}{H_{2\lambda}{}^2}] \\ - \frac{1+2\mu_\lambda[1-(1-\tilde{a}_\lambda{}^2)(1+\tilde{\rho}_\lambda)]}{2\tilde{\rho}_\lambda{}^2[3\tilde{a}_\lambda{}^2 - \tilde{\rho}_\lambda(1-\tilde{a}_\lambda{}^2)]} \\ \times \{(\Phi_{1\lambda}-1)^2[3\Gamma_{1\lambda}{}^2 + (\tilde{a}_\lambda{}^2 \\ -1)(\Phi_{1\lambda}-1)] + (\Phi_{2\lambda}-1)^2[3\Gamma_{2\lambda}{}^2 \\ + (\tilde{a}_\lambda{}^2-1)(\Phi_{2\lambda}-1)]\}\end{aligned} \quad (10)$$

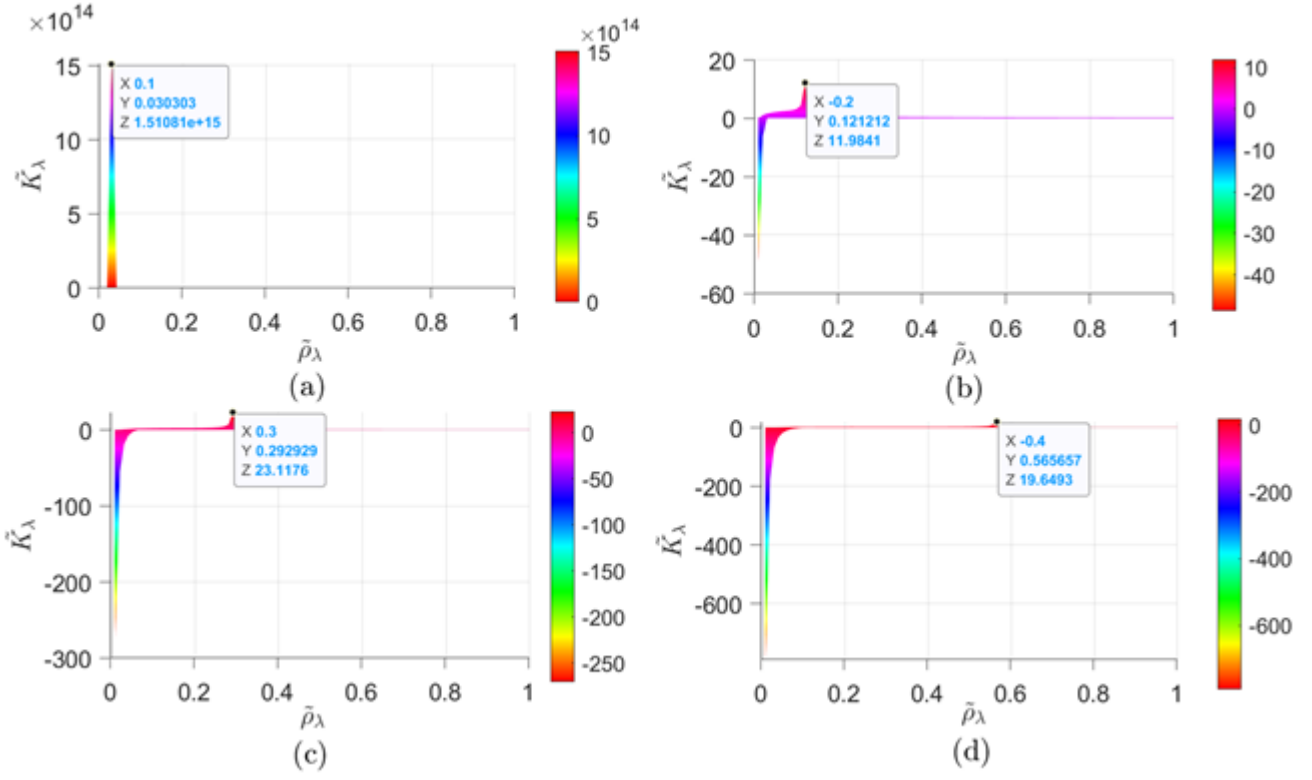

Fig. 9: A 2D mapping diagram of the dimensionless stiffness $\tilde{K}_\lambda$ as a function of parameter $\tilde{\rho}_\lambda$. ($\nu_\lambda \neq 0$); (a) $\tilde{a}_\lambda = 0.1$, (b) $\tilde{a}_\lambda = 0.2$, (c) $\tilde{a}_\lambda = 0.3$, (d) $\tilde{a}_\lambda = 0.4$.

From the equation given by Eq. (10), a 3D surface plot of $\tilde{K}_\lambda$ of the QZS system as a function of parameters $\tilde{\rho}_\lambda$ and $\tilde{\lambda}$ for different values of $\tilde{a}_\lambda$ can be drawn, as shown in Fig. 7. To better observe the mechanical performance of the QZS isolation system, we have also plotted 2D mapping diagrams of the dimensionless stiffness $\tilde{K}_\lambda$ as a function of parameter $\tilde{\lambda}$ shown in Fig. 8, as well as the dimensionless stiffness $\tilde{K}_\lambda$ as a function of parameter $\tilde{\rho}_\lambda$ shown in Fig. 9. It can also be seen from Fig. 8 and Fig. 9 the dimensionless stiffness of the three-dimensional vibration isolator at the static equilibrium position is $\tilde{K}_\lambda = 0$. As the dimensionless pre-compression coefficient changes, the system stiffness may turn negative at times, which causes instability and must be avoided in practice. Therefore, the design of a three-dimensional vibration isolator should ensure positive stiffness throughout the entire compression stroke, in addition to considering the QZS characteristics at the static equilibrium position.

Fig. 7 and Fig. 9 also show that for different values of $\tilde{a}_\lambda$, the three-dimensional QZS system will always experience a sudden change in stiffness at a specific value of parameter $\tilde{\rho}_\lambda$. When $\tilde{a}_\lambda = 0.1$, $\tilde{K}_\lambda$ value forms a sudden variation near around $\tilde{\rho}_\lambda = 0.0303$; when $\tilde{a}_\lambda = 0.2$, $\tilde{K}_\lambda$ value forms an abrupt change around $\tilde{\rho}_\lambda = 0.1212$; when $\tilde{a}_\lambda = 0.3$, $\tilde{K}_\lambda$ value forms a sudden variation near around $\tilde{\rho}_\lambda = 0.1$; and when $\tilde{a}_\lambda = 0.2929$, $\tilde{K}_\lambda$ value forms a sudden variation near around $\tilde{\rho}_\lambda = 0.5656$. This is due to the fact that in Eq. (10), it is also necessary to satisfy $\{1+2\mu_\lambda[1-(1-\tilde{a}_\lambda{}^2)(1+\tilde{\rho}_\lambda)]\}/\{2\tilde{\rho}_\lambda{}^2[3\tilde{a}_\lambda{}^2-\tilde{\rho}_\lambda(1-\tilde{a}_\lambda{}^2)]\} \neq 0$, implying $\tilde{\rho}_\lambda \neq \tilde{a}_\lambda{}^2/(1-\tilde{a}_\lambda{}^2)$, so the parameters selection need to pay attention to avoid specific parameter values, in order to avoid the stiffness value produces a sudden change affecting the vibration isolation performance of the system.

Considering that the stiffness ratio $\mu_\lambda = \{2\nu_\lambda\tilde{\rho}_\lambda{}^2[3\tilde{a}_\lambda{}^2-\tilde{\rho}_\lambda(1-\tilde{a}_\lambda{}^2)]-1\}/\{2[1-(1-\tilde{a}_\lambda{}^2)(1+\tilde{\rho}_\lambda)]\}$ needs to be greater than 0, it is possible to generate a 3D surface plot of μ_λ with respect to parameters $\tilde{\rho}_\lambda$ and ν_λ for $\tilde{a}_\lambda = 0.1$, along with the μ_λ-ν_λ and μ_λ-$\tilde{\rho}_\lambda$ views from various angles, as illustrated in Fig. 10. In Fig. 10, $\nu_\lambda > 0$ is considered because the system adopts a softened cubic stiffness coefficient. The abrupt change in stiffness ratio μ_λ occurs at $\tilde{\rho}_\lambda = \tilde{a}_\lambda{}^2/(1-\tilde{a}_\lambda{}^2)$. It can be observed that when $\tilde{a}_\lambda{}^2/(1-\tilde{a}_\lambda{}^2) < \tilde{\rho}_\lambda < 1$ and $0 < \nu_\lambda < 8$, the stiffness ratio μ_λ remains constantly greater than 0. Fig. 11 and Fig. 12 show the μ_λ-ν_λ view and μ_λ-$\tilde{\rho}_\lambda$ view of the stiffness ratio when $\tilde{a}_\lambda = 0.2\sim0.5$. It can be observed that $\tilde{a}_\lambda$ of the device remains constant and greater than zero when $\tilde{a}_\lambda = 0.2\sim0.4$, $\tilde{a}_\lambda{}^2/(1-\tilde{a}_\lambda{}^2) < \tilde{\rho}_\lambda < 1$, and $0 < \nu_\lambda < 8$. The stiffness ratio $\tilde{a}_\lambda$ of the device is always greater than 0 when $\tilde{a}_\lambda = 0.5$, $\tilde{a}_\lambda{}^2/(1-\tilde{a}_\lambda{}^2) < \tilde{\rho}_\lambda < 1$, $0 < \nu_\lambda < 4$.

4. Optimized design and analysis of three-dimensional QZS isolator

The vertical (Z-axis) and horizontal (X- and Y-axes) QZS isolator parameters are further refined to enlarge the quasi-zero stiffness interval of the three-dimensional system, thereby enhancing its capability for low-frequency vibration attenuation.

4.1 Linear tilting springs with pre-stress

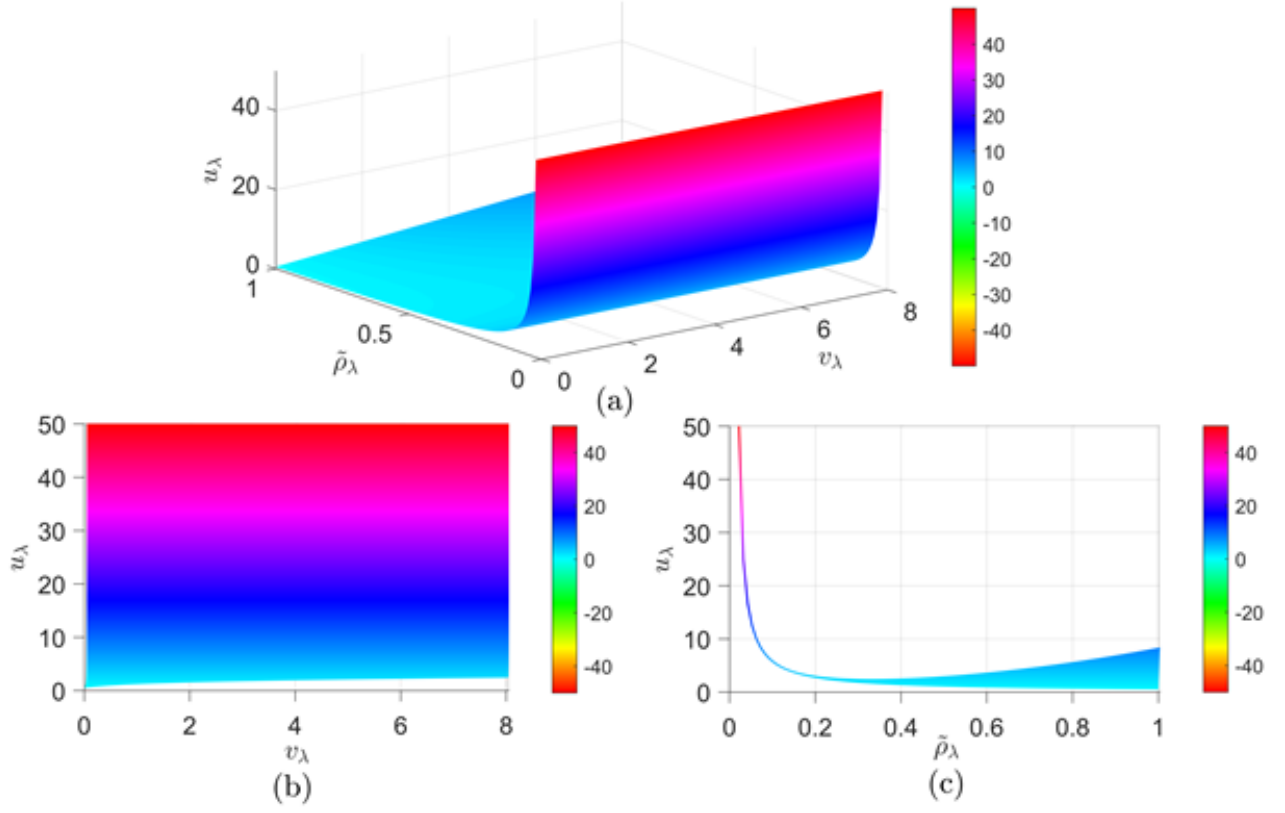

Fig. 10: Stiffness ratio μ_λ with respect to parameters $\tilde{\rho}_\lambda$ and ν_λ; (a) 3D surface plot showing μ_λ as a function of $\tilde{\rho}_\lambda$ and ν_λ, (b) 2D contour map of μ_λ versus ν_λ, (c) 2D contour map of μ_λ versus $\tilde{\rho}_\lambda$.

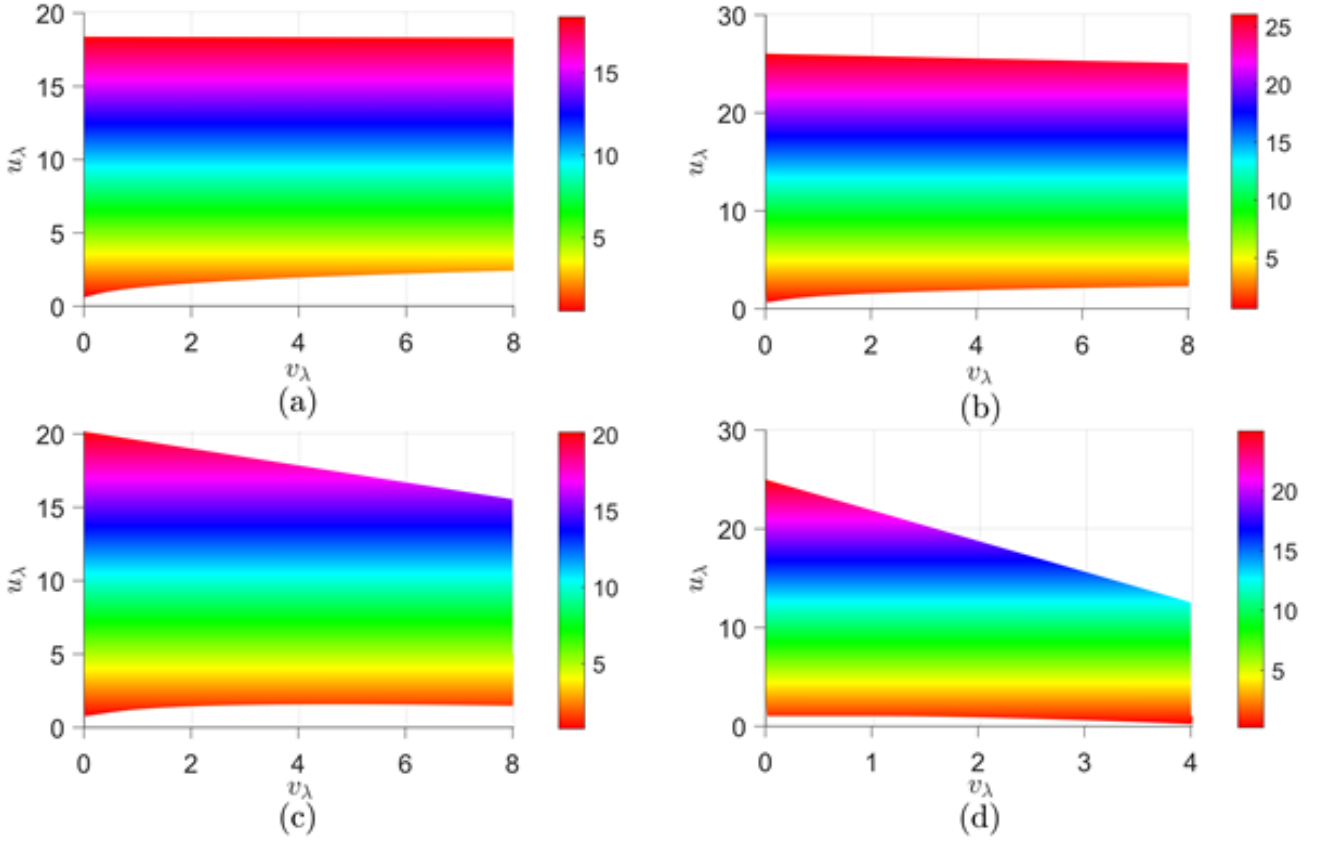

Fig. 11: 2D mapping diagram of the stiffness ratio μ_λ as a function of parameter ν_λ under different parameters of $\tilde{\alpha}_\lambda$; (a) $\tilde{\alpha}_\lambda = 0.2$, (b) $\tilde{\alpha}_\lambda = 0.3$, (c) $\tilde{\alpha}_\lambda = 0.4$, (d) $\tilde{\alpha}_\lambda = 0.5$.

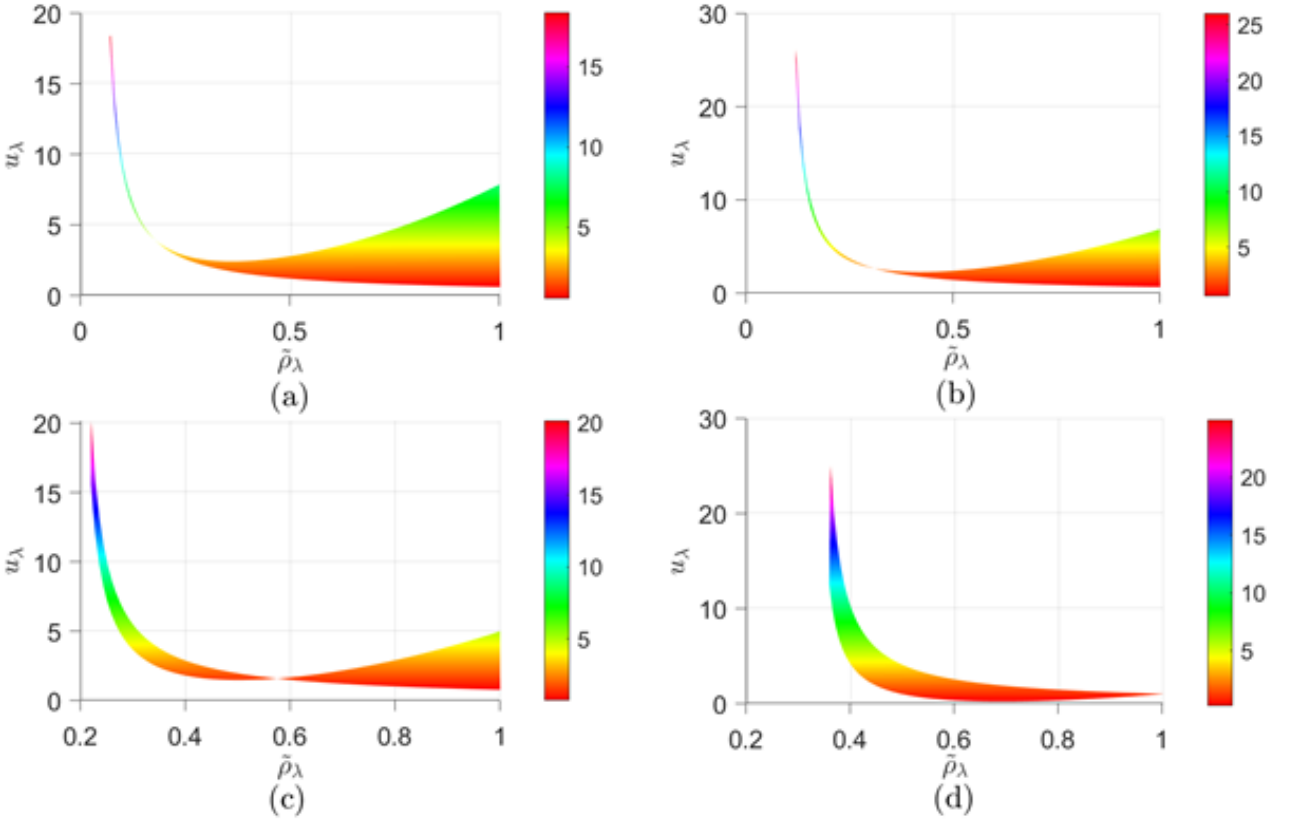

Fig. 12: 2D mapping diagram of the stiffness ratio μ_λ as a function of parameter $\tilde{\rho}_\lambda$ under different parameters of $\tilde{a}_\lambda$; (a) $\tilde{a}_\lambda = 0.2$, (b) $\tilde{a}_\lambda = 0.3$, (c) $\tilde{a}_\lambda = 0.4$, (d) $\tilde{a}_\lambda = 0.5$.

In Eq. (9), we not only need to satisfy $\tilde{\rho}_\lambda \neq {\tilde{a}_\lambda}^2/(1-{\tilde{a}_\lambda}^2)$, considering the stiffness ratio μ_λ is always positive in engineering practice, we also need to satisfy $\tilde{\rho}_\lambda > {\tilde{a}_\lambda}^2/(1-{\tilde{a}_\lambda}^2)$. From this inequality, we choose the following five sets of parameters to satisfy the conditions: $\tilde{a}_\lambda = 0.1$, $\tilde{\rho}_\lambda \in [0.04,1]$; $\tilde{a}_\lambda = 0.2$, $\tilde{\rho}_\lambda \in [0.08,1]$; $\tilde{a}_\lambda = 0.3$, $\tilde{\rho}_\lambda \in [0.14,1]$; $\tilde{a}_\lambda = 0.4$, $\tilde{\rho}_\lambda \in [0.22,1]$; $\tilde{a}_\lambda = 0.5$, $\tilde{\rho}_\lambda \in [0.34,1]$. Under the above five sets of parameter conditions, we have made 3D surface visualizations of $\widetilde{K}_\lambda$ versus $\tilde{\lambda}$ and $\tilde{\rho}_\lambda$, two-dimensional mapping plots of $\widetilde{K}_\lambda$ versus $\tilde{\lambda}$, and two-dimensional mapping plots of $\widetilde{K}_\lambda$ versus $\tilde{\rho}_\lambda$ as comparative analyses to study the performance characteristics of the three-dimensional QZS system, shown in Fig. 13.

To enhance and expand the QZS region of the system, it is essential to position $\widetilde{K}_\lambda$ surface as close as possible to the zero axis, while maintaining positive stiffness characteristics throughout the entire compression stroke. As seen in the 3D surface plot and the $\widetilde{K}_\lambda$-$\tilde{\lambda}$ view in Fig. 13, the dimensionless stiffness $\widetilde{K}_\lambda$ surface undergoes a concave-convex transition within the specified range. Therefore, the critical parameter $\tilde{h}$ value is found by solving for $\widetilde{K}''(0) = 0$, the system's stiffness-displacement relationship can be extended by calculating its higher-order derivatives as shown below.

$$\widetilde{K}_\lambda{}' = -3\mu_\lambda(1-{\tilde{a}_\lambda}^2)(1+\tilde{\rho}_\lambda)\left(\frac{\Gamma_{1\lambda}}{{H_{1\lambda}}^5}-\frac{\Gamma_{2\lambda}}{{H_{2\lambda}}^5}\right) \tag{11}$$

$$\widetilde{K}_\lambda{}'' = 3\mu_\lambda(1-{\tilde{a}_\lambda}^2)(1+\tilde{\rho}_\lambda)\left(\frac{1}{{H_{1\lambda}}^5}+\frac{1}{{H_{2\lambda}}^5}-\frac{5{\Gamma_{1\lambda}}^2}{{H_{1\lambda}}^7}-\frac{5{\Gamma_{2\lambda}}^2}{{H_{2\lambda}}^7}\right) \tag{12}$$

$$\widetilde{K}_\lambda{}''' = 15\mu_\lambda(1-{\tilde{a}_\lambda}^2)(1+\tilde{\rho}_\lambda)\left(\frac{3\Gamma_{1\lambda}}{{H_{1\lambda}}^7}-\frac{3\Gamma_{2\lambda}}{{H_{2\lambda}}^7}-\frac{7{\Gamma_{1\lambda}}^3}{{H_{1\lambda}}^9}+\frac{7{\Gamma_{2\lambda}}^3}{{H_{2\lambda}}^9}\right) \tag{13}$$

$$\widetilde{K}_\lambda{}'''' = -45\mu_\lambda(1-{\tilde{a}_\lambda}^2)(1+\tilde{\rho}_\lambda)\left(\frac{1}{{H_{1\lambda}}^7}+\frac{1}{{H_{2\lambda}}^7}-\frac{14{\Gamma_{1\lambda}}^2}{{H_{1\lambda}}^9}-\frac{14{\Gamma_{2\lambda}}^2}{{H_{2\lambda}}^9}+\frac{21{\Gamma_{1\lambda}}^4}{{H_{1\lambda}}^{11}}+\frac{21{\Gamma_{2\lambda}}^4}{{H_{2\lambda}}^{11}}\right) \tag{14}$$

Eq. (11) through (14) can be further obtained and expressed in the following form.

$$\tilde{f}_\lambda(0) = 0 \quad , \quad \widetilde{K}_\lambda(0) = 1 + 2\mu_\lambda[1-(1-{\tilde{a}_\lambda}^2)(1+\tilde{\rho}_\lambda)] \quad , \quad \widetilde{K}_\lambda{}'(0) = 0 \quad , \quad \widetilde{K}_\lambda{}''(0) = 6\mu_\lambda(1-{\tilde{a}_\lambda}^2)(1+\tilde{\rho}_\lambda)(1-5{\tilde{a}_\lambda}^2) \quad , \quad \widetilde{K}_\lambda{}'''(0) = 0 \quad , \quad \widetilde{K}_\lambda{}''''(0) = -90\mu_\lambda(1-{\tilde{a}_\lambda}^2)(1+\tilde{\rho}_\lambda)(1-14{\tilde{a}_\lambda}^2+21{\tilde{a}_\lambda}^4).$$

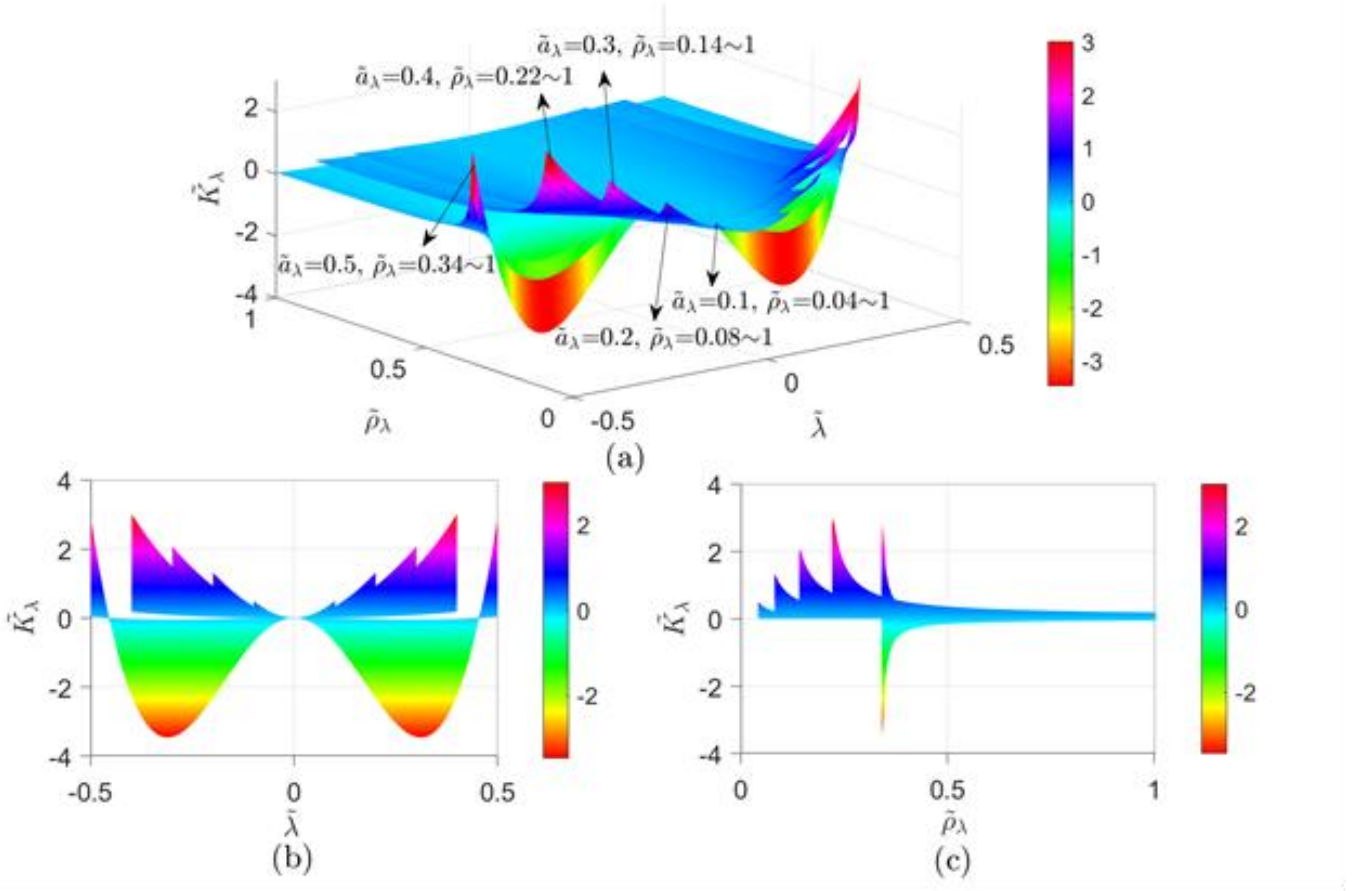

Fig. 13: Dimensionless stiffness $\tilde{K}_\lambda$ with parameters $\tilde{\lambda}$ and $\tilde{\rho}_\lambda$ under $\tilde{\rho}_\lambda > \tilde{a}_\lambda{}^2/(1-\tilde{a}_\lambda{}^2)$; (a) 3D plot of $\tilde{K}_\lambda$ versus $\tilde{\lambda}$ and $\tilde{\rho}_\lambda$, (b) 2D map of $\tilde{K}_\lambda$ versus $\tilde{\lambda}$, (c) 2D map of $\tilde{K}_\lambda$ versus $\tilde{\rho}_\lambda$.

When the system displacement $\tilde{\lambda}$ is relatively small, Eq. (5) can be linearized by applying a Taylor series expansion around $\tilde{\lambda}=0$, leading to the following simplified expression.

$$\begin{aligned}\tilde{f}_\lambda = \tilde{\lambda} + 2\mu_\lambda[1-(1-\tilde{a}_\lambda{}^2)(1+\tilde{\rho}_\lambda)]\tilde{\lambda} + \mu_\lambda(1 \\ -\tilde{a}_\lambda{}^2)(1+\tilde{\rho}_\lambda)(1-5\tilde{a}_\lambda{}^2)\tilde{\lambda}^3 \\ -0.75\mu_\lambda(1-\tilde{a}_\lambda{}^2)(1+\tilde{\rho}_\lambda)(1 \\ -14\tilde{a}_\lambda{}^2+21\tilde{a}_\lambda{}^4)\tilde{\lambda}^5 + o(\tilde{\lambda}^5)\end{aligned} \quad (15)$$

For the three-dimensional QZS isolation system, when $\tilde{\rho}_\lambda \neq \tilde{a}_\lambda{}^2/(1-\tilde{a}_\lambda{}^2)$, $\tilde{K}_\lambda(0)=0$. At this point, the Taylor series expansion of Eq. (15) at $\tilde{\lambda}=0$ is as follows

$$\begin{aligned}&\tilde{f}_\lambda \\ &= -\frac{0.5(1-\tilde{a}_\lambda{}^2)(1+\tilde{\rho}_\lambda)(1-5\tilde{a}_\lambda{}^2)}{1-(1-\tilde{a}_\lambda{}^2)(1+\tilde{\rho}_\lambda)}\tilde{\lambda}^3 \\ &+ \frac{0.375(1-\tilde{a}_\lambda{}^2)(1+\tilde{\rho}_\lambda)(1-14\tilde{a}_\lambda{}^2+21\tilde{a}_\lambda{}^4)}{1-(1-\tilde{a}_\lambda{}^2)(1+\tilde{\rho}_\lambda)}\tilde{\lambda}^5 \\ &+ o(\tilde{\lambda}^5)\end{aligned} \quad (16)$$

Eq. (16) is obtained from the Taylor expansion of Eq. (15) at small displacement, showing that the restoring force is mainly governed by the cubic and quintic terms, which reflects the quasi-zero stiffness property. When $\tilde{\lambda}=0$, $\tilde{K}_\lambda{}''(0)=0$, $(1-\tilde{a}_\lambda{}^2)(1+\tilde{\rho}_\lambda)(1-5\tilde{a}_\lambda{}^2)=0$, which leads to $\tilde{a}_\lambda = 0.447$, $\tilde{\rho}_\lambda \neq 0.25$, $\mu_\lambda = -2.5/(1-4\tilde{\rho}_\lambda)$, then the Taylor series expansion of Eq. (15) at $\tilde{\lambda}=0$ is

$$\tilde{f}_\lambda = -1.44\frac{1+\tilde{\rho}_\lambda}{1-4\tilde{\rho}_\lambda}\tilde{\lambda}^5 + o(\tilde{\lambda}^5) \quad (17)$$

Eq. (17) corresponds to the specific parameter case, where the cubic term vanishes and the quintic term dominates, indicating that the stiffness near equilibrium is almost zero and thus beneficial for vibration isolation. At this point, the parameter $\tilde{a}_\lambda = 0.447$ is solved for, and the corresponding sharp transition around $\tilde{K}$ value is at $\tilde{\delta}=0.25$, and the pre-compression coefficient needs to satisfy $\tilde{\delta} > 0.25$. Fig. 14 show the 3D surface visualizations of $\tilde{K}_\lambda$ versus $\tilde{\lambda}$ and $\tilde{\rho}_\lambda$, and also the $\tilde{K}_\lambda$-$\tilde{\lambda}$ view and $\tilde{K}_\lambda$-$\tilde{\rho}_\lambda$ view from different viewpoints when $\tilde{a}_\lambda = 0.447$. It is evident that the QZS range of the device expands as the value of $\tilde{\rho}_\lambda$ increases, and the value of $\tilde{K}_\lambda$ reaches its maximum value at the compression stroke limit of the device, and the magnitude of the peak decreases along with the increase of $\tilde{\rho}_\lambda$. When the system parameter $\tilde{a}_\lambda$ is fixed, the pre-compression coefficient $\tilde{\rho}_\lambda$ of the vibration isolation system is inversely proportional to the stiffness ratio μ_λ, meaning that as $\tilde{\rho}_\lambda$ increases μ_λ decreases accordingly. Therefore, in practical engineering applications, there are two corresponding design methods, the first is to fix the stiffness ratio μ_λ, and then determine the corresponding pre-compression coefficient $\tilde{\rho}_\lambda$ of the tilting spring by the values of $\tilde{a}_\lambda$ and μ_λ.

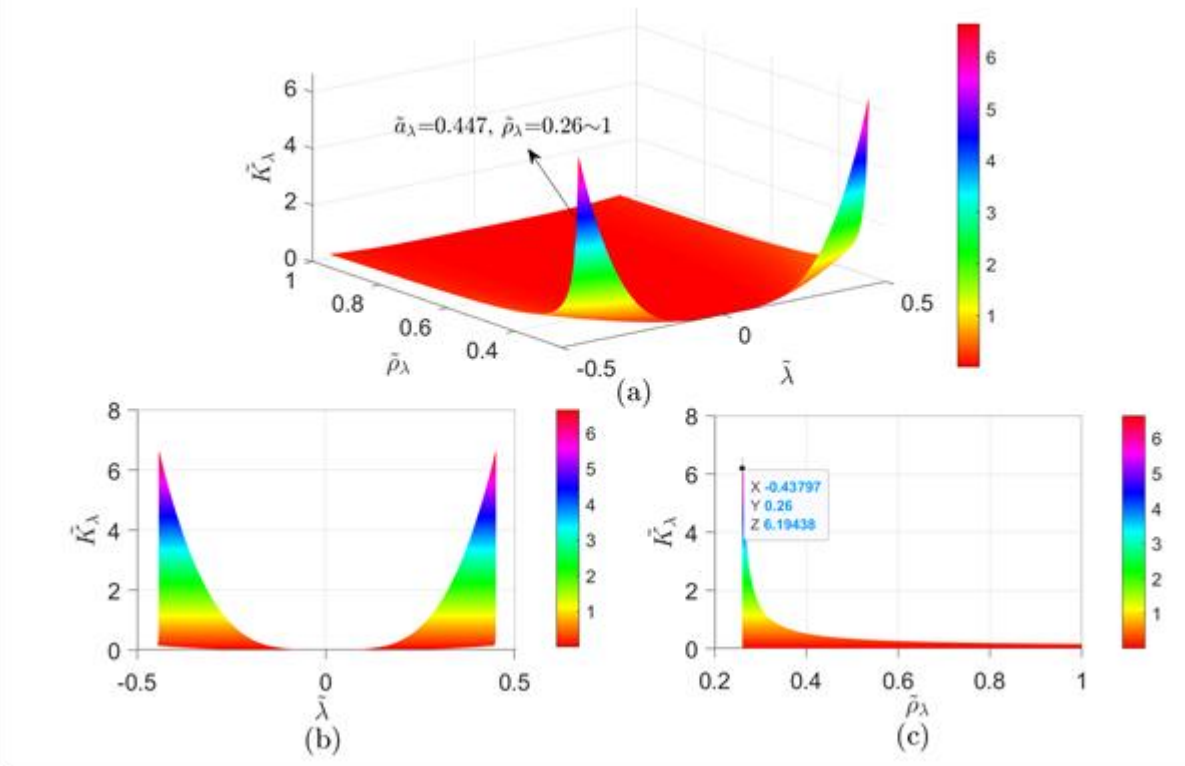

Fig. 14: Dimensionless stiffness $\tilde{K}_\lambda$ versus $\tilde{\lambda}$ and $\tilde{\rho}_\lambda$ when $\tilde{a}_\lambda = 0.447$; (a) 3D surface plot of $\tilde{K}_\lambda$ versus $\tilde{\lambda}$ and $\tilde{\rho}_\lambda$, (b) 2D map of $\tilde{K}_\lambda$ versus $\tilde{\lambda}$, (c) 2D map of $\tilde{K}_\lambda$ versus $\tilde{\rho}_\lambda$.

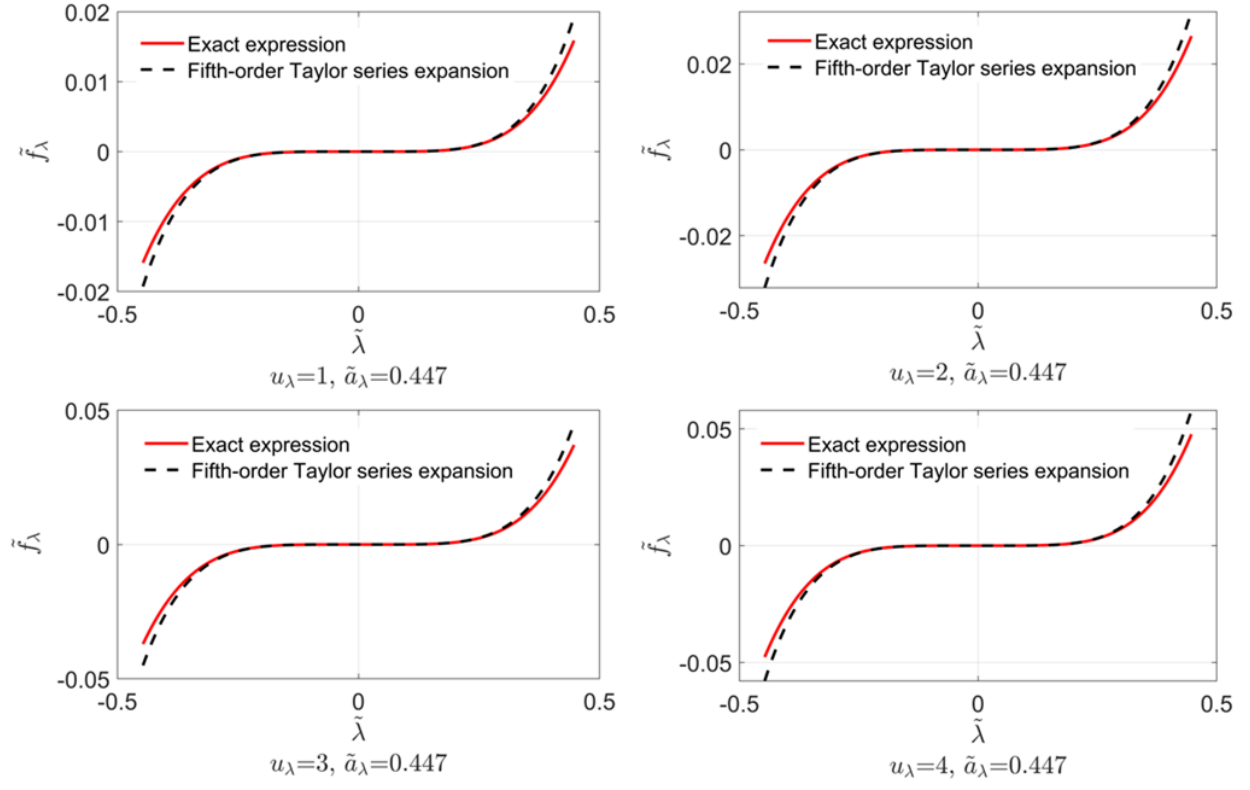

Fig. 15: Comparison of dimensionless force-displacement curves and Taylor series results for the 3D QZS isolator without cubic stiffness.

In this case, it is necessary to consider whether the pre-compression of the tilting spring is able to meet the requirements. The second is to fix the pre-compression coefficient $\tilde{\rho}_\lambda$ of the tilting spring, and then to determine the corresponding stiffness ratio μ_λ by the values of $\tilde{a}_\lambda$ and $\tilde{\rho}_\lambda$. Considering that it is more difficult to control $\tilde{\rho}_\lambda$ in

engineering design, and that the stiffness of tilting springs and vertical coil springs can be easily adjusted in processing, we generally consider the second design method. Therefore, when $\nu_\lambda = 0$, four distinct sets of optimization parameters for the QZS isolation system can be obtained, as outlined below: $\mu_\lambda = 1$, $\tilde{a}_\lambda = 0.447$, $\tilde{\rho}_\lambda = 0.876$, $r = 1.0805$; $\mu_\lambda = 2$, $\tilde{a}_\lambda = 0.447$, $\tilde{\rho}_\lambda = 0.562$, $r = 1.8017$; $\mu_\lambda = 3$, $\tilde{a}_\lambda = 0.447$, $\tilde{\rho}_\lambda = 0.458$, $r = 2.5236$; $\mu_\lambda = 4$, $\tilde{a}_\lambda = 0.447$, $\tilde{\rho}_\lambda = 0.406$, $r = 3.2462$. Fig. 15 presents the comparison between the exact expression for the dimensionless force-displacement and its Taylor series expansion for four different sets of optimization parameters. Due to the large value of $\tilde{a}_\lambda$, the Taylor series expansion performs poorly at the end of the system's compression travel. The error between the approximate and exact expressions of the dimensionless force increases as the system's displacement grows.

4.2 Softening nonlinear tilting springs with pre-stress

As observed from Fig. 10, Fig. 11 and Fig. 12, when $\tilde{\rho}_\lambda > \tilde{a}_\lambda{}^2/(1-\tilde{a}_\lambda{}^2)$ and $0 < \nu_\lambda < 4$, the stiffness ratio $\mu_\lambda > 0$ can satisfy the needs of practical engineering. According to this parameter selection range, further made when $\nu_\lambda = 0.05,0.25,0.5,0.75$, respectively, in different parameters $\tilde{a}_\lambda = 0.1$, $\tilde{\rho}_\lambda \in [0.04,5]$; $\tilde{a}_\lambda = 0.2$, $\tilde{\rho}_\lambda \in [0.08,5]$; $\tilde{a}_\lambda = 0.3$, $\tilde{\rho}_\lambda \in [0.14,5]$; $\tilde{a}_\lambda = 0.4$, $\tilde{\rho}_\lambda \in [0.22,5]$, under $\widetilde{K}_\lambda$ and parameters $\tilde{\lambda}$ and $\tilde{\rho}_\lambda$ of the three-dimensional surface graph, as shown in Fig. 16. As observed, for different values of ν_λ and $\tilde{a}_\lambda$, the three-dimensional surfaces exhibit a transformation in concavity and convexity at a particular value of $\tilde{\rho}_\lambda$. For small values of $\tilde{\rho}_\lambda$, $\widetilde{K}_\lambda$ is a three-dimensional concave surface, and for large values of $\tilde{\rho}_\lambda$, $\widetilde{K}_\lambda$ is a three-dimensional convex surface. In order to see this property more clearly, we take $\nu_\lambda = 0.5$, $\tilde{a}_\lambda = 0.1$, and $\tilde{\rho}_\lambda \in [0.04,5]$, and make a 3D surface visualization of $\widetilde{K}_\lambda$ with $\tilde{\lambda}$ and $\tilde{\rho}_\lambda$, along with $\widetilde{K}_\lambda$-$\tilde{\lambda}$ view and $\widetilde{K}_\lambda$-$\tilde{\rho}_\lambda$ view from different viewpoints, as shown in Fig. 17. The concavity of the 3D surface maps probably shifts around $\tilde{\rho}_\lambda = 1.042$.

Similarly when $\nu_\lambda \neq 0$, to enhance and broaden the QZS region of the vibration isolation system, it is crucial to keep $\widetilde{K}_\lambda$ surface as close as possible to the zero axis at the static equilibrium position ($\tilde{\lambda} = 0$), while simultaneously maintaining positive stiffness characteristics throughout the entire compression stroke. As seen in the plot of $\widetilde{K}_\lambda$ and the $\widetilde{K}_\lambda$-$\tilde{\rho}_\lambda$ view in Fig. 17, the $\widetilde{K}_\lambda$ surface exhibits a shift between concave and convex behavior at a specific value of $\tilde{\rho}_\lambda$. Thus, the critical value of parameter $\tilde{\rho}_\lambda$ can be derived by solving for $\widetilde{K}_\lambda'' = 0$.

When $-\tilde{a}_\lambda < \tilde{\lambda} < \tilde{a}_\lambda$, according to Eq. (10), the relationship between system stiffness and displacement can be further obtained by calculating derivatives of different orders as shown below.

$$\widetilde{K}_\lambda{}' = -3\mu_\lambda(1-\tilde{a}_\lambda{}^2)(1+\tilde{\rho}_\lambda)\left(\frac{\Gamma_{1\lambda}}{H_{1\lambda}{}^5}-\frac{\Gamma_{2\lambda}}{H_{2\lambda}{}^5}\right)-3\nu_\lambda\{\Gamma_{1\lambda}[2\Gamma_{1\lambda}{}^2\frac{\Phi_{1\lambda}(\Phi_{1\lambda}-1)}{H_{1\lambda}{}^2}+(\tilde{a}_\lambda{}^2-1)\frac{\Phi_{1\lambda}(\Phi_{1\lambda}-1)^2}{H_{1\lambda}{}^2} \\ -2(\Phi_{1\lambda}-1)^2]-\Gamma_{2\lambda}[2\Gamma_{2\lambda}{}^2\frac{\Phi_{2\lambda}(\Phi_{2\lambda}-1)}{H_{2\lambda}{}^2}+(\tilde{a}_\lambda{}^2-1)\frac{\Phi_{2\lambda}(\Phi_{2\lambda}-1)^2}{H_{2\lambda}{}^2}-2(\Phi_{2\lambda}-1)^2]\} \tag{18}$$

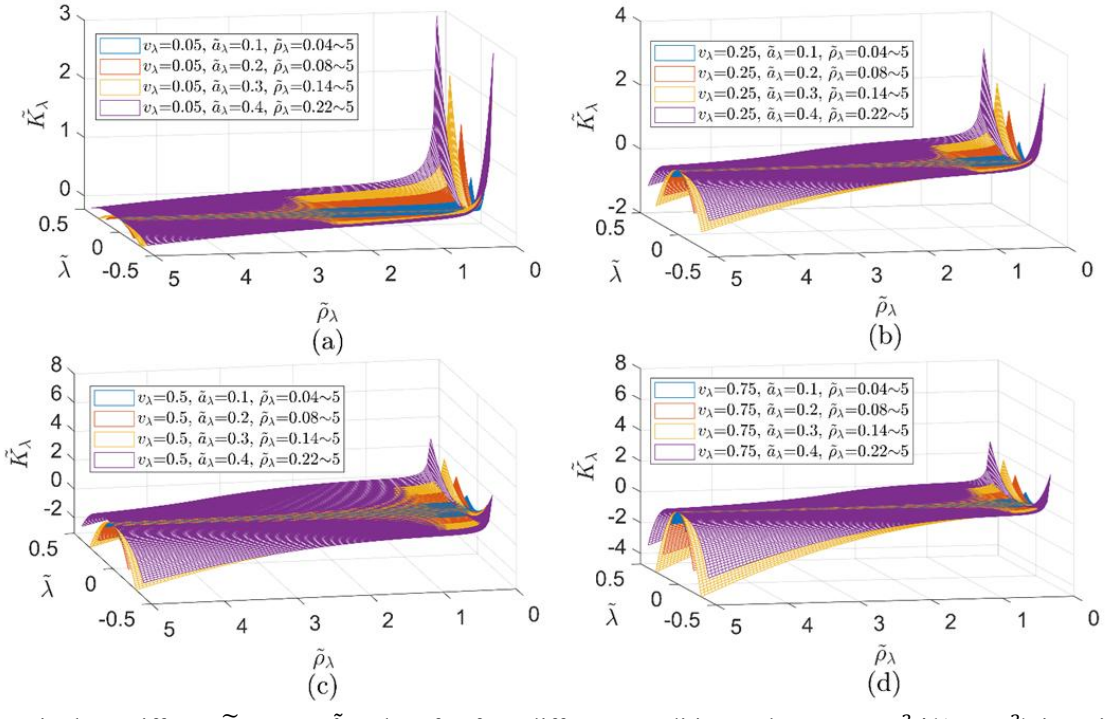

Fig. 16: Dimensionless stiffness $\widetilde{K}_\lambda$ versus $\tilde{\lambda}$ and $\tilde{\rho}_\lambda$ for four different conditions when $\tilde{\rho}_\lambda > \tilde{a}_\lambda{}^2/(1-\tilde{a}_\lambda{}^2)$ is satisfied; (a) $\nu_\lambda = 0.05$, (b) $\nu_\lambda = 0.25$, (c) $\nu_\lambda = 0.5$, (c) $\nu_\lambda = 0.75$.

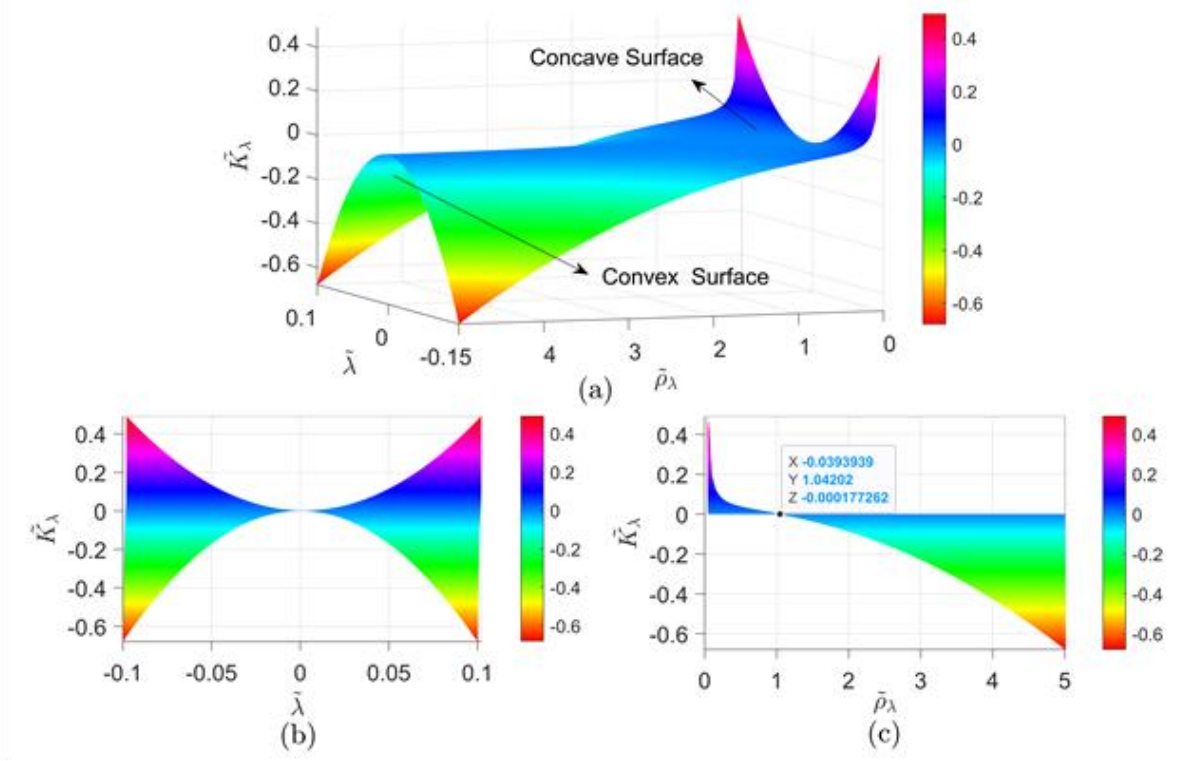

Fig. 17: Dimensionless stiffness $\tilde{K}_\lambda$ versus $\tilde{\lambda}$ and $\tilde{\rho}_\lambda$ when $\nu_\lambda = 0.5$, $\tilde{a}_\lambda = 0.1$, $\tilde{\rho}_\lambda \in [0.04,5]$; (a) 3D surface plot of $\tilde{K}_\lambda$ versus $\tilde{\lambda}$ and $\tilde{\rho}_\lambda$, (b) 2D map of $\tilde{K}_\lambda$ versus $\tilde{\lambda}$, (c) 2D map of $\tilde{K}_\lambda$ versus $\tilde{\rho}_\lambda$.

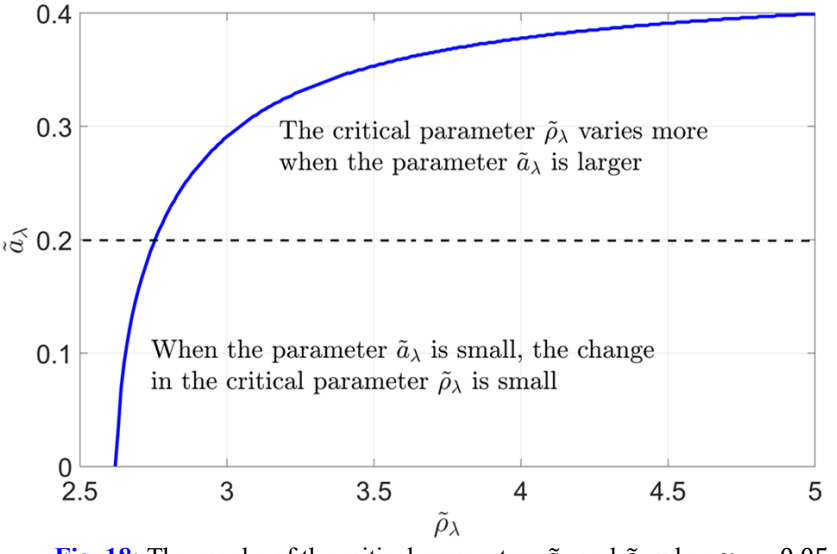

Fig. 18: The graphs of the critical parameters $\tilde{a}_\lambda$ and $\tilde{\rho}_\lambda$ when $\nu_\lambda = 0.05$.

$$\begin{aligned}\tilde{K}_\lambda'' = {} & 3\mu_\lambda(1-\tilde{a}_\lambda{}^2)(1+\tilde{\rho}_\lambda)\left(\frac{1}{H_{1\lambda}{}^5}+\frac{1}{H_{2\lambda}{}^5}-\frac{5\Gamma_{1\lambda}{}^2}{H_{1\lambda}{}^7}-\frac{5\Gamma_{2\lambda}{}^2}{H_{2\lambda}{}^7}\right)-3\nu_\lambda\{2(\Phi_{1\lambda}-1)^2 \\ & -\frac{\Phi_{1\lambda}(\Phi_{1\lambda}-1)[(\tilde{a}_\lambda{}^2-1)(\Phi_{1\lambda}-1)+10\Gamma_{1\lambda}{}^2]}{H_{1\lambda}{}^2} \\ & +\frac{\Gamma_{1\lambda}{}^2\Phi_{1\lambda}(\Phi_{1\lambda}-1)[(\tilde{a}_\lambda{}^2-1)(5\Phi_{1\lambda}-3)+8\Gamma_{1\lambda}{}^2]+2\Gamma_{1\lambda}{}^4\Phi_{1\lambda}}{H_{1\lambda}{}^4}+2(\Phi_{2\lambda}-1)^2 \\ & -\frac{\Phi_{2\lambda}(\Phi_{2\lambda}-1)[(\tilde{a}_\lambda{}^2-1)(\Phi_{2\lambda}-1)+10\Gamma_{2\lambda}{}^2]}{H_{2\lambda}{}^2} \\ & +\frac{\Gamma_{2\lambda}{}^2\Phi_{2\lambda}(\Phi_{2\lambda}-1)[(\tilde{a}_\lambda{}^2-1)(5\Phi_{2\lambda}-3)+8\Gamma_{2\lambda}{}^2]+2\Gamma_{2\lambda}{}^4\Phi_{2\lambda}}{H_{2\lambda}{}^4}\}\end{aligned} \tag{19}$$

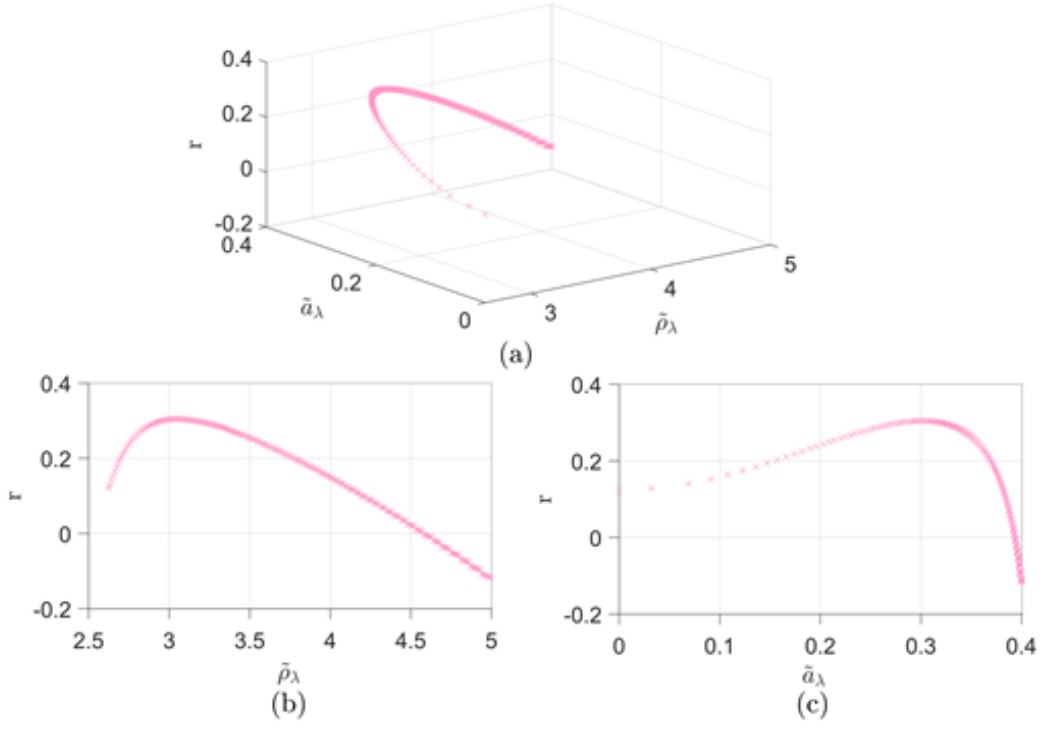

Fig. 19: Plot of nonlinear coefficients r versus parameters $\tilde{a}_\lambda$ and $\tilde{\rho}_\lambda$ when $\nu_\lambda = 0.05$; (a) 3D surface plot, (b) 2D mapping diagram r -$\tilde{\rho}_\lambda$, (c) 2D mapping diagram r -$\tilde{a}_\lambda$.

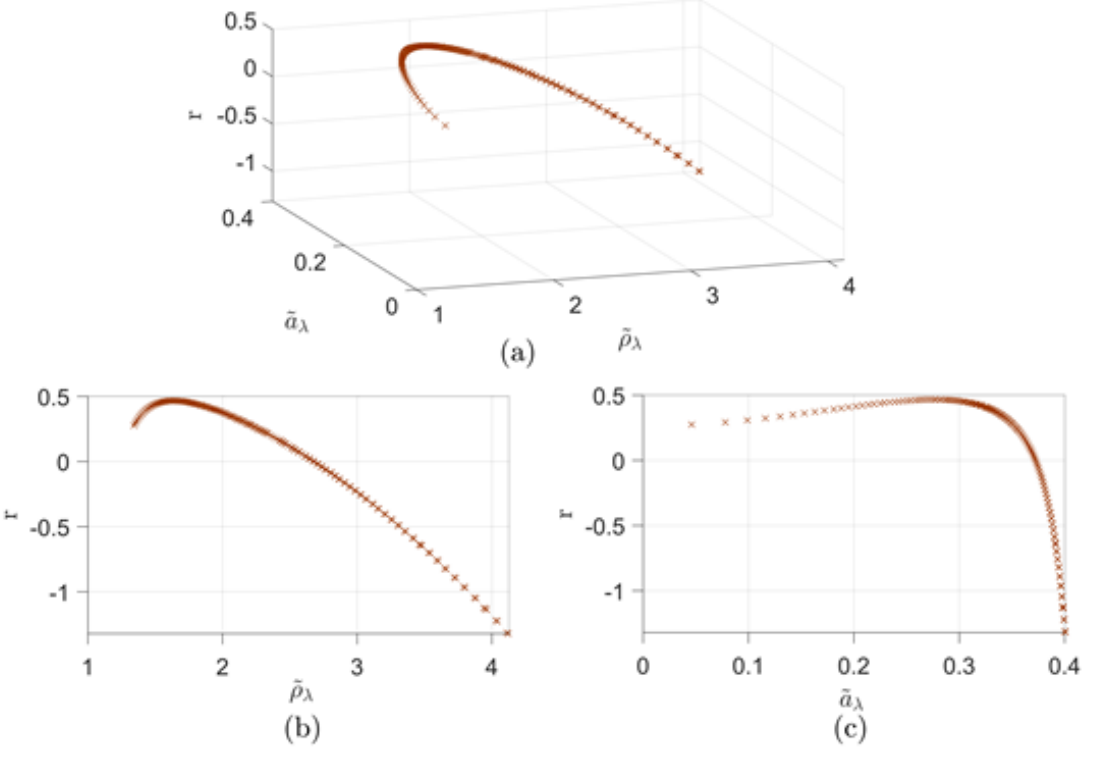

Fig. 20: Plot of nonlinear coefficients r versus parameters $\tilde{a}_\lambda$ and $\tilde{\rho}_\lambda$ when $\nu_\lambda = 0.25$; (a) 3D surface plot, (b) 2D mapping diagram r -$\tilde{\rho}_\lambda$, (c) 2D mapping diagram r -$\tilde{a}_\lambda$.

$$\mu_\lambda(1-\tilde{a}_\lambda{}^2)(1-5\tilde{a}_\lambda{}^2)(1+\tilde{\rho}_\lambda)-\frac{1+2\mu_\lambda[1-(1-\tilde{a}_\lambda{}^2)(1+\tilde{\rho}_\lambda)]}{2\tilde{\rho}_\lambda{}^2[3\tilde{a}_\lambda{}^2-\tilde{\rho}_\lambda(1-\tilde{a}_\lambda{}^2)]}\times[(5\tilde{a}_\lambda{}^4-6\tilde{a}_\lambda{}^2+1)\tilde{\rho}_\lambda{}^3+(15\tilde{a}_\lambda{}^4-18\tilde{a}_\lambda{}^2+3)\tilde{\rho}_\lambda{}^2+(12\tilde{a}_\lambda{}^4-12\tilde{a}_\lambda{}^2)\tilde{\rho}_\lambda+2\tilde{a}_\lambda{}^4]=0 \quad (20)$$

Eqs. (18) and (19) represent the first and second derivatives of the dimensionless stiffness. Together, they are used to analyze how the system stiffness varies with displacement and pre-compression, and to determine the critical points and curvature changes that define the boundaries of the quasi-zero stiffness region. The equation for $\widetilde{K}_{\lambda}''(0)=0$ is provided in Eq. (20), and the corresponding curves for the critical parameter $\tilde{\rho}_{\lambda}$ and $\tilde{a}_{\lambda}$ values, when $\widetilde{K}_{\lambda}''(0)=0$ and $\nu_{\lambda}=0.05$, are illustrated in Fig. 18. These curves demonstrate that, as the parameter $\tilde{a}_{\lambda}$ decreases, the variation in the critical parameter $\tilde{\rho}_{\lambda}$ becomes smaller. Conversely, as $\tilde{a}_{\lambda}$ increases, the change in $\tilde{\rho}_{\lambda}$ becomes more pronounced, especially when $\tilde{a}_{\lambda}>0.3$, where the variation in $\tilde{\rho}_{\lambda}$ becomes significantly larger. In practical engineering applications, the compression factor of the spring element is constrained, and therefore, the optimal selection of the $\tilde{a}_{\lambda}$ value should aim to be as minimal as possible.

$$\begin{aligned}\widetilde{K}_{\lambda}'''(\tilde{\lambda}) = {} & 15\mu_{\lambda}(1-\tilde{a}_{\lambda}^{2})(1+\tilde{\rho}_{\lambda})\left(\frac{3\Gamma_{1\lambda}}{H_{1\lambda}^{7}}-\frac{3\Gamma_{2\lambda}}{H_{2\lambda}^{7}}-\frac{7\Gamma_{1\lambda}^{3}}{H_{1\lambda}^{9}}+\frac{7\Gamma_{2\lambda}^{3}}{H_{2\lambda}^{9}}\right)-3\nu_{\lambda}\times\{\Gamma_{1\lambda}\Phi_{1\lambda}\times[24\frac{\Phi_{1\lambda}-1}{H_{1\lambda}^{2}}\\ & -\frac{(\tilde{a}_{\lambda}^{2}-1)(15\Phi_{1\lambda}^{2}-24\Phi_{1\lambda}+9)+2\Gamma_{1\lambda}^{4}(36\Phi_{1\lambda}-31)+8}{H_{1\lambda}^{4}}\\ & +\frac{\Gamma_{1\lambda}^{2}[(\tilde{a}_{\lambda}^{2}-1)(35\Phi_{1\lambda}^{2}-48\Phi_{1\lambda}+15)+2\Gamma_{1\lambda}^{2}(24\Phi_{1\lambda}-15)]}{H_{1\lambda}^{6}}]-\Gamma_{2\lambda}\Phi_{2\lambda}\times[24\frac{\Phi_{2\lambda}-1}{H_{2\lambda}^{2}}\\ & -\frac{(\tilde{a}_{\lambda}^{2}-1)(15\Phi_{2\lambda}^{2}-24\Phi_{2\lambda}+9)+2\Gamma_{2\lambda}^{4}(36\Phi_{2\lambda}-31)+8}{H_{2\lambda}^{4}}\\ & +\frac{\Gamma_{2\lambda}^{2}[(\tilde{a}_{\lambda}^{2}-1)(35\Phi_{2\lambda}^{2}-48\Phi_{2\lambda}+15)+2\Gamma_{2\lambda}^{2}(24\Phi_{2\lambda}-15)]}{H_{2\lambda}^{6}}]\}\end{aligned} \tag{21}$$

$$\begin{aligned}\widetilde{K}_{\lambda}''''(\tilde{\lambda}) = {} & -45\mu_{\lambda}(1-\tilde{a}_{\lambda}^{2})(1+\tilde{\rho}_{\lambda})\left(\frac{1}{H_{1\lambda}^{7}}+\frac{1}{H_{2\lambda}^{7}}-\frac{14\Gamma_{1\lambda}^{2}}{H_{1\lambda}^{9}}-\frac{14\Gamma_{2\lambda}^{2}}{H_{2\lambda}^{9}}+\frac{21\Gamma_{1\lambda}^{4}}{H_{1\lambda}^{11}}+\frac{21\Gamma_{2\lambda}^{4}}{H_{2\lambda}^{11}}\right)-3\nu_{\lambda}\times\{\Phi_{1\lambda}[\frac{24(1-\Phi_{1\lambda})}{H_{1\lambda}^{2}}\\ & +\frac{8+(\tilde{a}_{\lambda}^{2}-1)(15\Phi_{1\lambda}^{2}-24\Phi_{1\lambda}+9)+24\Gamma_{1\lambda}^{2}(4\Phi_{1\lambda}-3)+10\Gamma_{1\lambda}^{4}(36\Phi_{1\lambda}-31)}{H_{1\lambda}^{4}}\\ & -\frac{6\Gamma_{1\lambda}^{2}(\tilde{a}_{\lambda}^{2}-1)(35\Phi_{1\lambda}^{2}-48\Phi_{1\lambda}+15)+10\Gamma_{1\lambda}^{4}(24\Phi_{1\lambda}-15)+2\Gamma_{1\lambda}^{6}(216\Phi_{1\lambda}-55)+40\Gamma_{1\lambda}^{2}}{H_{1\lambda}^{6}}\\ & +\frac{3\Gamma_{1\lambda}^{4}(\tilde{a}_{\lambda}^{2}-1)(35\Phi_{1\lambda}^{2}-32\Phi_{1\lambda}+5)+2\Gamma_{1\lambda}^{6}(48\Phi_{1\lambda}-15)}{H_{1\lambda}^{8}}\\ & +\frac{6\Gamma_{1\lambda}^{4}(\tilde{a}_{\lambda}^{2}-1)(35\Phi_{1\lambda}^{2}-48\Phi_{1\lambda}+15)+12\Gamma_{1\lambda}^{6}(24\Phi_{1\lambda}-15)}{H_{1\lambda}^{10}}]+\Phi_{2\lambda}[\frac{24(1-\Phi_{2\lambda})}{H_{2\lambda}^{2}}\\ & +\frac{8+(\tilde{a}_{\lambda}^{2}-1)(15\Phi_{2\lambda}^{2}-24\Phi_{2\lambda}+9)+24\Gamma_{2\lambda}^{2}(4\Phi_{2\lambda}-3)+10\Gamma_{2\lambda}^{4}(36\Phi_{2\lambda}-31)}{H_{2\lambda}^{4}}\\ & -\frac{6\Gamma_{2\lambda}^{2}(\tilde{a}_{\lambda}^{2}-1)(35\Phi_{2\lambda}^{2}-48\Phi_{2\lambda}+15)+10\Gamma_{2\lambda}^{4}(24\Phi_{2\lambda}-15)+2\Gamma_{2\lambda}^{6}(216\Phi_{2\lambda}-55)+40\Gamma_{2\lambda}^{2}}{H_{2\lambda}^{6}}\\ & +\frac{3\Gamma_{2\lambda}^{4}(\tilde{a}_{\lambda}^{2}-1)(35\Phi_{2\lambda}^{2}-32\Phi_{2\lambda}+5)+2\Gamma_{2\lambda}^{6}(48\Phi_{2\lambda}-15)}{H_{2\lambda}^{8}}\\ & +\frac{6\Gamma_{2\lambda}^{4}(\tilde{a}_{\lambda}^{2}-1)(35\Phi_{2\lambda}^{2}-48\Phi_{2\lambda}+15)+12\Gamma_{2\lambda}^{6}(24\Phi_{2\lambda}-15)}{H_{2\lambda}^{10}}]\}\end{aligned} \tag{22}$$

$$\begin{aligned}\widetilde{K}_{\lambda}''''(0) = {} & -90\mu_{\lambda}\times(1-\tilde{a}_{\lambda}^{2})(1+\tilde{\rho}_{\lambda})(1-14\tilde{a}_{\lambda}^{2}+21\tilde{a}_{\lambda}^{4})-6\nu_{\lambda}\times(1+\tilde{\rho}_{\lambda})[(315\tilde{a}_{\lambda}^{6}-525\tilde{a}_{\lambda}^{4}+225\tilde{a}_{\lambda}^{2}\\ & -15)\tilde{\rho}_{\lambda}^{2}+(198\tilde{a}_{\lambda}^{6}-258\tilde{a}_{\lambda}^{4}+234\tilde{a}_{\lambda}^{2}-30)\tilde{\rho}_{\lambda}-112\tilde{a}_{\lambda}^{6}-88\tilde{a}_{\lambda}^{4}-4\tilde{a}_{\lambda}^{2}+8]\end{aligned} \tag{23}$$

Eqs. (21) and (22) are the higher-order derivatives of the dimensionless stiffness. They are mainly used to analyze the nonlinear variation of stiffness and to locate the critical parameter conditions of the QZS system. In short, they help determine where the system exhibits quasi-zero stiffness behavior and define the stability boundaries. When $\widetilde{K}_{\lambda}''(0)=0$, in order to further get the Taylor series approximation of $\tilde{f}_{\lambda}$ in the QZS isolation system, it is necessary to further derive Eq. (19), which in turn yields the Taylor series expansion of the isolation system. In the quasi-zero stiffness isolation system, the variable or coefficient refers to: $\nu_{\lambda}=\{1+2\mu_{\lambda}[1-(1-\tilde{a}_{\lambda}^{2})(1+\tilde{\rho}_{\lambda})]\}/\{2\tilde{\rho}_{\lambda}^{2}[3\tilde{a}_{\lambda}^{2}-\tilde{\rho}_{\lambda}(1-\tilde{a}_{\lambda}^{2})]\}$, while satisfying $\widetilde{K}_{\lambda}(0)=0$ when $\tilde{\rho}_{\lambda}\neq 3\tilde{a}_{\lambda}^{2}/(1-\tilde{a}_{\lambda}^{2})$. Further combining Eq. (20) and Eq. (23), the $\tilde{f}_{\lambda}$ of the system at $\tilde{\lambda}=0$ can be obtained as follows Eq. (24).

$$\tilde{f} = \{-0.75\mu_\lambda \times (1-\tilde{a}_\lambda{}^2)(1+\tilde{\rho}_\lambda)(1-14\tilde{a}_\lambda{}^2+21\tilde{a}_\lambda{}^4) - 0.05\nu_\lambda \times (1+\tilde{\rho}_\lambda)[(315\tilde{a}_\lambda{}^6-525\tilde{a}_\lambda{}^4+225\tilde{a}_\lambda{}^2 - 15)\tilde{\rho}_\lambda{}^2+(198\tilde{a}_\lambda{}^6-258\tilde{a}_\lambda{}^4+234\tilde{a}_\lambda{}^2-30)\tilde{\rho}_\lambda-112\tilde{a}_\lambda{}^6-88\tilde{a}_\lambda{}^4-4\tilde{a}_\lambda{}^2+8]\}\tilde{\lambda}^5+o(\tilde{\lambda}^5) \quad (24)$$

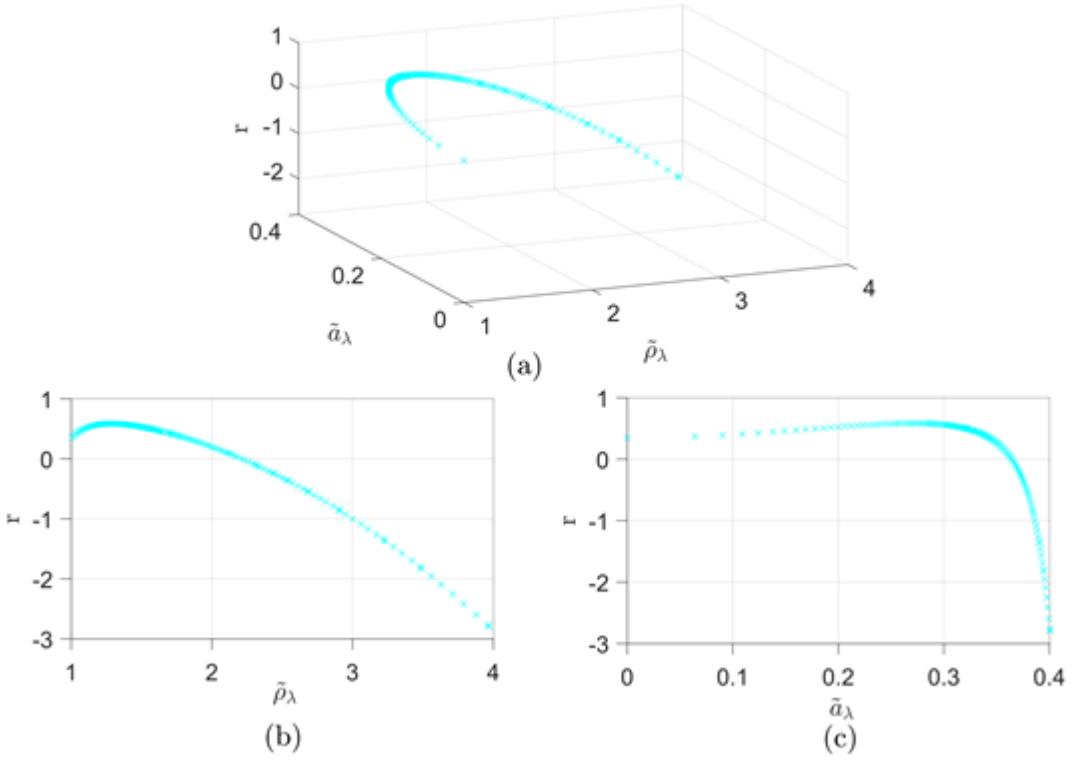

Fig. 21: Plot of nonlinear coefficients r versus parameters $\tilde{a}_\lambda$ and $\tilde{\rho}_\lambda$ when $\nu_\lambda = 0.5$; (a) 3D surface plot, (b) 2D mapping diagram r -$\tilde{\rho}_\lambda$, (c) 2D mapping diagram r -$\tilde{a}_\lambda$.

According to the corresponding relationship curves of critical parameter $\tilde{a}_\lambda$ value and $\tilde{\rho}_\lambda$ value in Fig. 18, combined with Eq. (23), we can further make the relationship between nonlinear coefficients r of the fifth-order Taylor series expansion and critical parameter $\tilde{a}_\lambda$ value and $\tilde{\rho}_\lambda$ value as shown in Fig. 19 to 22. As shown in Fig. 19 to 22, for varying values of ν_λ and the critical parameters $\tilde{a}_\lambda$ and $\tilde{\rho}_\lambda$, the nonlinear coefficient r of the vibration isolation system initially increases and then decreases. When the values of $\tilde{a}_\lambda$ and $\tilde{\rho}_\lambda$ are large, the nonlinear coefficient r becomes negative, which is undesirable in practical applications, as this indicates that the device is in an unstable state.

In practical engineering applications, the pre-compression coefficient of the spring is constrained, meaning that the critical parameter $\tilde{\rho}_\lambda$ cannot be excessively large. Therefore, during parameter selection, it is preferable to choose smaller values for $\tilde{\rho}_\lambda$ and the corresponding $\tilde{a}_\lambda$ as much as possible. Hence, by considering various softening cubic stiffness coefficients ν_λ four distinct sets of optimization parameters for the QZS isolation system can be obtained, as outlined below: $\nu_\lambda = 0.05$, $\mu_\lambda = 0.542$, $\tilde{a}_\lambda = 0.108$, $\tilde{\rho}_\lambda = 2.66$, $r = 0.1640$; $\nu_\lambda = 0.25$, $\mu_\lambda = 0.826$, $\tilde{a}_\lambda = 0.099$, $\tilde{\rho}_\lambda = 1.35$, $r = 0.3076$; $\nu_\lambda = 0.5$, $\mu_\lambda = 1.015$, $\tilde{a}_\lambda = 0.109$, $\tilde{\rho}_\lambda = 1.03$, $r = 0.4120$; $\nu_\lambda = 0.75$, $\mu_\lambda = 1.148$, $\tilde{a}_\lambda = 0.107$, $\tilde{\rho}_\lambda = 0.88$, $r = 0.4714$.

Fig. 23 presents the comparison between the exact dimensionless force-displacement expression and the fifth-order Taylor series expansion for the QZS vibration isolation system, considering the four different sets of optimization parameters. It is observed that the fifth-order Taylor series expansion provides a poor fit at the end of the system's compression stroke, with the discrepancy between the approximate and exact expressions increasing as the system's displacement grows. When $\nu_\lambda = 0.05$, the fifth-order Taylor series expansion provides the best fit. However, as the value increases, the fit gradually worsens. Notably, for dimensionless displacements of the system below 0.05, the approximation is quite accurate across different values of ν_λ.

5. Dynamic analysis of the three-dimensional device with optimized parameters

In the modeling process, it is considered that the QZS system includes damping elements characterized by damping coefficients C_λ. Specifically, $\lambda = z$ refers to the vertical vibration isolation branch with damping coefficient C_z, while $\lambda = x$ or $\lambda = y$ corresponds to the horizontal isolation branches with damping coefficients C_x and C_y, respectively. When an external excitation such as $F\cos\omega t$ acts on the isolated object or $D\cos\omega t$ is applied through the base, the dynamic behavior of the system is governed by the following

differential equations.

$$m_\lambda \lambda''(t) + C_\lambda \lambda'(t) + f_\lambda = F cos\omega t \quad (25)$$

$$m_\lambda {\lambda_d}''(t) + C_\lambda {\lambda_d}'(t) + f_\lambda = m_\lambda \omega^2 D \cos \omega t \quad (26)$$

In Eq. (25), F represents the force excitation amplitude, while D in Eq. (26) indicates the amplitude of the imposed displacement excitation λ_a. The relative displacement between the mass and the excitation is expressed as $\lambda_d = \lambda - \lambda_a$. To express the system in a dimensionless form, the following parameters are introduced: $\tilde{f}_\lambda = nf_\lambda/k_{1\lambda}l_\lambda$, $\tilde{\lambda} = \lambda/l_\lambda$, $\tilde{F} = F/k_{1\lambda}l_\lambda$, $m_\lambda{\omega_\lambda}^2 = k_{1\lambda}$, $\Omega_\lambda = \omega/\omega_\lambda$, $\xi_\lambda = C_\lambda\omega_\lambda/2k_{1\lambda}$, $\tilde{\lambda}_d = \lambda_d/l_\lambda$, $\widetilde{D} = D/k_{1\lambda}l_\lambda$. By substituting these parameters, the motion equations from Eq. (25) and Eq. (26) can be rewritten in a dimensionless form using $\tau_\lambda = \omega_\lambda t$.

$$\tilde{\lambda}''\tau_\lambda) + 2\xi_\lambda\tilde{\lambda}'(\tau_\lambda) + \tilde{F}_\lambda/n = \tilde{F}\cos(\Omega_\lambda\tau_\lambda \quad (27)$$

$$\tilde{\lambda}_d{}''(\tau_\lambda) + 2\xi_\lambda\tilde{\lambda}_d{}'(\tau_\lambda) + \tilde{f}_{\lambda_d}/n = {\Omega_\lambda}^2\widetilde{D}\cos(\Omega_\lambda\tau_\lambda) \quad (28)$$

Let $\tilde{f}_\lambda/n = r\tilde{\lambda}^5/n$, $\tilde{f}_{\lambda_d}/n = r{\tilde{\lambda}_d}^5/n$, then Eq. (27) and Eq. (28) can be further deduced as

$$\widetilde{\lambda''}(\tau_\lambda) + 2\xi_\lambda\widetilde{\lambda'}(\tau_\lambda) + \frac{r\tilde{\lambda}^5}{n} = \tilde{F}_\lambda\cos(\Omega_\lambda\tau_\lambda \quad (29)$$

$$\tilde{\lambda}_d{}''(\tau_\lambda) + 2\xi_\lambda\tilde{\lambda}_d{}'(\tau_\lambda) + r{\tilde{\lambda}_d}^5/n = {\Omega_\lambda}^2\widetilde{D}_\lambda\cos(\Omega_\lambda\tau_\lambda) \quad (30)$$

When $\lambda = z$, it indicates the vertical QZS subsystem within the three-dimensional isolator, corresponding to $n = 1/4$ in Eq. (29) and Eq. (30). Similarly, $\lambda = x$ or $\lambda = y$ refers to the horizontal QZS subsystem along the X- and Y-axes, where n takes the value 1/2 in Eq. (29) and Eq. (30). Let $\tilde{\lambda}(\tau_\lambda) = A\cos(\Omega_\lambda\tau_\lambda + \theta)$, $\tilde{\lambda}_d(\tau_\lambda) = \widetilde{D}\cos(\Omega_\lambda\tau_\lambda + \theta)$, using the harmonic balance method to simplify the equations of motion, the following equations can be obtained

$$(-{\Omega_\lambda}^2 A + \frac{5}{8n}rA^5)^2 + (-2\xi_\lambda A\Omega_\lambda)^2 = {\tilde{F}_\lambda}^2 \quad (31)$$

$$(-{\Omega_\lambda}^2\widetilde{D} + \frac{5}{8n}r\widetilde{D}^5)^2 + (-2\xi_\lambda\widetilde{D}\Omega_\lambda)^2 = {\Omega_\lambda}^4{\widetilde{D}_\lambda}^2 \quad (32)$$

From Eq. (29), the dimensionless force experienced by the isolated object due to the QZS vibration isolation system is given by: $\tilde{f}_t = 2\xi_\lambda\tilde{\lambda}'(\tau_\lambda) + r\tilde{\lambda}^5(\tau_\lambda)/n$, assuming $\tilde{f}_t = \tilde{F}_t\cos(\Omega_\lambda\tau_\lambda + \theta)$, $\tilde{\lambda}(\tau_\lambda) = A\cos(\Omega_\lambda\tau_\lambda + \theta)$, and expanding $r\tilde{\lambda}^5(\tau_\lambda)/n$ into Fourier series, we obtain: ${\tilde{F}_t}^2 = (\frac{5}{8n}rA^5)^2 + (2\xi_\lambda A\Omega_\lambda)^2$. Defining the force transmissibility as the ratio of the response amplitude $\tilde{F}_t$ to the excitation amplitude $\tilde{F}_\lambda$, and combining it with Eq. (31), the subsequent conclusions can be drawn.

$$T_F = \frac{\tilde{F}_t}{\tilde{F}_\lambda} = \frac{|A|\sqrt{(\frac{5}{8n}rA^4)^2 + (2\xi_\lambda\Omega_\lambda)^2}}{\tilde{F}_\lambda} \quad (33)$$

The T_Z is defined as the ratio of the displacement response amplitude $\widetilde{D}$ to the displacement excitation amplitude $\widetilde{D}_\lambda$. Combined with Eq. (32), the equation can be further derived as follows

$$(-{\Omega_\lambda}^2 T_Z + \frac{5}{8n}r\widetilde{D}_\lambda{}^4 T_Z{}^5)^2 + (-2\xi_\lambda T_Z\Omega_\lambda)^2 = {\Omega_\lambda}^4 \quad (34)$$

In order to better study the vibration isolation performance of the QZS isolator, a comparative analysis between the optimized system and the traditional three-spring QZS isolation system can be conducted. A conventional three-spring QZS isolation system consisting of a pair of inclined springs and a vertical spring.[6] The optimal configuration parameters of the traditional three-spring QZS isolation system for $\nu_\lambda = 0$ and $\nu_\lambda \neq 0$ can be obtained from the published paper,[4-5] as summarized in Table 1. It is worth noting that five sets of optimization parameters for the three-dimensional QZS isolation system are also listed in Table 1, where Case I is the case where the softened cubic stiffness coefficient ν_λ is not taken into account ($\nu_\lambda = 0$); Case II, Case III, Case IV, and Case V are four sets of optimized parameter values considering the softening cubic stiffness coefficient ($\nu_\lambda \neq 0$).

5.1 Dynamic analysis of vertical QZS system with optimized parameters

Based on the above formulas, the force transmissibility comparison curves of the Z-direction QZS system, the traditional three-spring QZS system, and equivalent linear

Table 1: Optimization parameters of three-dimensional and conventional three-spring QZS isolation system.

Conventional QZS system ($\nu_\lambda = 0$)	$\tilde{a} = (2/3)^{1/2}$, $\mu_\lambda = 0.5973$, $\tilde{\rho}_\lambda$=0.5, $r = 1.6459$
Conventional QZS system ($\nu_\lambda \neq 0$)	$\tilde{a} = 0.5$, ν_λ=0.1709, $\mu_\lambda = 0.51$, $\tilde{\rho}_\lambda$=0.89
Three-dimensional QZS system (Case I)	$\mu_\lambda = 1$, $\tilde{a}_\lambda = 0.447$, $\tilde{\rho}_\lambda = 0.876$, r=1.0805
Three-dimensional QZS system (Case II)	$\nu_\lambda = 0.05$, $\mu_\lambda = 0.542$, $\tilde{a}_\lambda = 0.108$, $\tilde{\rho}_\lambda = 2.66$
Three-dimensional QZS system (Case III)	$\nu_\lambda = 0.25$, $\mu_\lambda = 0.826$, $\tilde{a}_\lambda = 0.099$, $\tilde{\rho}_\lambda = 1.35$
Three-dimensional QZS system (Case IV))	$\nu_\lambda = 0.5$, $\mu_\lambda = 1.015$, $\tilde{a}_\lambda = 0.109$, $\tilde{\rho}_\lambda = 1.03$
Three-dimensional QZS system (Case V))	$\nu_\lambda = 0.75$, $\mu_\lambda = 1.148$, $\tilde{a}_\lambda = 0.107$, $\tilde{\rho}_\lambda = 0.88$

system under optimized parameters in Table 1 can be plotted, as shown in Fig. 24. From Fig. 24(a) and Fig. 24(b), it can be seen that for the excitation amplitude $\tilde{F}_z = 0.01$ and damping ratio $\xi_z = 0.05$, vibration isolation occurs in the equivalent linear system at a frequency ratio of $\Omega_z > \sqrt{2} \approx 1.414$, and the conventional three-spring QZS system has vibration isolation at $\Omega_z > 0.295$, implying that the isolation starting frequency of the conventional three-spring QZS system is approximately $\frac{1}{5}$ of that of the equivalent linear system. The Z-direction QZS systems under five sets of optimization

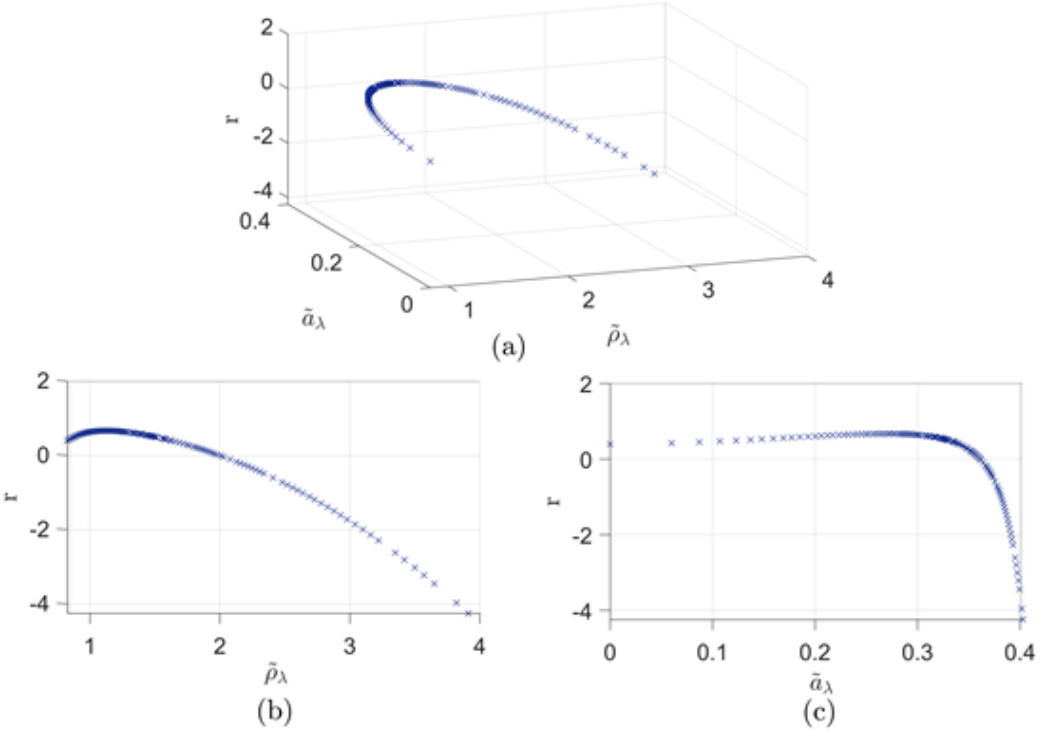

Fig. 22: Plot of nonlinear coefficients r versus parameters $\tilde{a}_\lambda$ and $\tilde{\rho}_\lambda$ when $\nu_\lambda = 0.75$; (a) 3D surface plot, (b) 2D mapping diagram r -$\tilde{\rho}_\lambda$, (c) 2D mapping diagram r -$\tilde{a}_\lambda$.

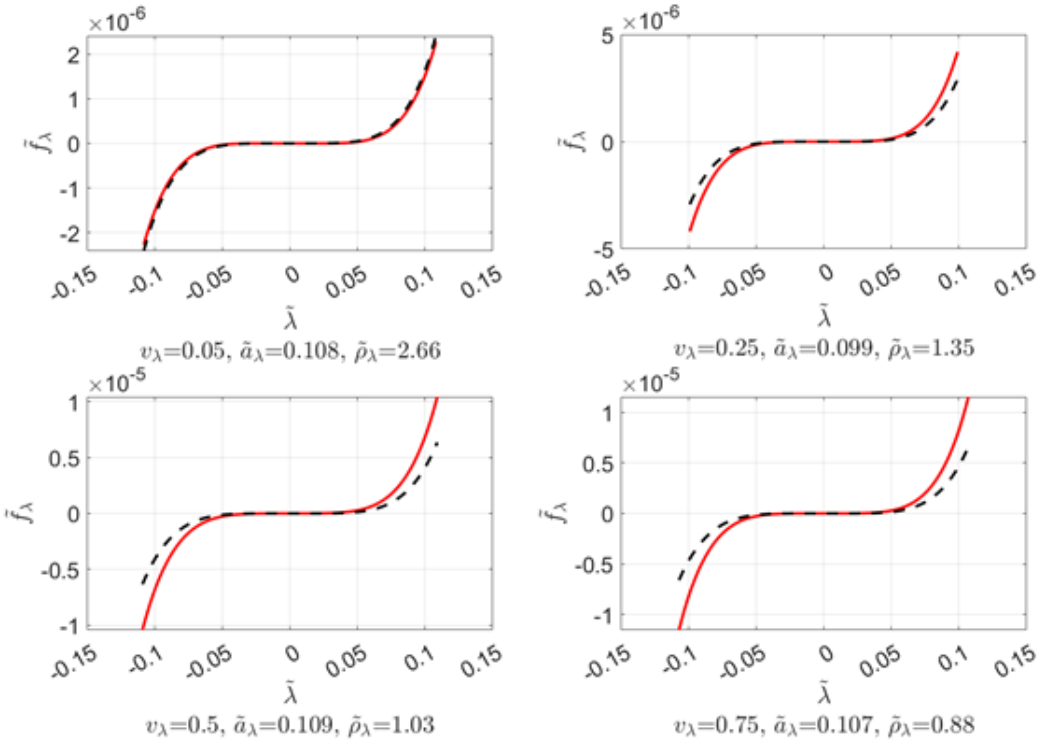

Fig. 23: Dimensionless force–displacement comparison plots and Taylor series approximations for the QZS isolator under four sets of optimized parameter configurations.

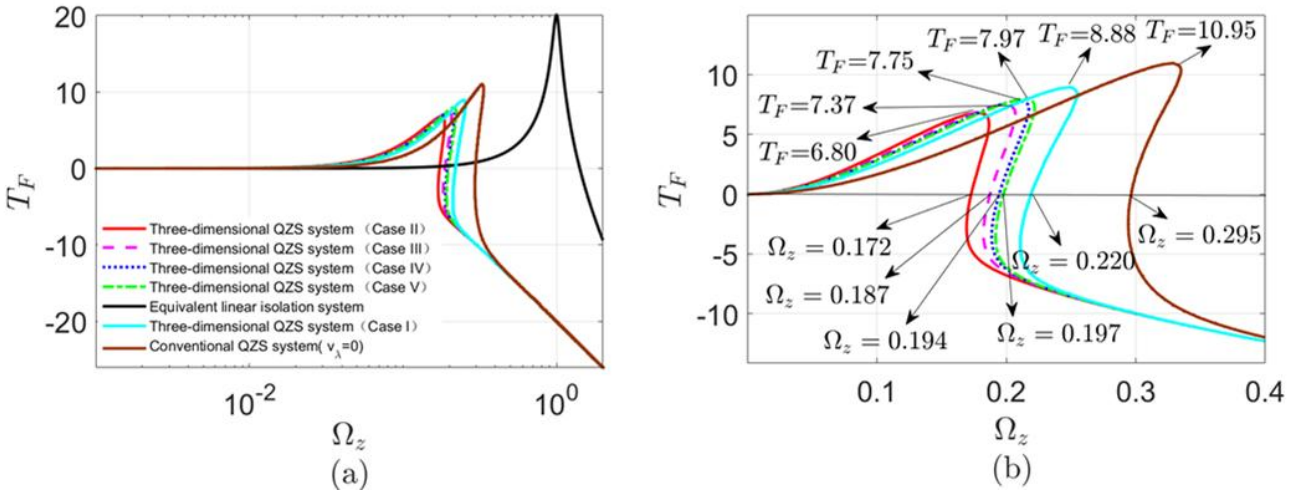

Fig. 24: The comparison of force transmissibility between the Z-direction QZS system under optimized parameters, the traditional three-spring QZS system, and the equivalent linear system; (a) analysis of the three systems under the same force excitation amplitude ($\tilde{F}_z = 0.01$), (b) detailed enlarged view.

parameters (Case I, Case II, Case III, Case IV, and Case V) exhibit vibration isolation effects when $\Omega_z > 0.220$, $\Omega_z > 0.172$, $\Omega_z > 0.187$, $\Omega_z > 0.194$, and $\Omega_z > 0.197$, respectively. This means that under the optimized parameters, the isolation starting frequencies of the Z-direction QZS systems (Case I, Case II, Case III, Case IV, and Case V) are approximately $\frac{7}{12}$ to $\frac{3}{4}$ of the isolation starting frequency of the traditional three-spring QZS system and $\frac{3}{19}$ to $\frac{1}{8}$ of the isolation starting frequency of the equivalent linear system.

It can be further seen from Fig. 24 that the equivalent linear system has a force transmissibility amplitude of 20 at the resonance frequency, and the conventional three-spring QZS system has a force transmissibility amplitude of 10.95 at the resonance frequency, implying that the maximum response amplitude of the conventional three-spring QZS system is approximately $\frac{1}{2}$ of the maximum response amplitude of the equivalent linear system. The force transmissibility amplitudes at the resonance frequency for the Z-direction QZS systems are as follows: Case I: 8.88, Case II: 6.80, Case III: 7.37, Case IV: 7.75, and Case V: 7.97. This means that the maximum response amplitude of the Z-direction QZS systems under the five sets of optimized parameters (Case I, Case II, Case III, Case IV, and Case V) is approximately $\frac{3}{5}$ to $\frac{4}{5}$ of the maximum response amplitude, and approximately $\frac{7}{20}$ to $\frac{3}{7}$ of the maximum response amplitude of the equivalent linear system. It is worth noting that the isolation starting frequency and the maximum response amplitude of the Z-direction QZS systems with optimized parameters, considering the nonlinear coefficient of the inclined spring (Case II, Case III, Case IV, and Case V), is lower than that of the system without considering the nonlinear coefficient (Case I).

From Fig. 25(a) and Fig. 25(b), it can be seen that the optimized QZS system exhibits a broader isolation frequency range and reduced vibration amplitudes compared to both the equivalent linear system and the conventional QZS system, enabling it to effectively isolate vibrations at lower

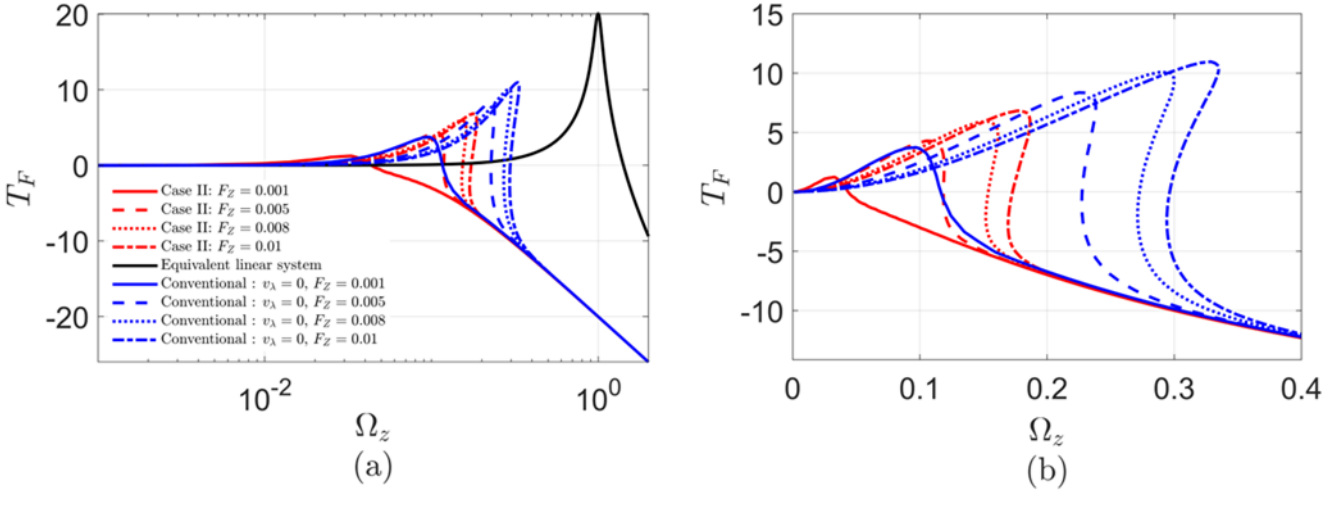

Fig. 25: Comparison of Z-direction QZS system (Case II), Conventional system ($v_\lambda = 0$) and Equivalent linear system at different excitation amplitudes； (a) analysis of the three systems under the different force excitation amplitude, (b) detailed enlarged view.

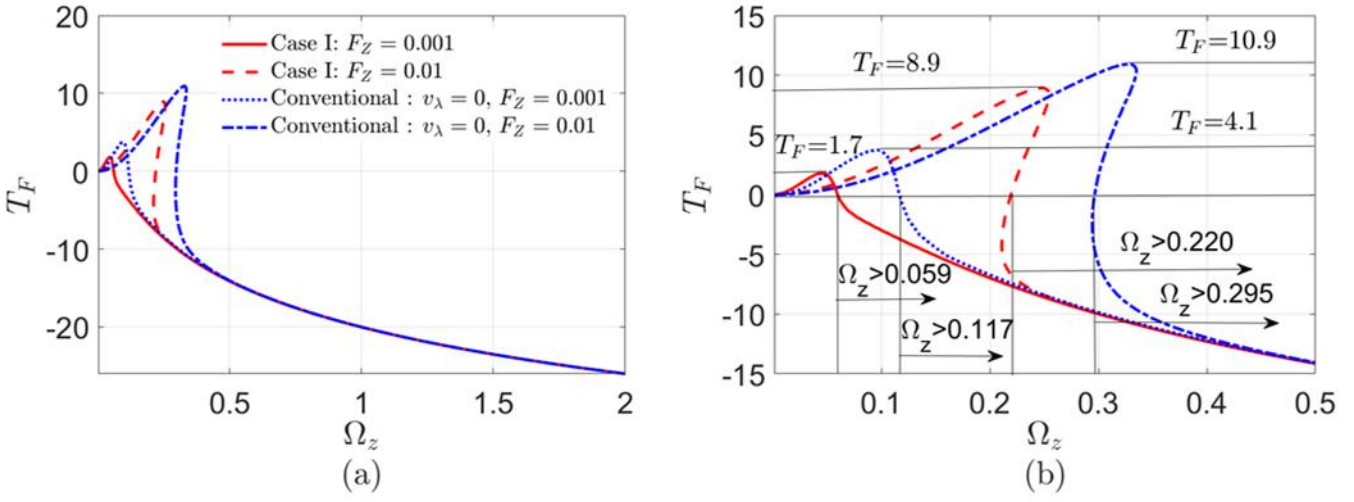

Fig. 26: Comparison of Z-direction QZS system and conventional system without considering the nonlinear coefficient of tilting springs ($v_\lambda = 0$, $\xi_z = 0.05$); (a) analysis of the two systems under the different force excitation amplitude, (b) detailed enlarged view.

frequencies. Additionally, for the Z-direction QZS system, as the excitation amplitude $\tilde{F}_z$ decreases, both the peak force transmissibility and the corresponding resonance frequency reduce, resulting in improved vibration isolation performance compared to the conventional QZS system.

When $v_\lambda = 0$ and $\xi_z = 0.05$, the comparison curves of force transmissibility between the Z-direction QZS system and the conventional system with optimized parameters are shown in Fig. 26. From Fig. 26(a) and Fig. 26(b), it can be observed that under the conditions of excitation amplitude $\tilde{F}_z = 0.01$ and damping ratio $\xi_z = 0.05$, the conventional system shows vibration isolation when $\Omega_z > 0.295$, indicating that the vibration isolation starting frequency of the conventional system is approximately $\frac{1}{5}$ that of the equivalent linear system.

The optimized system shows vibration isolation when $\Omega_z > 0.220$, which means that the vibration isolation starting frequency of optimized Z-direction system is approximately $\frac{3}{4}$ that of the conventional system and $\frac{3}{20}$ that of the equivalent linear system. Under the conditions of excitation amplitude $\tilde{F}_z = 0.001$ and damping ratio $\xi_z = 0.05$, the conventional QZS system shows vibration isolation when $\Omega_z > 0.117$, indicating that the vibration isolation starting frequency of the conventional QZS system is approximately $\frac{1}{12}$ that of the equivalent linear system. The optimized Z-direction system shows vibration isolation when $\Omega_z > 0.059$, which means that the vibration isolation starting frequency of optimized Z-direction system is approximately $\frac{1}{2}$ that of the conventional QZS system and $\frac{1}{24}$ that of the equivalent linear system.

From Fig. 26, it can be further observed that under the conditions of excitation amplitude $\tilde{F}_z = 0.01$ and damping ratio $\xi_z = 0.05$, the amplitude of the equivalent linear system at resonance frequency reaches 20. The force transmissibility amplitude of the conventional QZS system at resonance frequency is 10.9, indicating that the maximum response amplitude of the conventional QZS system is approximately $\frac{1}{2}$ of the maximum response amplitude of the equivalent linear system. The force transmissibility amplitude of the optimized Z-direction QZS system at resonance frequency is 8.9, meaning that the maximum response amplitude of optimized Z-direction QZS system is approximately $\frac{5}{6}$ of the maximum response amplitude of the conventional QZS system, and approximately $\frac{5}{12}$ of the maximum response amplitude of the equivalent linear system. Under the conditions of excitation amplitude $\tilde{F}_z = 0.001$ and damping ratio $\xi_z = 0.05$, the force transmissibility amplitude of the conventional QZS system at resonance frequency is 4.1, indicating that the maximum response amplitude of the conventional QZS system is approximately $\frac{1}{5}$ of the maximum response amplitude of the equivalent linear system. The amplitude of the optimized Z-direction QZS system at resonance frequency is 1.7, meaning that the maximum response amplitude of the optimized Z-direction QZS system is approximately $\frac{2}{5}$ of the maximum response amplitude of the conventional QZS system, and approximately $\frac{2}{25}$ of the maximum response amplitude of the equivalent linear system. It is worth noting that the vibration isolation starting frequency of the optimized Z-direction QZS system decreases as $\tilde{F}_z$ decreases. At the same time, the peak response amplitude at resonance frequency also decreases as the force excitation amplitude $\tilde{F}_z$ decreases.

Based on the comparative analysis of the force transmissibility of various vibration isolation systems shown in Fig. 24, Fig. 25 and Fig. 26, the results demonstrate that the Z-direction QZS isolation system with optimized parameters offers superior low-frequency vibration isolation performance compared to both the equivalent linear and conventional QZS systems. It features a lower isolation onset frequency, a wider

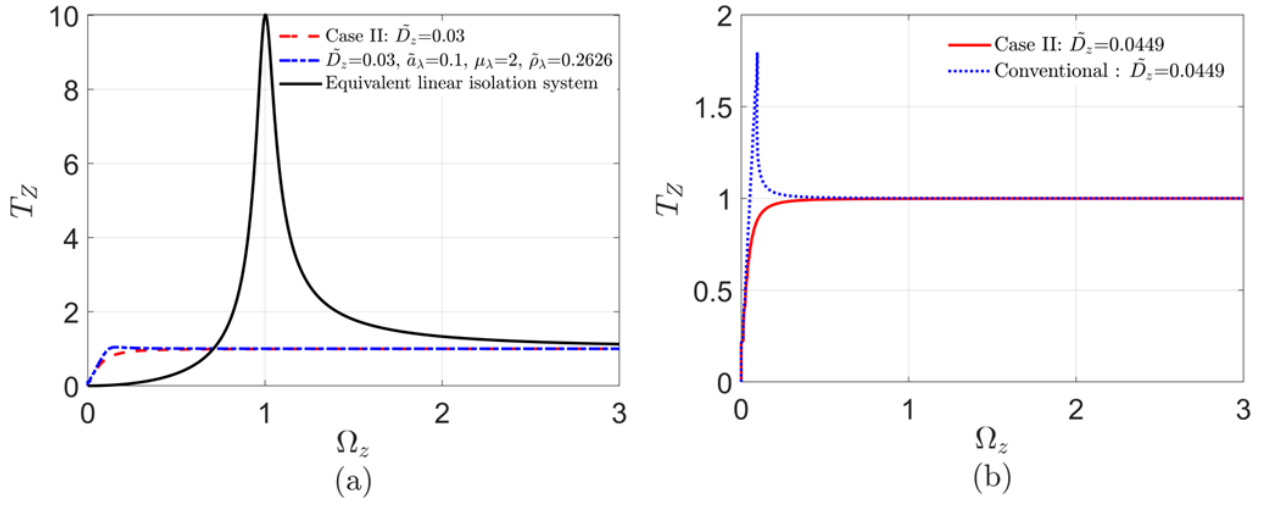

Fig. 27: Relative displacement transmissibility of different QZS systems; (a) optimized vs. non-optimized Z-direction QZS, (b) optimized Z-direction QZS vs. conventional QZS.

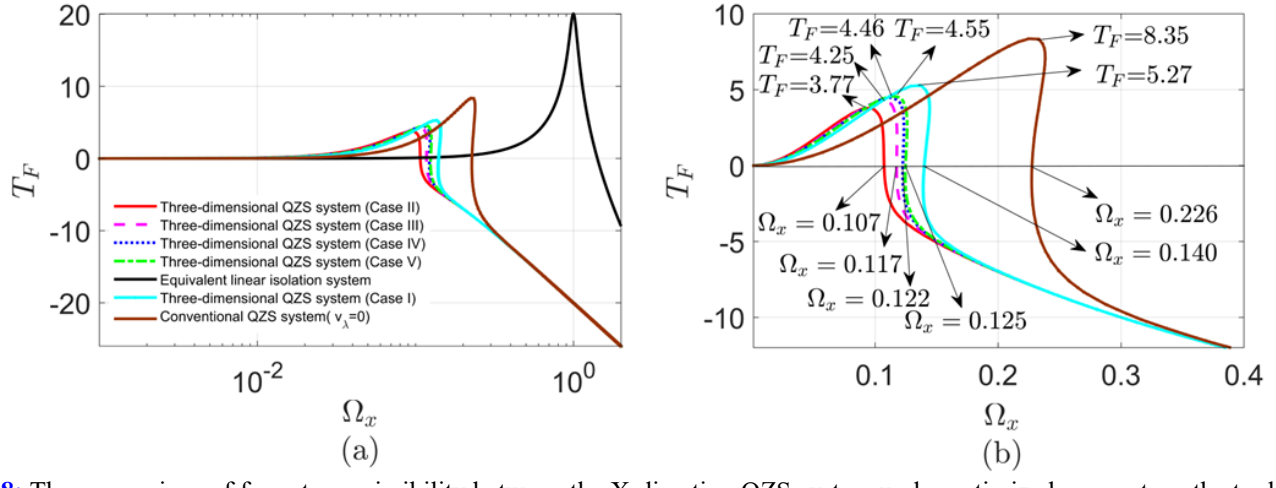

Fig. 28: The comparison of force transmissibility between the X-direction QZS system under optimized parameters, the traditional three-spring QZS system, and the equivalent linear system; (a) analysis of three systems under the same force excitation amplitude ($\tilde{F}_z = 0.005$), (b) detailed enlarged view.

frequency bandwidth for isolation, and a reduced maximum response amplitude at the resonance frequency. Furthermore, as the force excitation amplitude decreases, the enhancement in vibration isolation performance becomes increasingly pronounced. Notably, the rate at which the maximum response amplitude of the Z-direction QZS system decreases with reduced force excitation amplitude is significantly higher than that of the equivalent linear system under identical conditions. This indicates that as the force excitation amplitude $\tilde{F}_z$ decreases, the vibration isolation performance of the Z-direction QZS system with optimized parameters improves considerably.

The comparison of relative displacement transmissibility for the Z-direction QZS system with optimized parameters, the equivalent linear system, and the conventional QZS system is presented in Fig. 27, based on Eq. (32) and (34). Fig. 27(a) compares relative displacement transmissibility of the optimized and non-optimized Z-direction QZS systems and the equivalent linear system, considering softening cubic stiffness ($\nu_\lambda \neq 0$). Fig. 27(b) presents a comparison of the absolute displacement transmissibility between the Z-direction QZS system and the conventional QZS system under identical damping and excitation conditions, excluding the influence of the softening cubic stiffness coefficient ($\nu_\lambda = 0$).

From Fig. 27(a) and Fig. 27(b), it can be observed that when the damping coefficient ($\xi_z = 0.05$), the peak relative transmissibility under harmonic excitation vanishes. This further indicates that the Z-direction QZS system with optimized parameters provides superior low-frequency vibration isolation performance when compared to both the conventional QZS system and the equivalent linear system, which do not account for the nonlinear coefficients.

5.2 Dynamic analysis of horizontal QZS system with optimized parameters

Considering that the construction of the X-direction QZS

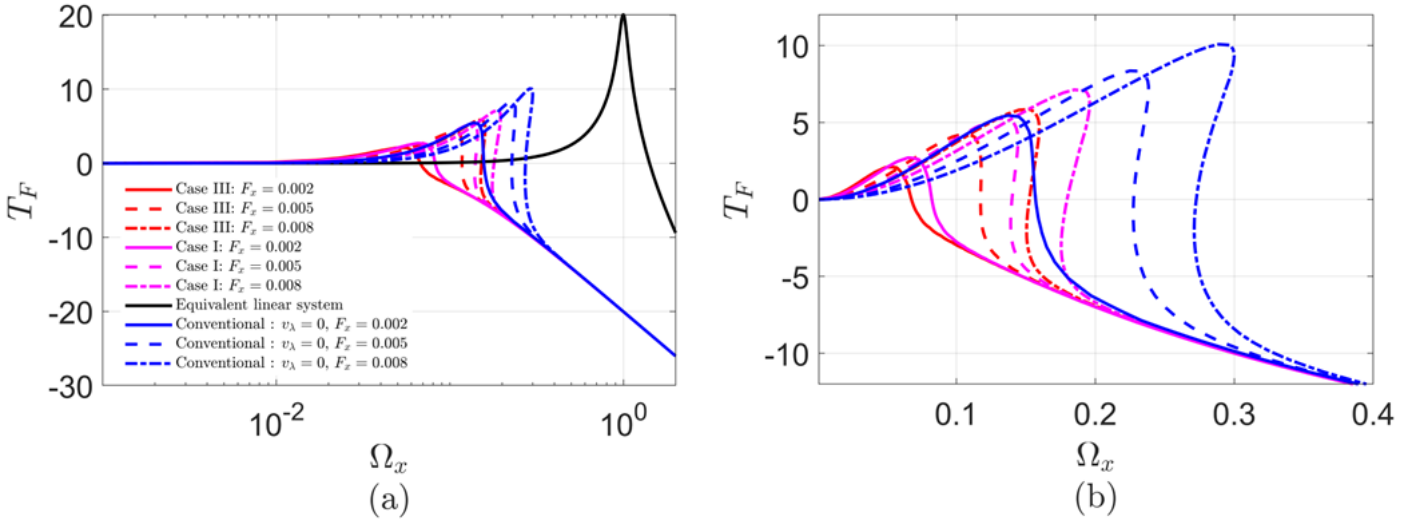

Fig. 29: Comparison of X-direction QZS system (Case III), Conventional system ($v_\lambda = 0$) and Equivalent linear system at different excitation amplitudes; (a) analysis of three systems under the different force excitation amplitude, (b) detailed enlarged view.

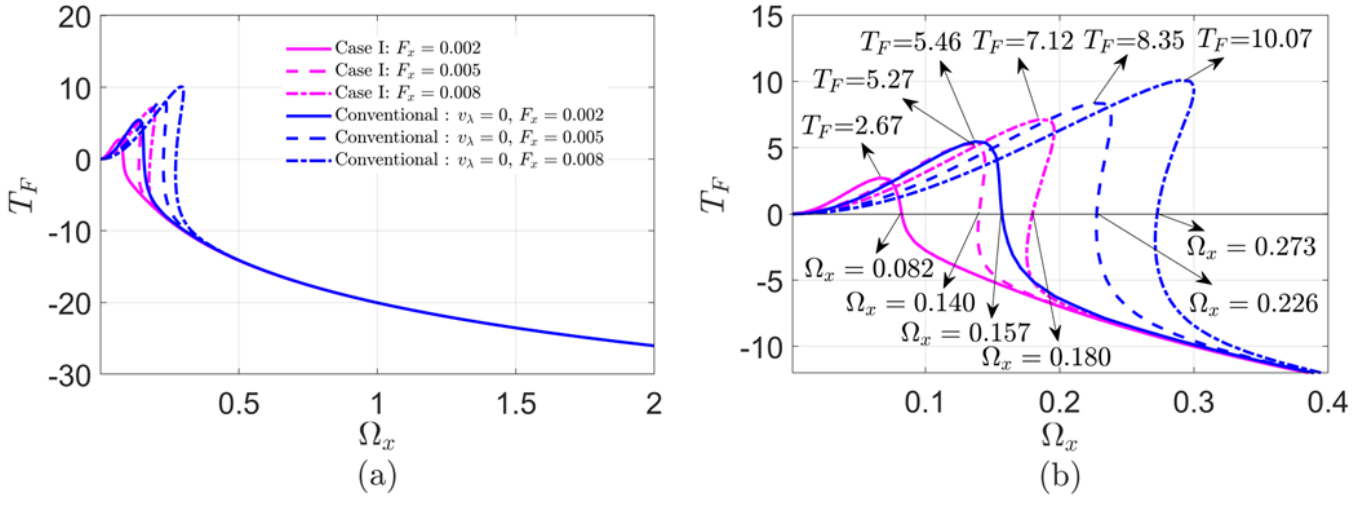

Fig. 30: Comparison of X-direction and conventional QZS system without considering nonlinear coefficient of tilting springs ($v_\lambda = 0$, $\xi_x = 0.05$); (a) analysis of the two systems under the different force excitation amplitude, (b) detailed enlarged view.

system and the Y-direction QZS system is essentially the same, we will focus on the dynamic analysis of the X-direction QZS system under optimized parameters. The Y-direction QZS system can be referenced similarly. Based on the above formulas, the force transmissibility comparison curves of the X-direction QZS system, the traditional and the equivalent linear system under the optimized parameters in Table 1 can be plotted, as shown in Fig. 28. From Fig. 28(a) and Fig. 28(b), it can be seen that for the excitation amplitude $\tilde{F}_z = 0.005$ and damping ratio $\xi_x = 0.05$, and the conventional QZS system has vibration isolation at $\Omega_z > 0.226$, implying that the isolation starting frequency of the conventional QZS system is approximately $\frac{1}{6}$ of that of the equivalent linear system. The X-direction QZS systems under five sets of optimization parameters (Case I, Case II, Case III, Case IV, and Case V) exhibit vibration isolation effects when $\Omega_z > 0.140$, $\Omega_z > 0.107$, $\Omega_z > 0.117$, $\Omega_z > 0.122$, and $\Omega_z > 0.125$, respectively. This means that under the optimized parameters, the isolation starting frequencies of the X-direction QZS systems (Case I, Case II, Case III, Case IV, and Case V) are approximately $\frac{5}{11}$ to $\frac{5}{8}$ of the isolation starting frequency of the conventional QZS system and $\frac{1}{13}$ to $\frac{1}{10}$ of the isolation starting frequency of the equivalent linear system.

It can be further seen from Fig. 28 that the equivalent linear system has a force transmissibility amplitude of 20 at the resonance frequency, and the conventional QZS system has a force transmissibility amplitude of 8.35 at the resonance frequency, implying that the maximum response amplitude of the conventional QZS system is approximately $\frac{5}{12}$ of the maximum response amplitude of the equivalent linear system. The force transmissibility amplitudes at the resonance frequency for the X-direction QZS systems are as follows: Case I: 5.27, Case II: 3.77, Case III: 4.25, Case IV: 4.46, and

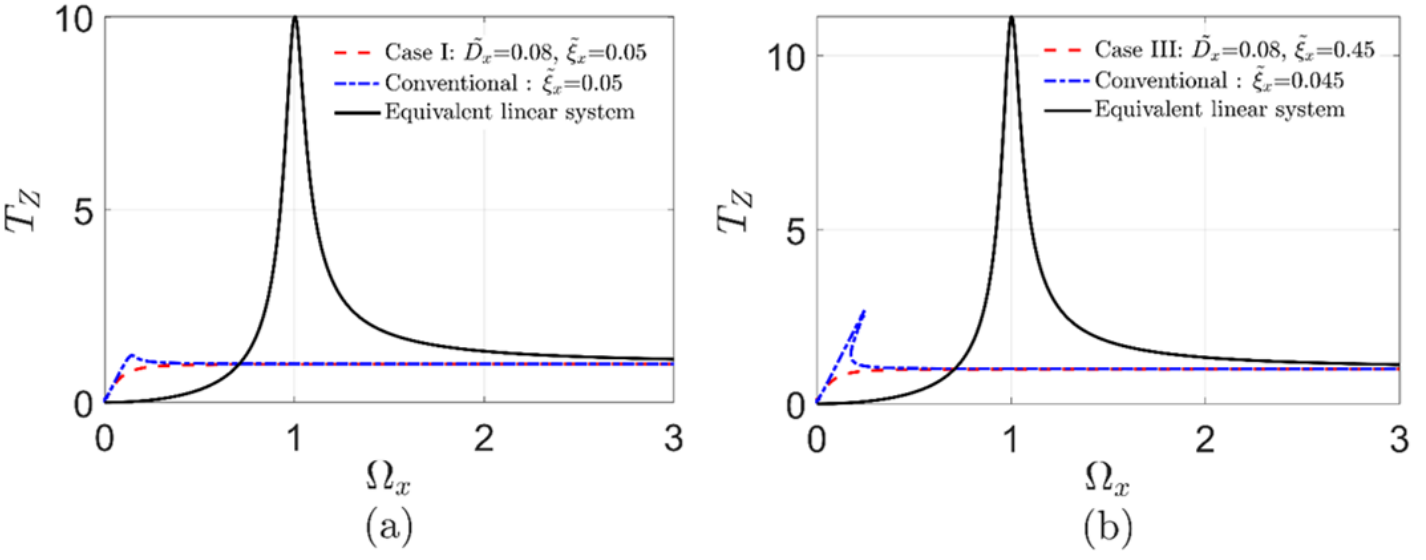

Fig. 31: Relative displacement transmissibility comparison of different QZS systems; (a) Case I with optimized parameters vs. conventional system ($\xi_x = 0.05$), (b) Case III with optimized parameters vs. conventional system ($\xi_x = 0.045$).

Case V: 4.55. This means that the maximum response amplitude of the X-direction QZS systems under the five sets of optimized parameters (Case I, Case II, Case III, Case IV, and Case V) is approximately $\frac{9}{20}$ to $\frac{5}{8}$ of the maximum response amplitude of the conventional QZS system, and approximately $\frac{3}{16}$ to $\frac{1}{4}$ of the maximum response amplitude of the equivalent linear system. Note that the isolation starting frequency and the maximum response amplitude of the X-direction QZS systems with optimized parameters, considering the nonlinear coefficient of the inclined spring (Case II, Case III, Case IV, and Case V), is lower than that of the system without considering the nonlinear coefficient (Case I).

From Fig. 29(a) and Fig. 29(b), it is evident that the optimized QZS system offers a broader frequency isolation range and reduced vibration amplitudes compared to both the equivalent linear and conventional QZS systems, effectively isolating vibrations at lower frequencies. Furthermore, for the X-direction QZS system, as the excitation amplitude $\tilde{F}_x$ decreases, both the peak force transmissibility and the corresponding resonance frequency diminish, resulting in improved vibration isolation performance when compared to the conventional QZS system.

From Fig. 30, it can be further observed that under the conditions of excitation amplitude $\tilde{F}_x = 0.002$ and damping ratio $\xi_x = 0.05$, the force transmissibility amplitude of the equivalent linear system at resonance frequency reaches 20. The amplitude of the conventional QZS system at resonance frequency is 5.46, indicating that the maximum response amplitude of the conventional QZS system is approximately $\frac{3}{11}$ of the maximum response amplitude of the equivalent linear system. The amplitude of the optimized X-direction QZS system at resonance frequency is 2.67, meaning that the maximum response amplitude of the optimized X-direction QZS system is approximately $\frac{1}{2}$ of the maximum response amplitude of the conventional QZS system, and approximately $\frac{1}{8}$ of the maximum response amplitude of the equivalent linear system. Under the conditions of excitation amplitude $\tilde{F}_z = 0.005$ and damping ratio $\xi_x = 0.05$, the force transmissibility amplitude of the conventional QZS system at resonance frequency is 8.35, indicating that the maximum response amplitude of the conventional QZS system is approximately $\frac{5}{12}$ of the maximum response amplitude of the equivalent linear system.

The amplitude of the optimized X-direction QZS system at resonance frequency is 5.27, meaning that the maximum response amplitude of the optimized X-direction QZS system is approximately $\frac{5}{8}$ of the maximum response amplitude of the conventional QZS system, and approximately $\frac{1}{4}$ of the maximum response amplitude of the equivalent linear system. Under the conditions of excitation amplitude $\tilde{F}_z = 0.008$ and damping ratio $\xi_x = 0.05$, the force transmissibility amplitude of the conventional QZS system at resonance frequency is 10.07, indicating that the maximum response amplitude of the conventional QZS system is approximately $\frac{1}{2}$ of the maximum response amplitude of the equivalent linear system. The amplitude of the optimized X-direction QZS system at resonance frequency is 7.12, meaning that the maximum response amplitude of the optimized X-direction QZS system is approximately $\frac{7}{10}$ of the maximum response amplitude of the conventional QZS system, and approximately $\frac{7}{20}$ of the maximum response amplitude of the equivalent linear system. It is worth noting that the vibration isolation starting frequency of the optimized X-direction QZS system decreases as $\tilde{F}_x$ decreases. At the same time, the peak response amplitude at resonance frequency also decreases as the force excitation

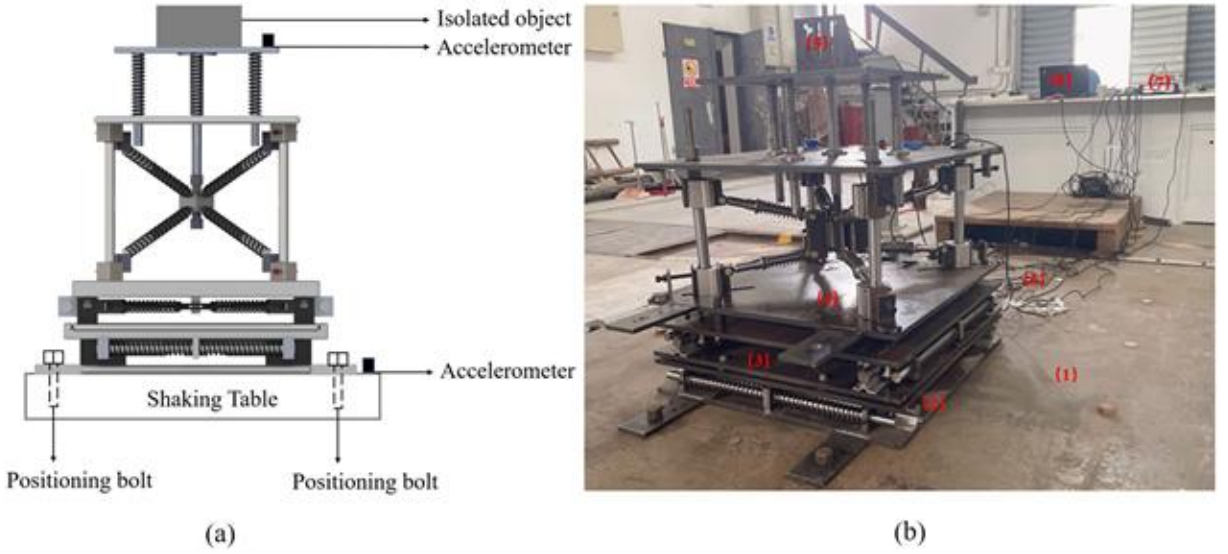

Fig. 32: Dynamic test setup for 3D QZS system: (a) structure diagram; (b) shaking table layout: (1) dual-axis table, (2) X-direction unit, (3) Y-direction unit, (4) Z-direction unit, (5) isolation mass, (6) sensors, (7) signal system, (8) computer.

amplitude $\tilde{F}_x$ decreases.

From the comparative analysis of force transmissibility across various vibration isolation systems presented in Figs. 28, 29, and 30, the results show that the X-direction QZS isolation system with optimized parameters demonstrates superior low-frequency vibration isolation performance when compared to both the equivalent linear and conventional QZS systems. Furthermore, as the force excitation amplitude decreases, the enhancement in vibration isolation performance becomes more pronounced. Notably, the rate at which the maximum response amplitude of the X-direction QZS system decreases with reduced force excitation amplitude is significantly higher than that of the equivalent linear system under the same conditions. This indicates that as the force excitation amplitude $\tilde{F}_x$ decreases, the vibration isolation performance of the optimized X-direction QZS system improves substantially.

Fig. 31 presents the comparison of relative displacement transmissibility for the X-direction QZS system with optimized parameters, the equivalent linear system, and the conventional QZS system, based on Eq. (32) and (34). In Fig. 31(a), the comparison is made between the X-direction QZS system with optimized parameters (Case I) and the conventional QZS system, considering the softening cubic stiffness coefficient. Fig. 31(b) compares the relative displacement transmissibility between the X-direction QZS system with optimized parameters (Case III) and the conventional QZS system ($\xi_x = 0.045$), without considering the softening cubic stiffness coefficient. From Fig. 31(a) and Fig. 31(b), it is evident that the peak value of relative transmissibility for the X-direction QZS system under harmonic excitation conditions is absent. This indicates that the X-direction QZS system with optimized parameters demonstrates superior low-frequency vibration isolation performance compared to both the conventional QZS system and the equivalent linear system.

6. Dynamics Experiment of the Three-Dimensional QZS device

The experiments were divided into three categories: vertical, horizontal, and combined three-dimensional configurations. Each test employed a single-degree-of-freedom excitation strategy to independently evaluate the dynamic characteristics of the respective components. The vibration platform was composed of three main subsystems as shown in Fig. 32: (1) an excitation system, (2) the QZS isolation system under study, and (3) a signal acquisition and processing system. The excitation system included a signal controller, a power amplifier, and a four-degree-of-freedom (4-DOF) bidirectional hydraulic shaking table. Harmonic excitation signals of discrete frequencies (3 Hz to 25 Hz for vertical, and 3 Hz to 15 Hz for horizontal direction) were generated and amplified before being transmitted to the vibration table.

The QZS isolation device, including its vertical and horizontal modules, was rigidly mounted to the shaking table using steel base plates and bolted connections to prevent unwanted motion. The isolated mass block was affixed to the top bearing plate of the isolator. Accelerometers (Endevco-7264A, sensitivity 0.8 mV/g, bandwidth 0-3000 Hz) were installed at multiple locations: the base platform, the top surface of the isolator, and the isolated object. These sensors captured both the input excitation and the system's dynamic response. The signal acquisition system utilized the INV-3602A acquisition unit, interfaced with the Coinv DASP V10 software for real-time data logging and analysis. The time-domain signals from the accelerometers were sampled at 1024 Hz and processed to extract displacement information.

In the vertical experiment, the system adopted a stiffness value of 11213 N/m with a 7.5 kg load, resulting in a natural frequency close to 6.15 Hz. The maximum measured

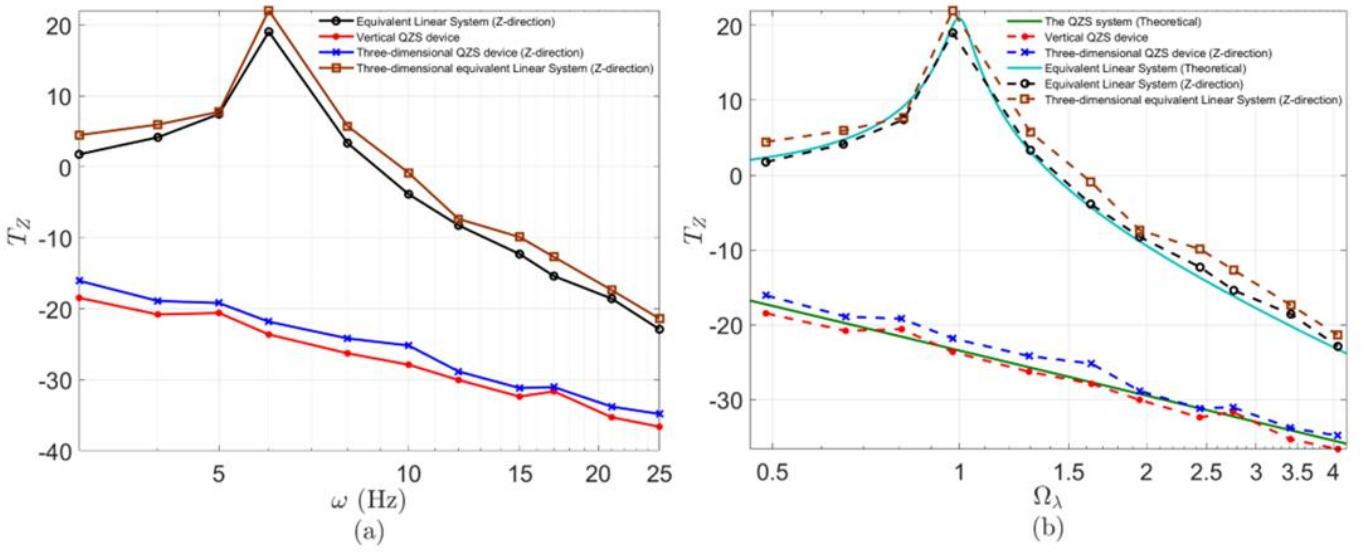

Fig. 33: Z-direction displacement transmissibility; (a) experimental results, (b) experimental vs. theoretical comparison.

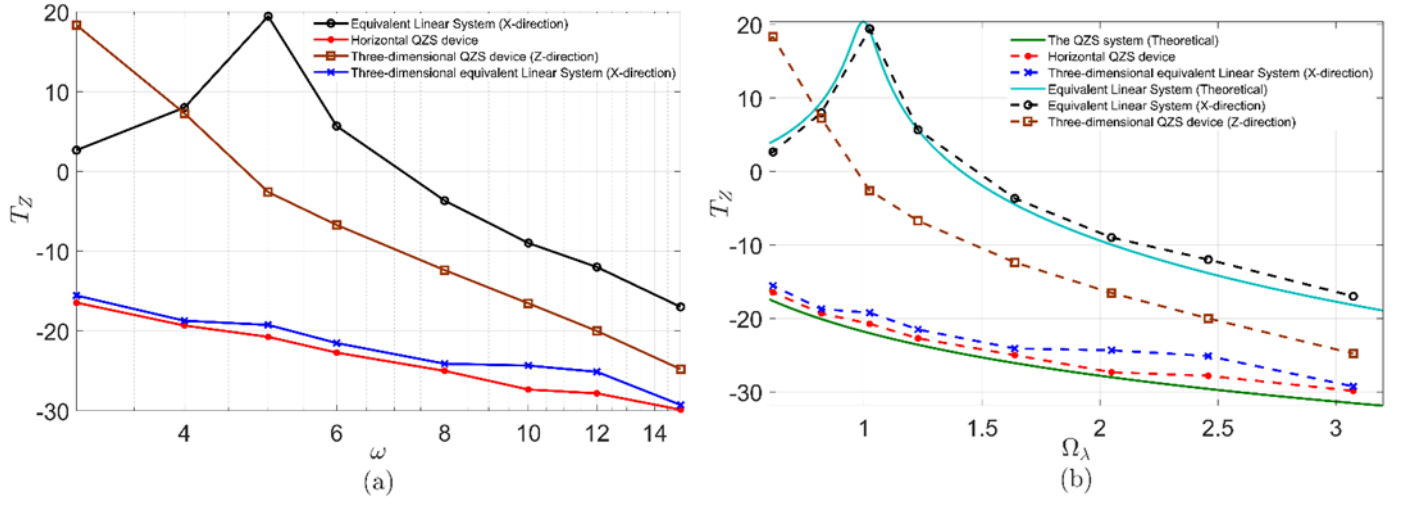

Fig. 34: X-direction displacement transmissibility; (a) experimental results, (b) comparison with theoretical values.

displacement transmissibility was 18.62 dB, corresponding to a damping ratio of 0.045. For the QZS isolator, the theoretical transmissibility curve was derived from the fitted restoring force equation: $\tilde{f}_z = 1.972\tilde{z}^3$. The dimensionless displacement amplitude was set as $\widetilde{D}_z = 0.001$. Both experimental and theoretical results showed high consistency as shown in Fig. 33, confirming the improved low-frequency performance of the QZS system, which exhibited no peak transmissibility and a broader isolation range. For the horizontal (X-direction) test as shown in Fig. 34, a similar methodology was applied. The system's equivalent linear stiffness was set to 18784 N/m with a load of 20 kg, producing a resonant frequency of 4.88 Hz. The damping ratio was calculated as 0.048 based on a peak transmissibility of 19.43 dB. The QZS isolation system in the horizontal direction demonstrated superior vibration attenuation with no resonance peak, as validated by experimental data and theoretical predictions based on the fitted restoring force: $\tilde{f}_x = 1.87\tilde{x}^3$. The dimensionless excitation amplitude was $\widetilde{D}_x = 0.00244$.

Separate excitation signals were applied in the Z- and X-directions while monitoring coupling effects. Although minor deviations were observed between the single-axis and full-system transmissibility curves, the overall performance remained consistent with theoretical expectations. This suggests that, in practice, the vertical and horizontal components can be analyzed independently due to minimal dynamic coupling. Additionally, it was noted that the resonance peak of the X-direction equivalent linear system in the full assembly appeared at a slightly lower frequency as shown in Fig. 34. This shift was attributed to the added mass of the vertical isolator module, which affected the total system inertia. Nonetheless, the QZS device maintained its superior isolation performance, making it a promising solution for multi-directional low-frequency vibration attenuation in engineering applications.

In the present study, damping is modeled as linear viscous damping for simplification. It is recognized that in practical systems, nonlinear damping mechanisms such as Coulomb

friction, material hysteresis, and contact damping are present, which may lead to observable discrepancies between theoretical and experimental transmissibility, particularly in the high-frequency range as shown in Fig. 33 and Fig. 34. The influence of these nonlinear damping effects will be investigated in future work by establishing refined dynamic models incorporating velocity- and displacement-dependent damping terms, as well as through parameter identification based on experimental data.

7. Conclusion

This paper proposes an innovative vibration isolator, designed with vertical and horizontal isolators, investigates its theoretical model, optimizes parameters for enhanced low-frequency isolation, and verifies its performance through shaking table tests, demonstrating superior vibration isolation capabilities compared to traditional systems.

(1) The three-dimensional system combines vertical (Z-axis) and horizontal (X- and Y-axis) quasi-zero stiffness isolators, arranged orthogonally using connecting components. Since each isolator operates independently, coupling effects can be reasonably ignored when analyzing vibration behavior in complex environments.

(2) Based on the developed three-dimensional quasi-zero stiffness isolator, mechanical models for both vertical (Z-axis) and horizontal (X- and Y-axis) isolation systems were further explored. Through parameter configuration, quasi-zero stiffness behavior at static equilibrium was achieved in all three directions, and the influence of key design parameters on the isolator's mechanical performance was systematically examined.

(3) Based on the geometric parameters of the three-dimensional device and the physical parameters of the spring components, the parameters of the vertical (Z-direction) and horizontal (X, Y-direction) quasi-zero stiffness isolation systems were optimized to expand the quasi-zero stiffness range and enhance the low-frequency isolation performance. Comparative analysis with traditional and equivalent linear isolation systems showed that the proposed system offers a broader isolation bandwidth and lower response amplitude, validating the excellent low-frequency isolation performance of the optimized device under three-dimensional vibration conditions.

(4) Prototypes of Z-axis, X-axis, and Y-axis quasi-zero stiffness isolators were developed and manufactured. These isolators were then combined into a complete three-dimensional quasi-zero stiffness vibration isolation system through the use of hinged fasteners and connection plates. The impact of excitation amplitude on the system's isolation performance was studied, and the displacement transmissibility obtained from the experiments was compared with the theoretical transmissibility characteristics derived from the dynamic analysis, validating the accuracy of the dynamic model and the excellent low-frequency isolation performance of the device.

Acknowledgements

The authors would like to thank the National Natural Science Foundation of China Key Program for the financial support provided under No.51438002, and thank the Quzhou University for the financial support provided under No.BSYJ202456.

Conflict of Interest

The manuscript has not been published before and is not being considered for publication elsewhere. All authors have contributed to the creation of this manuscript for important intellectual content and read and approved the final manuscript. We declare there is no conflict of interest.

Supporting Information

Not applicable.

CRediT Statement

Tao Liu: Writing - original draft, Writing - review & editing, Visualization. **Xiansong Xie:** Validation. **Aiqun Li:** Validation, Funding acquisition.

References

[1] Molyneux W. Supports for vibration isolation[M]. Great Britain: Aeronautical Research Council, 1957.

[2] J. van Eijk, J. F. Dijksman, Plate spring mechanism with constant negative stiffness, *Mechanism and Machine Theory*, 1979, **14**, 1-9, doi: 10.1016/0094-114X(79)90036-3.

[3] D. L. Platus, Negative-stiffness-mechanism vibration isolation systems, *Vibration Control in Microelectronics, Optics, and Metrology*, San Jose, CA. SPIE, 1992, 44-54, doi: 10.1117/12.56823.

[4] A. Carrella, M. J. Brennan, I. Kovacic, T. P. Waters, On the force transmissibility of a vibration isolator with quasi-zero-stiffness, *Journal of Sound and Vibration*, 2009, **322**, 707-717, doi: 10.1016/j.jsv.2008.11.034.

[5] A. Carrella, M. J. Brennan, T. P. Waters, Static analysis of a passive vibration isolator with quasi-zero-stiffness characteristic, *Journal of Sound and Vibration*, 2007, **301**, 678-689, doi: 10.1016/j.jsv.2006.10.011.

[6] I. Kovacic, M. J. Brennan, T. P. Waters, A study of a nonlinear vibration isolator with a quasi-zero stiffness characteristic, *Journal of Sound and Vibration*, 2008, **315**, 700-711, doi: 10.1016/j.jsv.2007.12.019.

[7] I. Kovacic, M. J. Brennan, B. Lineton, Effect of a static force on the dynamic behaviour of a harmonically excited quasi-zero stiffness system, *Journal of Sound and Vibration*, 2009, **325**, 870-883, doi: 10.1016/j.jsv.2009.03.036.

[8] Xu, D., Zhang, Y., Zhou, J., & Lou, J., On the analytical and experimental assessment of the performance of a quasi-zero-stiffness isolator, *Journal of Vibration and Control*, 2014, **20**(15), 2314-2325, doi: 10.1177/1077546313484

[9] F. Zhao, J. C. Ji, K. Ye, Q. Luo, Increase of quasi-zero stiffness region using two pairs of oblique springs, *Mechanical Systems and Signal Processing*, 2020, **144**, 106975, doi:

10.1016/j.ymssp.2020.106975.
[10] F. Zhao, J. Ji, K. Ye, Q. Luo, An innovative quasi-zero stiffness isolator with three pairs of oblique springs, *International Journal of Mechanical Sciences*, 2021, **192**, 106093, doi: 10.1016/j.ijmecsci.2020.106093.
[11] F. Zhao, J. Ji, Q. Luo, S. Cao, L. Chen, W. Du, An improved quasi-zero stiffness isolator with two pairs of oblique springs to increase isolation frequency band, *Nonlinear Dynamics*, 2021, **104**, 349-365, doi: 10.1007/s11071-021-06296-4.
[12] L. Meng, J. Sun, W. Wu, Theoretical design and characteristics analysis of a quasi-zero stiffness isolator using a disk spring as negative stiffness element, *Shock and Vibration*, 2015, **2015**, 813763, doi: 10.1155/2015/813763.
[13] Niu, F., Meng, L., Wu, W., Sun, J., Zhang, W., Meng, G., & Rao, Z., Design and analysis of a quasi-zero stiffness isolator using a slotted conical disk spring as negative stiffness structure, *Journal of Vibroengineering*, 2014, **16**(4), 1769-1785.
[14] A. R. Valeev, A. N. Zotov, S. A. Kharisov, Application of disk springs for manufacturing vibration isolators with quasi-zero stiffness, *Chemical and Petroleum Engineering*, 2015, **51**, 194-200, doi: 10.1007/s10556-015-0023-2.
[15] T. D. Le, K. K. Ahn, A vibration isolation system in low frequency excitation region using negative stiffness structure for vehicle seat, *Journal of Sound and Vibration*, 2011, **330**, 6311-6335, doi: 10.1016/j.jsv.2011.07.039.
[16] T. D. Le, K. K. Ahn, Experimental investigation of a vibration isolation system using negative stiffness structure, *International Journal of Mechanical Sciences*, 2013, **70**, 99-112, doi: 10.1016/j.ijmecsci.2013.02.009.
[17] C. Liu, K. Yu, Superharmonic resonance of the quasi-zero-stiffness vibration isolator and its effect on the isolation performance, *Nonlinear Dynamics*, 2020, **100**, 95-117, doi: 10.1007/s11071-020-05509-6.
[18] S. Dalela, P. S. Balaji, D. P. Jena, Design of a metastructure for vibration isolation with quasi-zero-stiffness characteristics using bistable curved beam, *Nonlinear Dynamics*, 2022, **108**, 1931-1971, doi: 10.1007/s11071-022-07301-0.
[19] S. Hou, J. Wei, A quasi-zero stiffness mechanism with monolithic flexible beams for low-frequency vibration isolation, *Mechanical Systems and Signal Processing*, 2024, **210**, 111154, doi: 10.1016/j.ymssp.2024.111154.
[20] J.-J. Lu, W.-H. Qi, F.-R. Liu, Y.-B. Cao, T.-Y. Zhao, L.-Q. Cai, Y. Li, G. Yan, W.-M. Zhang, Compliant curved beam support with flexible stiffness modulation for near-zero frequency vibration isolation, *Journal of Sound and Vibration*, 2025, **595**, 118702, doi: 10.1016/j.jsv.2024.118702.
[21] B. A. Fulcher, D. W. Shahan, M. R. Haberman, C. Conner Seepersad, P. S. Wilson, Analytical and experimental investigation of buckled beams as negative stiffness elements for passive vibration and shock isolation systems, *Journal of Vibration and Acoustics*, 2014, **136**, 031009, doi: 10.1115/1.4026888.
[22] X. Liu, X. Huang, H. Hua, On the characteristics of a quasi-zero stiffness isolator using Euler buckled beam as negative stiffness corrector, *Journal of Sound and Vibration*, 2013, **332**, 3359-3376, doi: 10.1016/j.jsv.2012.10.037.
[23] X. Huang, X. Liu, J. Sun, Z. Zhang, H. Hua, Vibration isolation characteristics of a nonlinear isolator using Euler buckled beam as negative stiffness corrector: a theoretical and experimental study, *Journal of Sound and Vibration*, 2014, **333**, 1132-1148, doi: 10.1016/j.jsv.2013.10.026.
[24] X. Liu, X. Huang, H. Hua, On the characteristics of a quasi-zero stiffness isolator using Euler buckled beam as negative stiffness corrector, *Journal of Sound and Vibration*, 2013, **332**, 3359-3376, doi: 10.1016/j.jsv.2012.10.037.
[25] J. Yang, Y. P. Xiong, J. T. Xing, Dynamics and power flow behaviour of a nonlinear vibration isolation system with a negative stiffness mechanism, *Journal of Sound and Vibration*, 2013, **332**, 167-183, doi: 10.1016/j.jsv.2012.08.010.
[26] S. S. Antman, Ordinary differential equations of non-linear elasticity I: Foundations of the theories of non-linearly elastic rods and shells, *Archive for Rational Mechanics and Analysis*, 1976, **61**, 307-351, doi: 10.1007/BF00250722.
[27] C. Truesdell, Ed., *Linear theories of elasticity and thermoelasticity: Linear and nonlinear theories of rods, plates, and shells*, Springer, 1984, **2**, ISBN- 9783662397763.
[28] B. Budiansky, Theory of buckling and post-buckling behavior of elastic structures, *Advances in Applied Mechanics*, 1974, **14**, 1-65, doi: 10.1016/s0065-2156(08)70030-9.
[29] L. Liu, Y. Chai, Z. Guo, M. Li, A novel isolation system with enhanced QZS properties for supporting multiple loads, *Aerospace Science and Technology*, 2023, **143**, 108719, doi: 10.1016/j.ast.2023.108719.
[30] Y. Wang, H.-X. Li, W.-A. Jiang, H. Ding, L.-Q. Chen, A base excited mixed-connected inerter-based quasi-zero stiffness vibration isolator with mistuned load, *Mechanics of Advanced Materials and Structures*, 2022, **29**, 4224-4242, doi: 10.1080/15376494.2021.1922961.
[31] X. Wang, X. Yue, H. Dai, J. Yuan, Vibration suppression for post-capture spacecraft *via* a novel bio-inspired Stewart isolation system, *Acta Astronautica*, 2020, **168**, 1-22, doi: 10.1016/j.actaastro.2019.11.033.
[32] J. Wang, G. Yao, Multi-directional vibration isolation performances of a scissor-like structure with nonlinear hybrid spring stiffness, *Nonlinear Dynamics*, 2024, **112**, 8871-8888, doi: 10.1007/s11071-024-09561-4.
[33] W. Zou, C. Cheng, R. Ma, Y. Hu, W. Wang, Performance analysis of a quasi-zero stiffness vibration isolation system with scissor-like structures, *Archive of Applied Mechanics*, 2021, **91**, 117-133, doi: 10.1007/s00419-020-01757-5.
[34] L. Guo, A. Khiu, R. L. Fan, X. Wang, Analysis of a passive scissor-like structure isolator with quasi-zero stiffness for a seating system vibration-isolation application, *International Journal of Vehicle Design*, 2020, **82**, 224, doi: 10.1504/ijvd.2020.113920.
[35] W. Zhang, J. Zhao, Analysis on nonlinear stiffness and vibration isolation performance of scissor-like structure with full types, *Nonlinear Dynamics*, 2016, **86**, 17-36, doi: 10.1007/s11071-016-2869-z.
[36] X. Sun, X. Jing, J. Xu, L. Cheng, Vibration isolation *via* a

scissor-like structured platform, *Journal of Sound and Vibration*, 2014, **333**, 2404-2420, doi: 10.1016/j.jsv.2013.12.025.
[37] M. Li, W. Cheng, R. Xie, A quasi-zero-stiffness vibration isolator using a cam mechanism with user-defined profile, *International Journal of Mechanical Sciences*, 2021, **189**, 105938, doi: 10.1016/j.ijmecsci.2020.105938.
[38] S. Zuo, D. Wang, Y. Zhang, Q. Luo, Design and testing of a parabolic cam-roller quasi-zero-stiffness vibration isolator, *International Journal of Mechanical Sciences*, 2022, **220**, 107146, doi: 10.1016/j.ijmecsci.2022.107146.
[39] S. Zuo, D. Wang, Y. Zhang, Q. Luo, An innovative design of parabolic cam-roller quasi-zero-stiffness isolators for ultralow frequency vibration isolation, *Nonlinear Dynamics*, 2024, **112**, 18717-18744, doi: 10.1007/s11071-024-10011-4.
[40] Li, Y., Wu, Z., Peng, Y., Yao, S., & Zhou, J., Full-band vibration isolation of multi-step quasi-zero stiffness systems, *International Journal of Mechanical Sciences*, 2024, **274**, 109277, doi: 10.1016/j.ijmecsci.2024.109277.
[41] Y. Zhang, H. Wen, H. Hu, D. Jin, A novel quasi-zero stiffness isolator with designable stiffness using cam-roller-spring-rod mechanism, *Acta Mechanica Sinica*, 2024, **41**, 524210, doi: 10.1007/s10409-024-24210-x.
[42] Liu, F., Liao, X., Chen, L., & Jiao, R., Modeling and dynamics of a piecewise quasi-zero-stiffness vibration isolation system with cam, *Journal of the Brazilian Society of Mechanical Sciences and Engineering*, 2025, **47**, 177, doi: 10.1007/s40430-025-05449-5.
[43] G. Jiao, J. Zeng, S. Wang, A compact magnetic-curved-spring QZS isolator for supporting uncertain loads, *Nonlinear Dynamics*, 2025, **113**, 9217-9238, doi: 10.1007/s11071-024-10595-x.
[44] Y. Zheng, X. Zhang, Y. Luo, Y. Zhang, S. Xie, Analytical study of a quasi-zero stiffness coupling using a torsion magnetic spring with negative stiffness, *Mechanical Systems and Signal Processing*, 2018, **100**, 135-151, doi: 10.1016/j.ymssp.2017.07.028.
[45] X.-C. Liu, H. Ding, X.-F. Geng, K.-X. Wei, S.-K. Lai, L.-Q. Chen, A magnetic nonlinear energy sink with quasi-zero stiffness characteristics, *Nonlinear Dynamics*, 2024, **112**, 5895-5918, doi: 10.1007/s11071-024-09379-0.
[46] B. Yan, N. Yu, Z. Wang, C. Wu, S. Wang, W. Zhang, Lever-type quasi-zero stiffness vibration isolator with magnetic spring, *Journal of Sound and Vibration*, 2022, **527**, 116865, doi: 10.1016/j.jsv.2022.116865.
[47] B. Yan, N. Yu, C. Wu, A state-of-the-art review on low-frequency nonlinear vibration isolation with electromagnetic mechanisms, *Applied Mathematics and Mechanics* (*English Edition*), 2022, **43**, 1045-1062, doi: 10.1007/s10483-022-2868-5.
[48] Z. Ma, R. Zhou, Q. Yang, H. P. Lee, K. Chai, A semi-active electromagnetic quasi-zero-stiffness vibration isolator, *International Journal of Mechanical Sciences*, 2023, **252**, 108357, doi: 10.1016/j.ijmecsci.2023.108357.
[49] MengTong, W., Pan, S., ShuYong, L., Kai, C., BoXiang, W., & Jinfang, L., Design and analysis of electromagnetic quasi-zero stiffness vibration isolator, *Journal of vibration engineering & Technologies*, 2023, **11**, 153-164, doi: 10.1007/s42417-022-00569-x.
[50] Y. Jiang, C. Song, C. Ding, B. Xu, Design of magnetic-air hybrid quasi-zero stiffness vibration isolation system, *Journal of Sound and Vibration*, 2020, **477**, 115346, doi: 10.1016/j.jsv.2020.115346.
[51] S. Yuan, Y. Sun, J. Zhao, K. Meng, M. Wang, H. Pu, Y. Peng, J. Luo, S. Xie, A tunable quasi-zero stiffness isolator based on a linear electromagnetic spring, *Journal of Sound and Vibration*, 2020, **482**, 115449, doi: 10.1016/j.jsv.2020.115449.
[52] Y. Sun, J. Zhao, M. Wang, Y. Sun, H. Pu, J. Luo, Y. Peng, S. Xie, Y. Yang, High-static–low-dynamic stiffness isolator with tunable electromagnetic mechanism, *IEEE/ASME Transactions on Mechatronics*, 2020, **25**, 316-326, doi: 10.1109/TMECH.2019.2954910.
[53] Y. Sun, K. Meng, S. Yuan, J. Zhao, R. Xie, Y. Yang, J. Luo, Y. Peng, S. Xie, H. Pu, Modeling electromagnetic force and axial-stiffness for an electromagnetic negative-stiffness spring toward vibration isolation, *IEEE Transactions on Magnetics*, 2019, **55**, 8000410, doi: 10.1109/TMAG.2018.2879046.
[54] N. Yu, X. Fei, H. Sun, Z. Wu, B. Yan, Rhombus-type magnetic-levitation structure for low-frequency vibration isolation, *Mechanical Systems and Signal Processing*, 2025, **225**, 112289, doi: 10.1016/j.ymssp.2024.112289.
[55] T. Zhu, B. Cazzolato, W. S. P. Robertson, A. Zander, Vibration isolation using six degree-of-freedom quasi-zero stiffness magnetic levitation, *Journal of Sound and Vibration*, 2015, **358**, 48-73, doi: 10.1016/j.jsv.2015.07.013.
[56] Y. Lou, H. Zhang, L. Zhang, H. Cai, Advancements in key technologies for vibration isolators utilizing electromagnetic levitation, *Energies*, 2024, **17**, 5343, doi: 10.3390/en17215343.